



Universiteit
Leiden
The Netherlands

Development and application of cryo-EM tools to study the ultrastructure of microbes in changing environments

Depelteau, J.S.

Citation

Depelteau, J. S. (2022, January 12). *Development and application of cryo-EM tools to study the ultrastructure of microbes in changing environments*.

Retrieved from <https://hdl.handle.net/1887/3249707>

Version: Publisher's Version

License: [Licence agreement concerning inclusion of doctoral thesis in the Institutional Repository of the University of Leiden](#)

Downloaded from: <https://hdl.handle.net/1887/3249707>

Note: To cite this publication please use the final published version (if applicable).

**Development and application of
cryo-EM tools to study the
ultrastructure of microbes in
changing environments**

PhD Thesis, Leiden University, 2021

ISBN: 978-94-6416-975-1

Cover design and layout by Jamie Scott Depelteau

Printed by Ridderprint | www.ridderprint.nl

Development and application of cryo-EM tools to study the ultrastructure of microbes in changing environments

Proefschrift

ter verkrijging van
de graad van doctor aan de Universiteit Leiden,
op gezag van rector magnificus prof.dr.ir. H. Bijl,
volgens besluit van het college voor promoties
te verdedigen op woensdag 12 januari 2022
klokke 13:45 uur

door

Jamie Scott Depelteau

geboren te Concord, New Hampshire,
Verenigde Staten van Amerika

in 1979

Promotiecommissie

Promotoren:

Prof. dr. A. Briegel

Prof. dr. A.H. Meijer

Overige leden:

Prof. dr. G.P. van Wezel (voorzitter)

Prof. dr. D. Claessen (secretaris)

Prof. dr. M. Blokesch (Swiss Federal Institute of Technology Lausanne)

Prof. dr. A.J. Koster (Leiden University Medical Center)

Prof. dr. H.P. Spaijk

The work in this dissertation was funded by a Building Blocks of Life Grant 737.016.004 from the Netherlands Organization for Scientific Research (NWO) and an Instruct-ULTRA Horizon 2020 Coordination and Support action Number ID: 731005. Microscope access was partially funded by Netherlands Electron Microscopy Infrastructure (NEMI) grant 84.034.014 provided by the NWO.

Contents

Chapter 1	General Introduction.....	7
Chapter 2	Bacterial and Archaeal Cell Structure.....	17
Chapter 3	An economical, portable manual cryogenic plunge freezer for the preparation of vitrified biological samples for cryogenic electron microscopy.....	43
Chapter 4	Transition of <i>Vibrio cholerae</i> through a natural host induces resistance to environmental changes	59
Chapter 5	UVC inactivation of pathogenic samples suitable for cryo-EM analysis.....	79
Chapter 6	Advanced methods for processing of large volume samples for cryogenic electron tomography	103
Chapter 7	General Discussion & Summary	123
	References	133
	Nederlandse samenvatting	145
	Curriculum vitae.....	149
	Publications.....	151

CHAPTER 1

General Introduction

General Introduction

Bacteria are ubiquitous in nature and certain species have adapted to thrive in even the most extreme environments. Moreover, cells from individual species can adapt to changing conditions, such as in soil, in fresh, brackish, or salt water as well as inside a host organism. Yet, much is still unknown about how bacteria can adapt to these changing conditions and thrive as individual cells, as part of microbial communities, or in close interaction with cells of a eukaryotic host.

The structural makeup of bacterial cells contributes to their ability to navigate and persist in environmental niches: they can produce a variety of molecular machines which enable the cells to sense and interact with their environment. They can even adjust their overall cell morphology. Gaining insight into bacterial ultrastructure in different growth conditions is essential to understand how bacteria adjust and change in complex environments. This is especially relevant for pathogens that cause hard-to-treat infections. Detailed insight into their specific morphological and structural characteristics during infection may open new treatment avenues.

However, the tools required to examine the ultrastructure that enables environmental interactions have only recently become available to the larger scientific community. The aim of this thesis is to develop and use tools and workflows for electron microscopy (EM) to better understand these interactions.

Cryogenic EM (cryo-EM) has become an especially powerful technique to peer inside of cells and to study specific protein complexes. Two types of cryo-EM are primarily used for these types of studies. To study whole cells and their associated molecular machines *in vivo*, cryo-electron tomography (cryo-ET) is used (outlined in Fig. 1). With this technique, cells are flash-frozen on an EM support grid using a cryogen cooled to liquid nitrogen temperatures (-194°C). These samples are preserved in a near-native state because the water molecules do not have time to crystalize, instead forming an amorphous state that does not impact the sample (1). The frozen samples are then transferred to an electron microscope, where a series of images are collected while the sample is tilted. The resulting images can then be computational combined to reconstruct a three-dimensional (3D) volume of the sample. These data can then be used to analyze structures of interest and can be further processed to obtain high resolution information about the structures at the macromolecular scale (2-4 nm, Fig. 2).

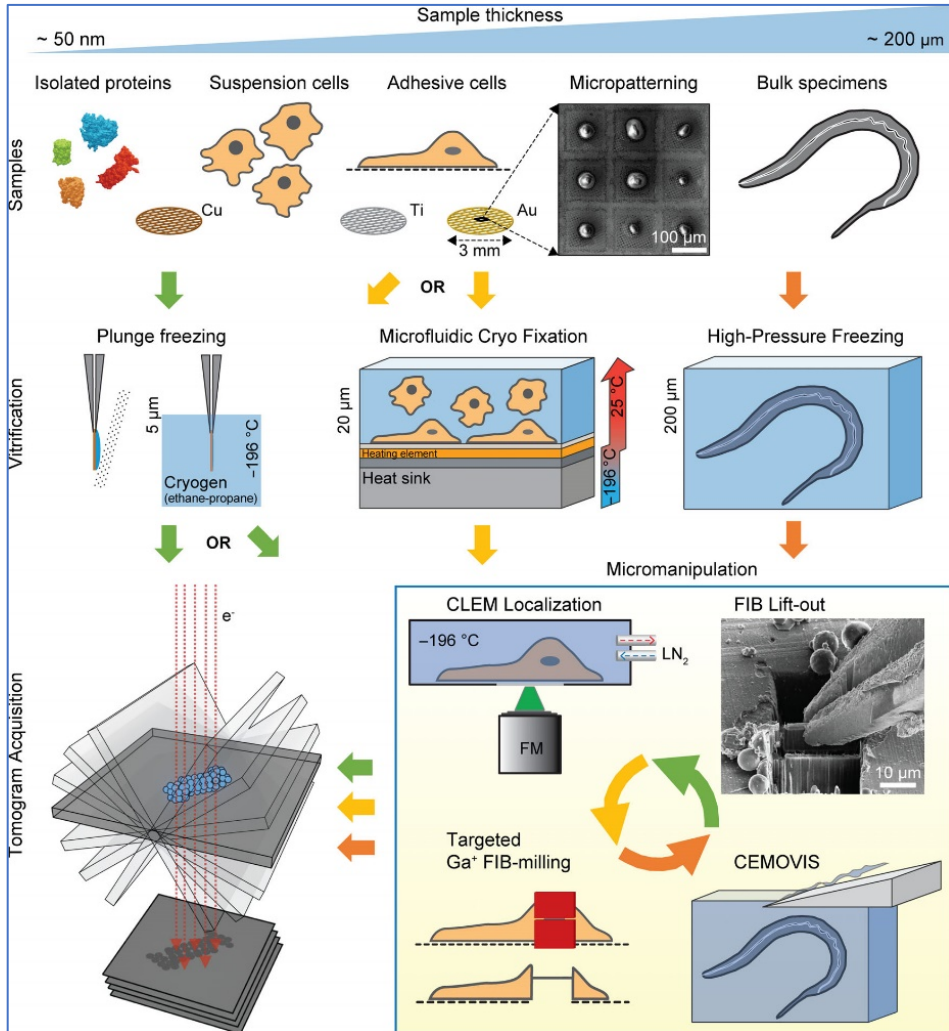


Figure 1, Overview of cryo-ET sample preparation and imaging workflow. Samples with a thickness of less than 5-10 μm are typically frozen by plunge freezing and then directly imaged using cryo-ET. However, if the area of interest falls within the thicker region, then thinning of the sample may be required. New freezing techniques allow for freezing directly on the cryo-stage (microfluidic cryo-fixation), though this technique is not assessed in this work. For samples greater than 10 μm , high pressure freezing is the typical process for vitrification. Once frozen, the sample requires thinning using focused ion beam (FIB) milling, FIB lift-out, and or CEMOVIS. Sample thicknesses of approximately 200nm provide a good balance between sample stability, image quality and sampling of the cell. The thinned sample is transferred to the cryo-EM for imaging and further analysis. Adapted from (2).

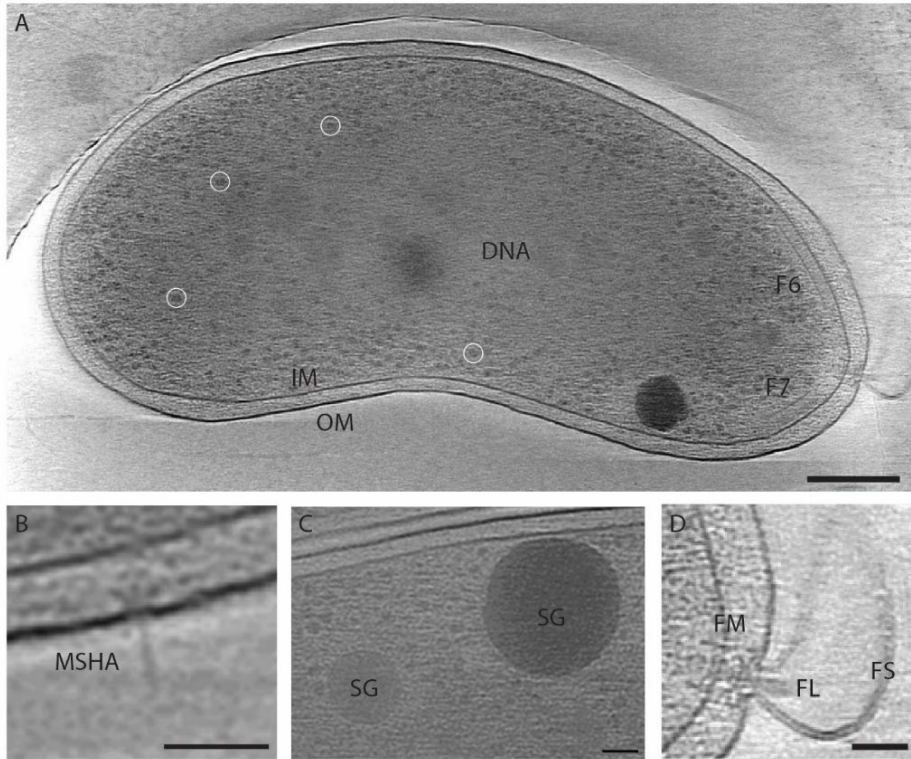


Figure 2. Examples of structures visible by cryo-ET. A. A single slice of a tomogram showing a whole *Vibrio cholerae* cell grown in LB overnight at 30°C. Different structural aspects denoted include the inner and outer membrane, (IM, OM), the ribosomes (selected examples are circled with white), areas of ribosome exclusion where the DNA is located, and two types of chemotaxis arrays (F6 & F7). B-D. Other structures that are identifiable using cryo-ET include the MSHA pili and its basal body in B, storage granules (SG) in C, and the flagella apparatus (flagellar motor (FM), the flagellum (FL), and the flagellar sheath (FS) in D. Scale bar = 200nm in A, and 50nm in B-D.

Alternatively, cryo-EM can be used to study individual proteins and protein complexes in solution, which typically allows for higher resolution information. As with cryo-ET, the sample is applied to an EM support grid and plunge frozen to embed the sample in an amorphous buffer solution. Using the electron microscope, individual images are taken from numerous positions on the EM grid. Each image contains a large number of individual particles, each randomly orientated with respect to the electron beam. These particles are then selected from each image, and computationally combined to create a 3D structure. With this technique, resolutions similar to crystallography can be obtained (sub nm, in ideal cases 2 Å or better have been achieved) which can provide significant insight into the structure of interest.

Together, these techniques provide a tremendous opportunity to better understand the bacteria at the nanoscale. However, there are still some challenges associated with these techniques. Sample thickness is especially challenging due to the limited ability of the electrons to penetrate the sample of interest. This becomes most clear when using cryo-ET to image intact bacterial cells. For instance, *Vibrio cholerae*, a common bacterial species used for studying a diverse set of molecular machines, can exceed 0.5 μm in diameter. This thickness is approaching the penetration limit of the electron beam when operating at 300 keV, which is a typical voltage for cryo-EM studies (3). In addition, we must consider that as the sample is tilted, the thickness further increases, meaning the less information that can be recovered. Thus, other techniques are necessary to prepare EM grids from samples of greater thicknesses.

Sample thickness is not just a challenge during cryo-EM imaging. Only relatively thin samples can be frozen by directly plunging them in a cryogen (ethane or ethane-propane mixture)(1, 4). Using thicker samples, such as larger cells, biofilms, or tissues that exceed 5 μm , the freezing rate during plunge-freezing is not fast enough to prevent ice crystal formation. Therefore, other methods must be used to vitrify thick samples. The most common technique for freezing volumes up to 250 μm is high pressure freezing. This technique combines the application of high pressure with rapid cooling to freeze the sample in amorphous water, buffer or growth media (5). Samples prepared by high-pressure freezing need additional thinning steps in order for the sample to be imaged with cryo-EM.

Samples less than 20 μm can be thinned using an ion beam, a technique referred to as cryogenic focused ion beam scanning electron microscopy (cryo-FIB SEM). The ion beam is used to ablate the material in a targeted way. The SEM beam is used to monitor the milling progress, ultimately producing so-called lamella with a thickness of approximately 200 nm (which is considered a good balance between thickness and the ability for electrons to pass through the sample).

Samples with a greater thickness must be thinned by other methods prior to imaging, either by cryogenic ultramicrotomy or ‘cryogenic lift out’. This is due to the limited depth of focus for the ion beam. In cryo-ultramicrotomy, the sample is thinned at cryogenic temperatures using a diamond knife, which removes 75-100 nm sections with each stroke (6, 7). These sections can then be transferred to an EM support grid for imaging. For the cryo-lift out method, a specialized cryo-FIB SEM is used. In this case, the focused ion beam is used to create trenches on either side of the area of interest and then the remaining tissue is lifted out with a mechanical arm, transferred to a specialty grid, and then milled to create lamella

for imaging (8, 9). However, both techniques are challenging and time consuming, and require someone specifically trained in the techniques.

An alternative method for preparing large volume samples lies in classical electron microscopy. Serial block face scanning electron microscopy (SBF SEM) continues to improve, allowing the automated trimming and image collection of larger volumes of samples (10). With this technique, the sample is prepared using chemical fixatives rather than physical fixation (such as vitrification), followed by subsequent steps to exchange the water molecules with non-ionic solvents and finally embedded in resin. The sample is roughly trimmed, and then inserted into a SEM that is equipped to trim the sample during imaging (Fig. 3). Imaging using this instrument allows the visualization of large volumes (in our case, up to 150 μm) because of its ability to repeat the process of section removal, imaging, removal, imaging, etc. unsupervised. The individual images of the sections can then be combined to reconstruct the volume in 3D. An alternative of this technique combines high pressure freezing with chemical fixation, which has been shown to greatly improve sample preservation (11). However resolution is still limited to larger features such as cell shape, storage granules, and flagella. Smaller structures below this resolution (i.e. $< 2 \text{ nm}$) require methods that preserve samples in near native states, as demonstrated by cryo-ET.

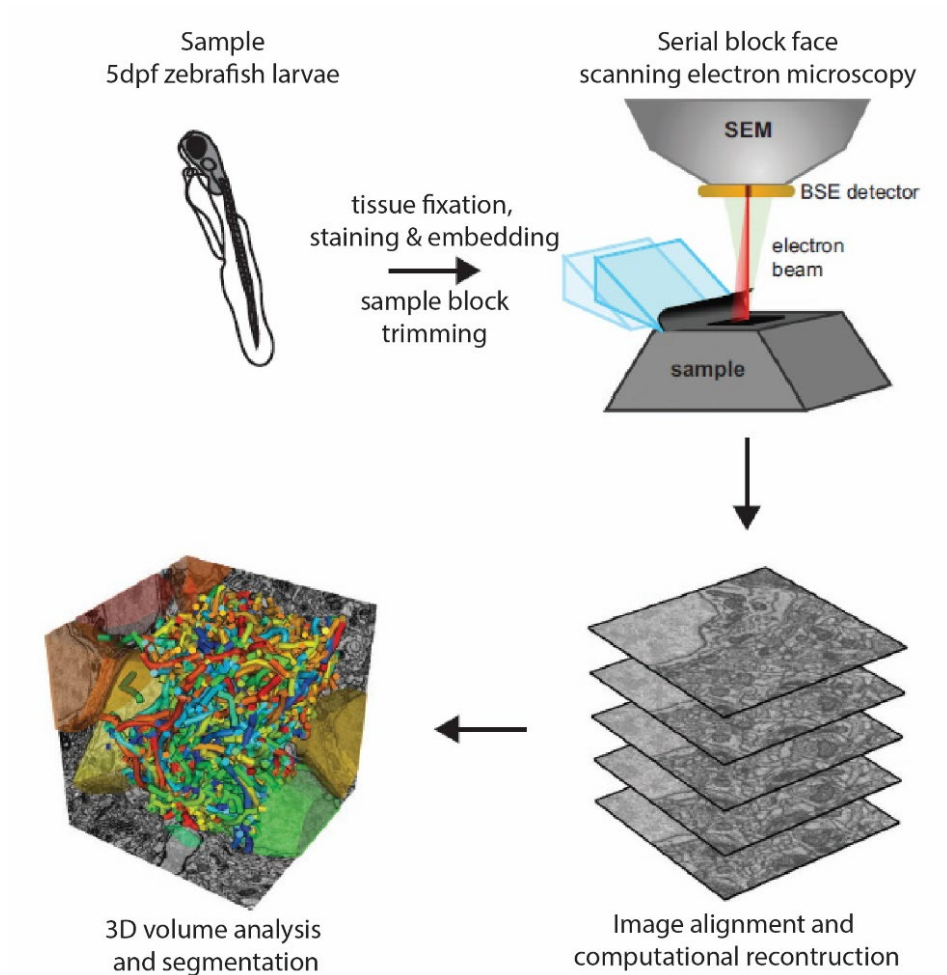


Figure 3. Overview of serial block face scanning electron microscopy. The sample is fixed, stained, and embedded in resin. Once polymerized, the block containing sample is roughly trimmed and then inserted into the SBF SEM instrument. During data collection, the sample is trimmed using a diamond knife with a determined thickness, followed by imaging using the SEM beam. This process is repeated through the volume, and the resulting images are then computationally combined into a 3D volume (Image alignment and computational reconstruction). Areas of interest can then be segmented for further analysis (3D volume analysis and segmentation). Adapted from (10).

Together, these techniques allow an unprecedented view into the microbial world and provide opportunities to examine the multicellular environment. Cryo-ET methods also allow resolutions that approach the atomic scales, providing key insights into the structural biology of the molecular machines that are important to a bacterium's ability to adjust to changing environments. The goal of this thesis is to employ these techniques to better understand how bacteria interact with their environment, and to develop and employ the tools necessary to engage these techniques in answering this question.

Thesis Outline

In this thesis, I describe the use of the various cryo-EM techniques to gain insight into the structural changes of the human pathogen, *Vibrio cholerae*, and its transitions between different environments. A combination of techniques is used that describe how to prepare the individual cells for cryo-ET using a locally designed manual plunging apparatus and how to visualize changes to the cells' morphology and structure when transitioning from the environment and back into the host. I also show how environmental conditions, such as exposure to ultraviolet-C radiation, affects the ultrastructure of *V. cholerae* and the associated ICP1 bacteriophage. Together with biochemical techniques and microbiology assays, cryo-EM proves to be a powerful technique for elucidating how bacteria adapt to changing environments.

In **chapter two**, I begin with an overview of bacterial and archaeal ultrastructure, highlighting molecular machines that have been investigated by methods including classical and cryo-EM. Many of these machines have been shown to be important for interacting with the microbe's environment, and a significant amount of the current knowledge that is known is because of methods in cryo-EM. For instance, I describe the F6 chemotaxis array, which is responsible for sensing chemical signals in the environment, and the flagellar apparatus, which is then used to move toward or away depending on that signal. This chapter lays the foundation for several of the following chapters.

Chapter three describes the development of a portable manual plunge freezing device. The inspiration for this device came when the sample preparation for a collaborative project could not be carried out within our own group, and the collaborating lab did not have a cryo-EM setup. The portable manual plunge freezer developed here is an inexpensive alternative to commercially available options and allows the device to be easily moved from lab to lab, locally, nationally, or internationally. Subsequently, I used this device for the analysis of the

ultrastructure of *V. cholerae* that had been excreted by the natural host, the zebrafish (*Danio rerio*). In this case, I was able to travel to the lab with the expertise in the infection model and use the device to prepare the cells.

Using the manual freezing device, in **chapter four** I examine *V. cholerae* for changes in its morphology and the molecular machines as this bacterium transitions from the environment, into a zebrafish host, and then back into the environment. This important piece of work demonstrates the journey through a natural host's digestive track results in a more resilient bacterium that is better able to adjust to environmental changes. This resilience likely primes the bacterium to move from host to host more efficiently, and analysis of the molecular machines showed that cells that maintained their vibrioid or near-viroid shape also retained the molecular machines that are important to sensing and attachment during colonization. To gain these insights, I used cryo-EM, confocal imaging, SBF-SEM, and microbiological techniques to characterize the bacterium at different stages in the infection cycle.

Working with a pathogenic species requires the adherence to strict biosafety guidelines to ensure the safety of staff, researchers, and the surrounding environment. In **chapter five**, in another effort to increase access to cryo-EM, I focused on the effect of ultraviolet C (UVC) irradiation on sample integrity and the ability to access high resolution structural information after irradiation. In this study, I targeted two types of samples, the bacterium *V. cholerae* for subtomogram averaging, and the ICP1 bacteriophage for single particle analysis. The importance of this study became even more apparent with the outbreak of the COVID-19 pandemic as UVC irradiation is a well-established protocol for disinfection. Exposure to UVC causes changes to the DNA which in turn prevents replication of the bacterium or virus (12). Our study demonstrated that UVC exposure at cryogenic temperatures is a suitable method for inactivation of pathogens. Furthermore, the structural information gained from the inactivated pathogen is indistinguishable to untreated organisms. For the bacterial sample, I achieved a resolution of 22.6Å after inactivation with 30 seconds of UVC using our home-built device. For the bacterial virus sample, I achieved a resolution of 5.1Å for the capsid after 60s UVC treatment on the carbon and 30s of treatment on the copper side of the support grid. In addition to the economical device used for UVC treatment, this chapter also demonstrates the possibility of using UVC irradiation as a way to lower the biosafety level of pathogens which can then be imaged in most cryo-EM facilities, even those lacking biosafety certifications.

In **chapter six**, I describe the current state of large volume sample preparation using microfabricated biopsy needles. The challenges associated with these sample types

and the promising workflows that I am developing in collaboration with members of the group and our local fine mechanical department are given. I first tested glass needles for the biopsy of various tissue types. I then utilize 3D printed needles to retrieve samples from a bacterial colony of *Streptomyces coelicolor*, which were subsequently frozen by high pressure freezing in preparation for sample thinning by cryo-ultramicrotomy and cryo-FIB SEM. In addition, we began the steps of optimal sample preparation by freezing of sample directly on EM support grids. Together, I demonstrate that our biopsy needles are suitable for the cryo-EM workflow.

Overall, as summarized and discussed in **chapter seven**, this thesis provides unique insight into the infection life cycle of *V. cholerae* while also developing devices that invite more users into the field of cryo-EM.

CHAPTER 2

Bacterial and Archaeal Cell Structure

This chapter is published as:

Jamie S. Depelteau¹, Susanne Brenzinger¹, and Ariane Briegel¹. (2019) Bacterial and Archaeal Cell Structure, Editor(s): Thomas M. Schmidt, Encyclopedia of Microbiology (Fourth Edition), Academic Press, Pages 348-360.

¹Institute of Biology Leiden, Leiden University, Leiden, Netherlands

Abstract

The intricate nature of the cellular structure in bacteria and archaea has historically been underappreciated because of their small size. However, the advent of new microscopy techniques, such as fluorescent microscopy, super resolution light microscopy, cryo-electron microscopy, electron cryotomography and correlative microscopy techniques now enables the study of intact microbial cells at unprecedented resolution. We are now able to directly observe microbial cell structures and gain insight into essential processes such as establishing the proper cell shape, cell growth, division, motility, sensing and interacting with the environment and the formation of cellular communities. In this article, we will give a brief overview into the components of bacterial and archaeal cells, and how the cells rely on these structures to thrive.

Cell Boundaries of Microorganisms

Most bacteria and archaea constantly face changing and often hostile environments. Therefore, their cell envelopes must provide adequate protection against physical, chemical, and biological stresses while allowing an adequate influx of nutrients and efflux of waste products and signaling molecules. As bacterial and archaeal cell envelopes differ fundamentally in their composition and structure, they will be discussed separately.

Bacterial Envelope Structure

Traditionally, bacterial envelopes are classified into one of two groups using the Gram stain. Gram-negative bacteria possess a cytoplasmic membrane (CM), a thin peptidoglycan (PG) layer and an outer membrane (OM), while Gram-positive bacteria lack the OM and produce a thicker PG cell wall (Fig. 1, upper panel). Some notable exceptions of bacteria that lack a continuous PG layer exist, such as in *Mycoplasma*. The CM of bacteria is a phospholipid bilayer, its two leaflets are clearly distinguishable using electron microscopy at high magnification (Fig. 1, lower panel). The CM is water-permeable but impermeable to polar organic solutes and inorganic ions. This allows the cells to generate an inward-directed proton motive force, which is used to facilitate essential processes such as ATP syntheses and motility. Accordingly, a multitude of proteins involved in energy production, transport and secretion are embedded in the CM.

The major stress-bearing component of most bacteria is the PG network that envelopes the cell. PG is composed of long glycan strands of alternating N-acetyl glucosamine and N-acetyl muramic acid molecules which are crosslinked by short peptide chains. The CM and the PG are separated by a 10–20 nm wide space. In Gram-positive and -negative bacteria, the PG is similar in chemical composition and synthesis, but the PG layer of Gram-positive bacteria is substantially thicker (40 nm) than in Gram-negatives. Lipoteichoic acids associated with the CM, teichoic acids and polysaccharides, which are linked to the PG, extend through the peptidoglycan network and form a negatively charged, loose outer layer. In Gram-negative bacteria, the PG is a 4 nm thin single layered mesh. The glycan strands run in a circumferential fashion around the cell body and the peptides roughly parallel to the long axis of the cell (see Fig. 2). While the PG of Gram-positive cells is generally much thicker than that of Gram-negatives, the thickness does not serve as a reliable phylogenetic

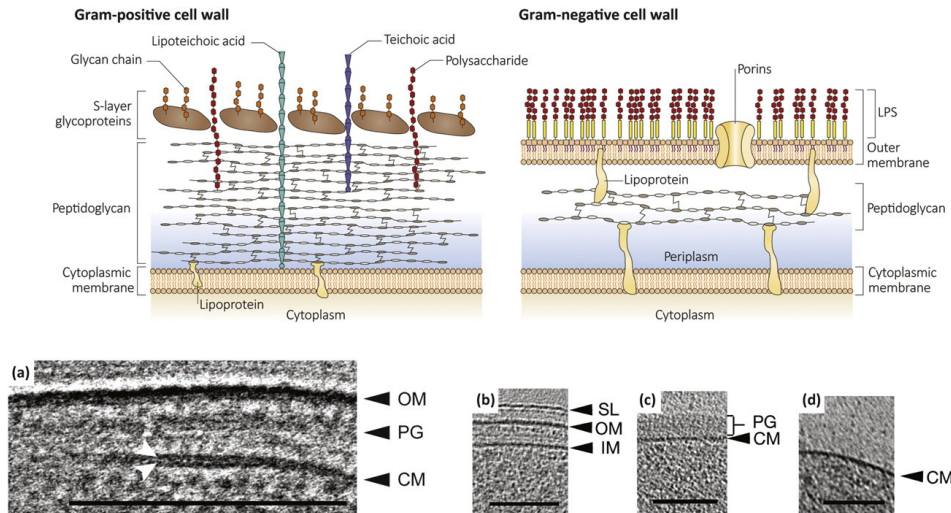


Figure 1. (Upper panel) Schematic side view of cell envelopes of exemplarily Gram-negative and -positive bacterial cells. LPS, Lipopolysaccharides. (Lower panel) Electron micrographs show the architecture of a Gram-negative cell wall without S-layer showing the two leaflets of the cytoplasmic membrane (white arrows): (a) *Vibrio cholera*; a Gram-negative envelope with S-layer: (b) *Caulobacter crescentus*; Gram-positive cell wall: (c) *Listeria monocytogenes*; cell-wall less: (d) *Mycoplasma pneumoniae*. IM, inner membrane; OM, outer membrane; PG, peptidoglycan; SL, S-Layer; CM, cytoplasmic membrane; LPS, Lipopolysaccharides. Scale bars, 100 nm. Upper Panel reproduced from (13). Lower panel (a) courtesy of Wen Yang; (b-d) reproduced (14).

marker as several species possess intermediate thicknesses, and Gram-negative and -positive staining organisms may be found in the same class. Furthermore, the thick PG layer of *Bacillus subtilis* and *Acetonebma longum* is converted to a thin layer reminiscent of the PG of Gram-negative bacteria during then initial stages of sporulation. The PG layer in Gram-negative bacteria is enclosed by the OM. The OM itself differs chemically from the CM as it is composed of an inner leaflet and an exterior leaflet of lipopolysaccharides (LPS) that provide the cell with a negatively charged barrier.

Some Gram-positive and -negative bacteria produce an additional proteinaceous surface layer on top of the PG layer or OM, respectively. This S-layer is mostly composed of one protein that self-assembles into oblique, square, or hexagonal lattice symmetries. Since the S-layer proteins arrange into a two-dimensional crystal in vitro, they can readily be studied by electron microscopy (Fig. 3). Finally, the outmost layer of many Gram-positive and -negative bacteria is a thick capsule of vastly variable polysaccharide associated with the OM or PG. This capsule provides additional protection against desiccation and is of clinical relevance as it facilitates cell attachment and evasion of the host immune defense.

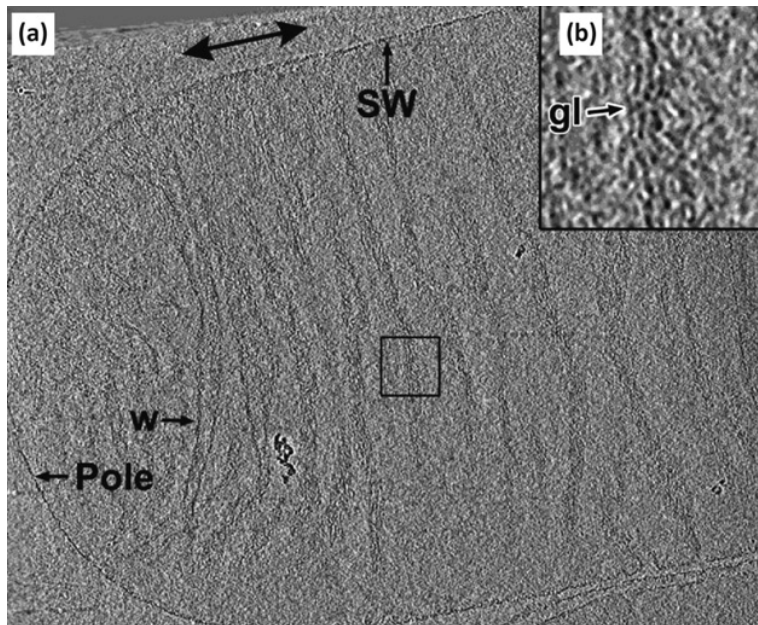


Figure 2. (a) Tomographic slices of *E. coli* XL-10 sacculus. Abbreviations: (gl) glycan strand; (SW) side wall; (w) wrinkle. (b) A four-fold enlarged view of the boxed region showing the glycan strands of the sacculus. The double-headed arrow denotes the saccular polar axis. Reproduced from (15).

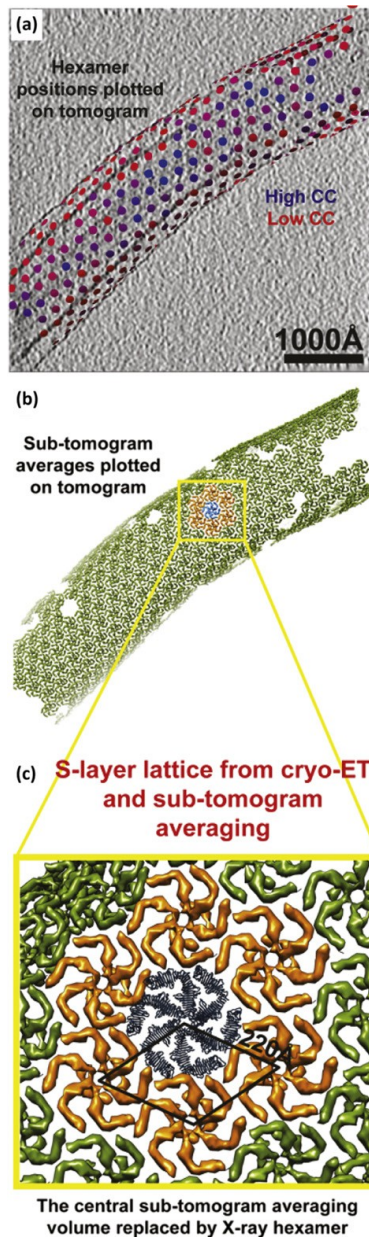


Figure 3. (a) Final refined positions of subtomograms of S-layer proteins plotted back onto a tomogram of a *C. crescentus* cell stalk with the corresponding refined orientations. Positions have been coloured from blue (high cross-correlation of alignment) to red (low cross-correlation). (b) The same plot as panel A, except each hexamer position is illustrated with the subtomogram average (green volumes). One hexamer is highlighted in blue, and the hexamers directly contacting it are shown in orange. (c) A zoomed view of the hexameric lattice revealed by cryo-ET and subtomogram averaging. The central blue hexamer from panel B is replaced by one copy of the X-ray hexamer. Reproduced from (16).

Archaeal Envelope Structure

While the chemical composition of CM, PG and OM is conserved among the bacteria, archaea produce a more diverse and species-specific set of envelope components (Fig. 4(a)). The lipids comprising the CM are unique for the archaea. Some species produce diether lipids that arrange into two leaflets whereas others possess tetraether lipids with up to 8 cyclopentane rings, thus forming a monolayer. Archaea also produce a variety of further structural components that envelope the CM. Some Euryarchaeota possess a cell wall composed of sugar polymers. However, unlike the PG of bacteria, archaeal cell walls differ vastly regarding their chemical composition and properties. Methanochondroitin for example is a fibrillar polymer that forms a rather loose matrix around aggregated cells. In contrast, pseudomurein has a thickness of approximately 15–20 nm and resembles PG in general architecture and rigidity. In most archaea that lack polymeric cell walls, an additional proteinaceous layer provides protection and maintains the cell shape. Most commonly, this is an S-layer with similar properties as their bacterial counterparts. However, while bacterial S-layers are only five to 20 nm thick, they may reach a thickness of up to 70 nm in archaea (Fig. 4(b)). Another type of protein layer is the tubular sheath of the filamentous growing *Methanospirillum* and *Methanosaeta* species. This sheath is composed of circumferential rings that envelope the entire filament. The circumferential hoops can clearly be seen using transmission electron microscopy (TEM). Capsule-like structures have been described for several archaea and genomic analysis suggests that many archaea encode genes for capsule systems.

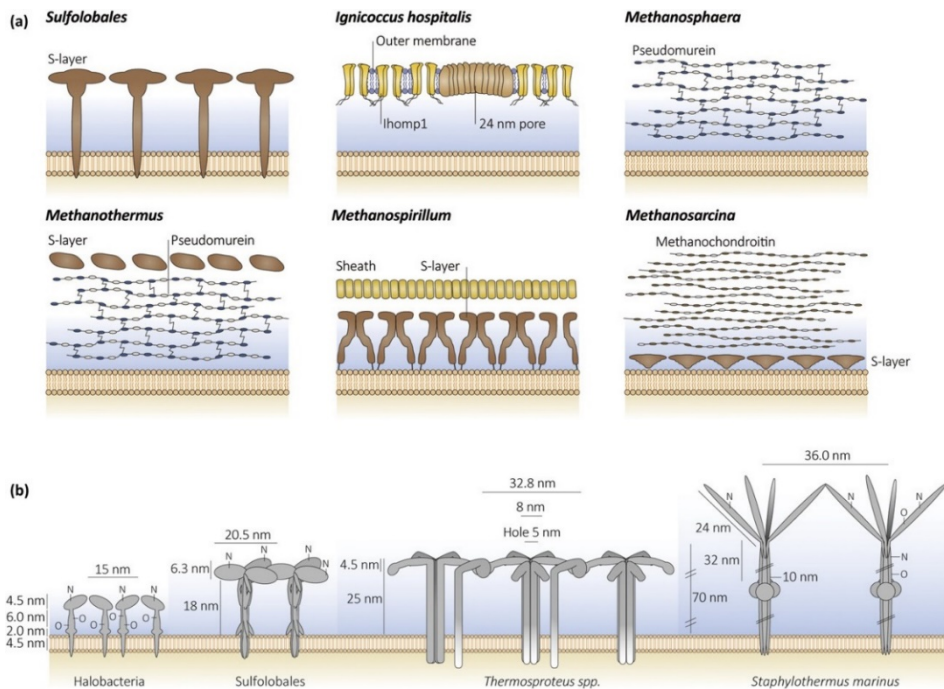


Figure 4. (a) Schematic side view of cell envelopes of exemplarily archaea. LPS, Lipopolysaccharides. (b) Models of the archaeal S-layer inside view. N, N-linked glycosylation; O, O-linked glycosylation. Reproduced from (13).

Cell Shape

Bacteria and archaea exhibit a broad diversity of cell shapes and cell sizes (Fig. 5). These features are tightly controlled through elaborate cell division machineries and structural features that maintain their intrinsic morphology. While some archaea share both structural and cell division components with bacteria, others have systems homologous to eukaryotic division machineries.

For most bacteria, the PG is both essential and sufficient to regulate and maintain their shape. However, how the PG synthesis is orchestrated to result in a particular shape is not well understood for most morphologies and organisms. In general, it is believed that cytoskeletal elements direct the PG synthesis machinery to the appropriate positions. In *Escherichia coli*, the actin-like cytoskeletal protein MreB coordinates localization of the PG synthesis machinery and, consequently, the insertion of PG precursors. MreB itself preferentially localizes to regions of negative curvature. The insertion of PG at these sites results in the growth of *E. coli* as a straight rod. In some cases, the cytoskeleton may play a more active role in shaping a cell. The vibrioid cell shape of *Caulobacter crescentus* is the result of crescentin, a

homologue to eukaryotic intermediate filaments. This protein coats the inner curvature of the cytoplasmic side of the CM. In contrast to coccoid spheres, alternative cell shapes offer the possibility of subcellular organization. In rod shaped cells for example the cell can distinguish between polar and midcell regions. In some bacteria, structures required for motility and chemosensing are predominantly found at one or both poles of the cell. The differently curved membrane at the pole can establish polarity of bacterial cells, and landmark proteins can recruit further proteins to the pole or protein gradients along the axis of the cell.

The cell shape maintenance in archaea is less well understood. CetZ, a protein related to eukaryotic tubulin and bacterial FtsZ, was shown to be essential for the development of rod-shaped *Haloferax volcanii* cells. This protein forms an additional layer underneath the membrane in cells producing high levels of this protein.

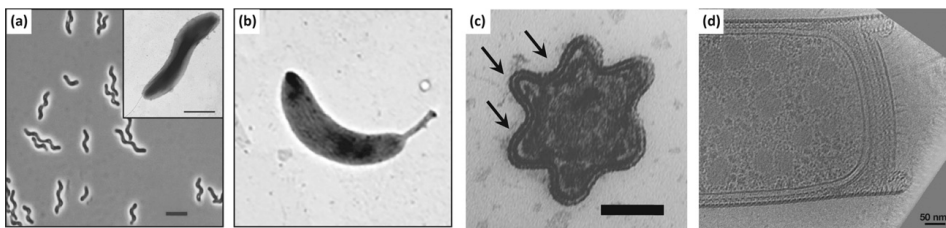


Figure 5. Diverse bacterial and archaeal morphologies. (a) Uncharacterized spiral-shaped methanotroph. Phase contrast with inset electron micrograph. (b) Transmission electron micrograph of *C. crescentus* (c) ultrathin section TEM micrograph of a six-pointed starshaped bacterium. (d) Cell tip of *Methanospirillum hungatei* cells imaged by cryo-electron microscopy. Modified from (a) (17), (b) (18), (c) (19), and (d) (20).

Cell Division

With few exceptions, the cell division machinery is necessary to reliably divide a cell into two daughter cells of similar volume and content. In nearly all bacteria, cell division is orchestrated by the tubulin homologue FtsZ. This specialized cytoskeletal element assembles into circumferentially orientated, overlapping filaments at the cytoplasmic side of the CM, which marks the division site and provides an assembly platform for the cell division machinery (Fig. 6). In Gram-positive bacteria, cell division occurs by septation. Here, the CM is pulled inwards and two new PG layers grow in parallel into the septum. At the outer rim of the septum, a PG bridge connects the old cell wall material of the mother cell both to each other as well as to new PG layers. Once septation is complete, the two daughter cells are fully

separated and split from each other. Division of Gram-negative bacteria follows a similar scheme with some variations. The constriction of the Gram-negative cell envelope starts either symmetrically, or asymmetrically at one side of the cell, before occurring circumferentially. Additionally, instead of forming a compact thin septum, the OM and PG lag behind the CM that moves into the center of the cell first, forming a V-shaped constriction. Here, the hydrolysis and synthesis of the PG bridge is speculated to be more controlled as it needs to move inward following the FtsZ ring while preventing premature rupture.

Archaea also divide by binary fission but exhibit a higher diversity of systems and modes of cell division than bacteria. Most *Euryarchaeota*, *Thaumarchaeota*, *Nanoarchaeota* and *Korarchaeota* encode an FtsZ-based division machinery, while the *Crenarchaeota* possess a system homologous to the eukaryotic endosomal sorting complex required for transport III (ESCRT-III). Cell division of these archaea may occur either symmetrically or asymmetrically.

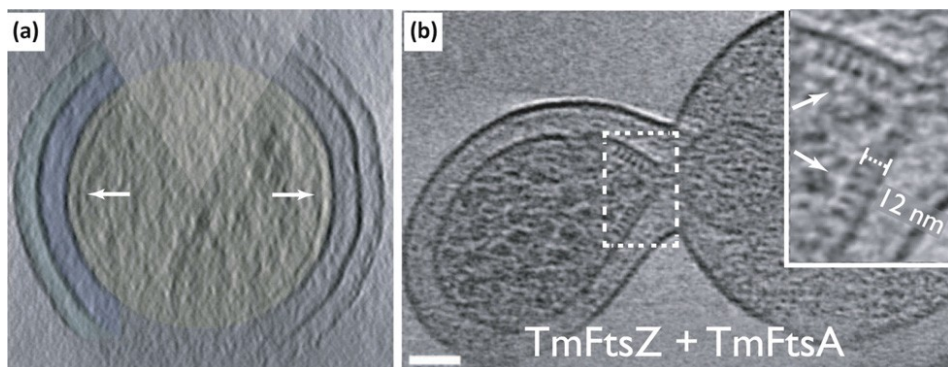


Figure 6. (a) FtsZ forms bands of filaments completely encircling *C. crescentus* NA1000/CB15N division site with filaments near the inner membrane IM. The Z ring (arrow) is continuous. The cytoplasm (beige), periplasm (blue), and space between the OM and S layer (cyan) have been colored for clarity. (b) 10-nm thick electron cryotomographic slice of an *E. coli* minicell formed from cells expressing *Thermotoga maritima* FtsZ and FtsA proteins, with a deeply constricted area showing cross-sections of FtsZ and FtsA filaments (black dots marked with white arrows). Distance between FtsZ filaments and IM is around 12 nm (inset in b). (a & b). Modified from (21).

Interaction with the Environment

Bacteria and archaea have developed an extraordinary arsenal of molecular machinery to interact with, as well as influence, the environment around them. The cells are able to sense their surroundings, determine the levels of nutrients, change the environmental milieu, and provide defenses for themselves and their neighbors. The following sections describe how bacteria and archaea interact with

their environment, highlighting the roles of motility apparatus, membrane vesicles, secretion systems, pili and, hami.

Motility

Some of the most striking structural features of bacteria and archaea are the proteinaceous ultrastructures required for cellular motility. Several distinct types of motility machineries have evolved in microorganisms, each adapted to a certain lifestyle and environment.

Swimming motility

Due to their small size, viscous forces are predominantly influencing microorganisms that move through water bodies. Therefore, reciprocal movements do not propel the cell. Bacteria and archaea solve this problem by using long rotating filaments that generate a fluid flow. Surprisingly, the bacterial flagellum and the archaeal archaellum have evolved separately, although they facilitate the same task.

The overall architecture of the flagellum can be divided into three major parts: The long helical filament extending from the cell body, a flexible hook and the envelope embedded basal body which comprises the rotary motor. Although the principal flagellar components are conserved among all flagellated bacteria, further proteins can modify the flagellar motor properties. Several additional periplasmic discs and ring structures are found to provide an increased structural support as well as a scaffold that allows more stators to be included in the motor. This results in increasing widths of the C- and stator ring (Fig. 7(a-i)). Both features allow cells to swim at a higher speed and torque.

Due to a similar assembly mechanism and homology of some components, the archaellum structurally resembles bacterial type IV pili (T4P) rather than the flagellum. Contrary to the flagellar filament, the archaellum is not hollow. Here, the prepilins are assembled into the pilus at the base of the growing archaellum. The motor is a multiprotein complex, however, rotation of the archaellum is powered by ATP hydrolysis and not by an ion-flux. While recent advances have elucidated the structure of the archaellum, several components and functions remain to be defined (Fig. 7(k and l)).

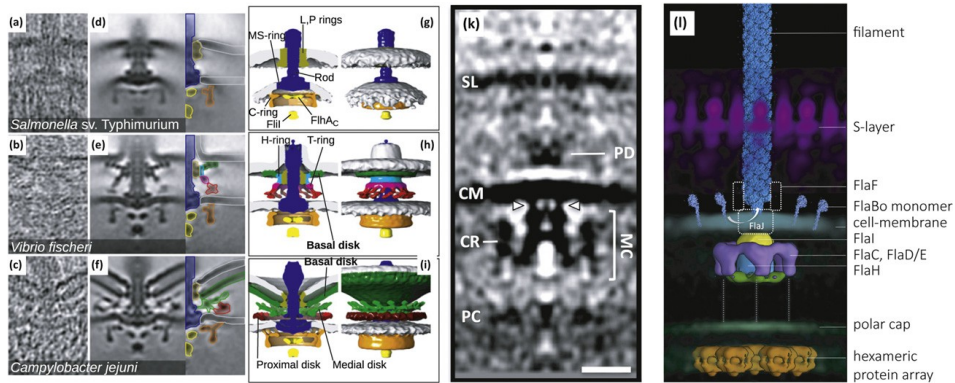


Figure 7. High-torque bacterial flagellar motors assemble large periplasmic disk complexes. (a–c) Tomographic slices through intact cells of *Salmonella* (a), *V. fischeri* (b), and *C. jejuni* (c) showing individual flagellar motors. (d–f) Slices (100 x 100 x 0.81 nm) through subtomogram averages of hundreds of motors. Color keys indicate the regions of the motor (named in g–i), (g–i) Isosurface renderings of motors shown in (d–f). Flil and FlhAC are components of the flagellar type III secretion system. (k) Tomographic slice through the subtomogram average of the motor complex of the archaellum of *Pyrococcus furiosus*. SL, S-layer; PD, periplasmic densities; CM, cell membrane; MC, motor complex; CR, cytosolic ring; PC, polar cap. Arrowheads indicate two of six narrow connections between MC and CM. (l) Composite model of the archaellum machinery of *P. furiosus*. Light blue, FlaB0 monomers and filament; hazy magenta, S-layer; solid yellow, blue, green, and purple, motor complex; hazy blue, cell membrane; hazy green, polar cap; solid orange, hexagonal protein array. Putative positions of protein subunits are indicated. Dashed grey lines, putative interaction with polar cap. (a–i). Modified from (22). (k & l) (23).

Surface Motility

Besides being required for attachment and biofilm formation, several bacteria possess retractile T4P that can attach to a surface and pull the cell towards the attachment point. This form of motility is referred to as twitching motility. Assembly of the pilus results in its extension, while the disassembly results in its retraction. Both processes depend on ATP hydrolysis. In several organisms, a specialized ATPase facilitates the depolymerization. Non-retractile and retractile T4P are structurally very similar.

An additional surface motility mechanism has been described for *Myxococcus xanthus*. The structural requirements of the so-called gliding motility, known as adventurous or A-motility, are not entirely understood. The current model of this mode of motility is based on the consecutive adhesion of OM lipoproteins to a surface, followed by the movement of the cell relative to that adhesion point, and the final release and disassembly of the lipoprotein complex at the lagging end of the cell. The involved protein complex appears to span the entire cell envelope. The release of a slime further facilitates the movement across the substratum.

Chemotaxis

In order to optimally benefit from the ability to move through the environment, many bacteria and archaea can sense their chemical environment and control their motility accordingly. This allows the cells to seek out their preferred environment and evade potentially harmful conditions.

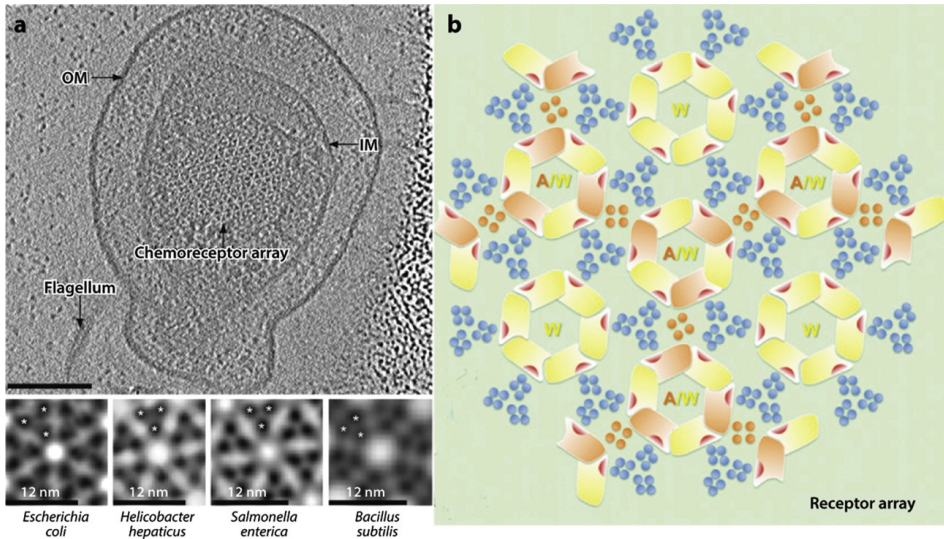


Figure 8. Visualization of the highly structured chemotaxis array by cryogenic electron microscopy (cryo-EM) in *Salmonella enterica* mini cells. (a) Viewed from the top, the chemotaxis array assumes a lattice formation (top) that is universal among bacteria (bottom). (b) Illustration of the chemotaxis array highlighting key proteins and their interacting partners that maintain the array: CheA (A, orange), methyl-accepting chemotaxis protein trimers (blue) and CheW (W, yellow). Scale bar in A (top) is 100 nm. Outer membrane (OM), inner membrane (IM). Modified from (24).

Chemotaxis is best understood in the model organism *E. coli*. Here, the cells can sense environmental cues such as sugars, amino acids or toxins via chemoreceptors that are anchored in the CM. The receptors, or MCPs (for Methyl accepting chemotaxis proteins), form trimer-of-receptor dimers, and these trimers are in turn arranged in highly ordered arrays, where six trimers form the corners of a hexagon (Fig. 8). This receptor packing, and thus the distance between the centers of the hexagons of 12 nm in the lattice, is highly conserved and universal across the bacteria and archaea.

In *E. coli*, the cytoplasmic tips of the receptors are networked by rings formed by the histidine kinase CheA and the linking protein CheW. CheA autophosphorylates and transfers this phosphoryl group to a messenger protein CheY upon an increase of repellents or a removal of attractants. The phosphorylated messenger protein CheY binds to the flagellar motors and biases the direction of flagellar rotation from

the default counterclockwise (CCW) to clockwise (CW). This results in a tumbling behavior where the cells randomly reorient their cell axis. Once all flagella of the cell return to CCW, the cells swim smoothly forward (run) in a new direction. The control of frequency and duration of these tumbles result in a biased random walk, which ultimately provides the means to find their preferred environment.

While *E. coli* only possesses one chemotaxis system, more than half of all chemotactic bacteria have additional chemotaxis systems encoded in their genome. Some of these systems lack the transmembrane and periplasmic regions of the receptors, and thus form purely cytoplasmic chemoreceptor arrays. Structurally, these arrays consist of two layers, where each layer is hexagonally packed like their membrane-bound counterparts. The receptors of both layers overlap and are sandwiched in between two layers composed of CheA and CheW. While we are beginning to understand the architecture of such cytoplasmic arrays, their function remains largely unclear.

Membrane Vesicles

Membrane vesicles are an essential component found in both Gram-positive and Gram-negative bacteria, as well as in archaea (also referred to outer membrane vesicles in gram negative bacteria). These vesicles are typically spherical, ranging in size from 20 to 100 nm in Gram-positive bacteria and archaea to 100–300 nm in Gram-negative bacteria (Fig. 9). The lipid bilayer composition of the vesicles resembles that of the membrane where the vesicle originated. They can contain cell-wall material, as well as a variable content enclosed by the membrane. In addition, the content of membrane vesicles can be enriched with a diverse set of molecules including LPS, peptidoglycan, nucleic acids, metabolites, and signaling molecules. The mechanism by which membrane vesicles are generated is still under investigation.

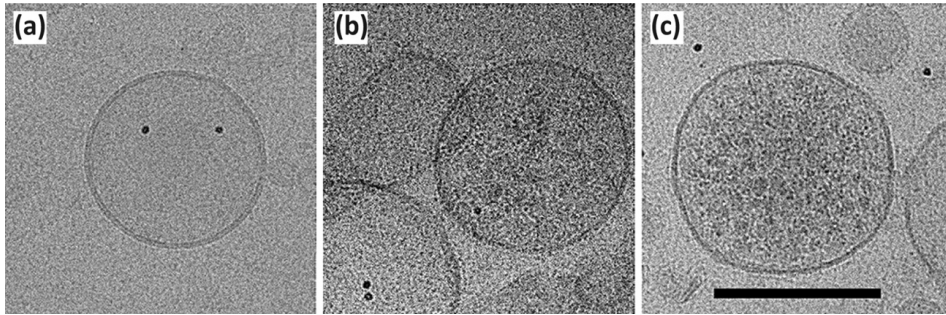


Figure 9. Cryo-EM of membrane vesicles isolated from *Streptomyces*, demonstrating the variety of sizes and variability in contents. Three types of vesicles are noted: Empty (a), partially filled, with or without external membrane complexes (b), or heavily filled with material (c). Scale bar 200 nm. Modified from (25).

Membrane vesicles have many proposed functions: bacterial communication, modulation of stressful environments, components for biofilm formation, and defense strategies. The membrane vesicles can be filled with specialized cargo that elicit specific types of response, including the recognition of self and non-self organisms. For the acquisition of nutrients, outer membrane vesicles (OMVs) can be filled with proteases and glycosidases, or with DNA and proteins that can be a source of food for the community. Recent studies have also demonstrated that interactions with specific hosts can bias the proteins found in membrane vesicles to those that are important to the bacteria-host relationship, including adhesions for binding to specific cell types. For instance, the Gram-positive bacteria *Staphylococcus aureus* produce membrane vesicles that contain beta lactamase as a way to protect the local environment from the antibiotic penicillin. In addition, membrane vesicles have also been shown to provide a defense against bacteriophage infection by acting as a decoy. Thus, membrane vesicles play an essential role in the bacterial and archaeal life cycle by modulating the environment in favor of their survival.

Secretion Systems

In addition to releasing membrane vesicles into the environment, bacteria and archaea have developed various mechanisms to transport unfolded or folded proteins across their membrane(s) and into the local environment or across the membrane of a target cell. Some systems allow a protein to move from the cytoplasm directly to the extracellular space in a one-step process. Others require several steps for the target protein to exit the cell via a transport system through the CM, followed by a second transport system that spans the OM and/or cell wall. Upon translocation, the proteins remain either attached to the cell envelope, are

released into the extracellular space, or are transferred directly into the target cell. Thus far, as many as sixteen unique complexes have been shown to be involved in protein transport across the membrane. Each system plays a specific role in bacterial and archaeal physiological processes. Furthermore, these systems are the primary method for the release of bacterial effector proteins that act on other cells in the environment. Some secretion systems are universal among bacteria and archaea, such as the Sec and Tat pathways, while others are restricted to a specific phylum or species. The same is true for the cargo of each system, some transporting a wide range of proteins and others are specific to just a small number of proteins. The secreted proteins have many roles in the bacterial and archaeal life cycle, including uptake of nutrients, expression of virulence factors, and attachment to target cells. Gram-negative bacteria have multiple secretion systems: Sec, Tat, type 1 secretion (T1SS), T2SS, T3SS, T4SS, T5SS, T6SS, and T9SS. Gram-positive bacteria have at least four systems, Sec, Sec2A, Tat, and T7SS, and only Sec and Tat have been identified in archaea so far. Because of the large number of secretion systems across bacteria and archaea, this section will highlight only those systems with significant ultrastructural information.

Type II Secretion System

The type II secretion system (T2SS) is only found in Gram-negative bacteria where it is responsible for secreting folded proteins from the periplasm through the OM. Proteins that are destined for the T2SS are first transported in an unfolded state across the CM by the Sec or Tat systems. Once in the periplasm, the protein is folded and then transported into the extracellular space by the T2SS. This secretion system is an important component in pathogenesis, and many pathogens utilize this pathway to deliver toxins to target cells. A well-studied example of this mechanism is the transport of the cholera toxin during *Vibrio cholerae* infection. The T2SS is thought to work by a piston mechanism, where the cholera toxin is mounted to a platform on the periplasmic side of the CM and then pushed through the OM pore. This export is powered by the retraction of the pseudopilins (Fig. 10).

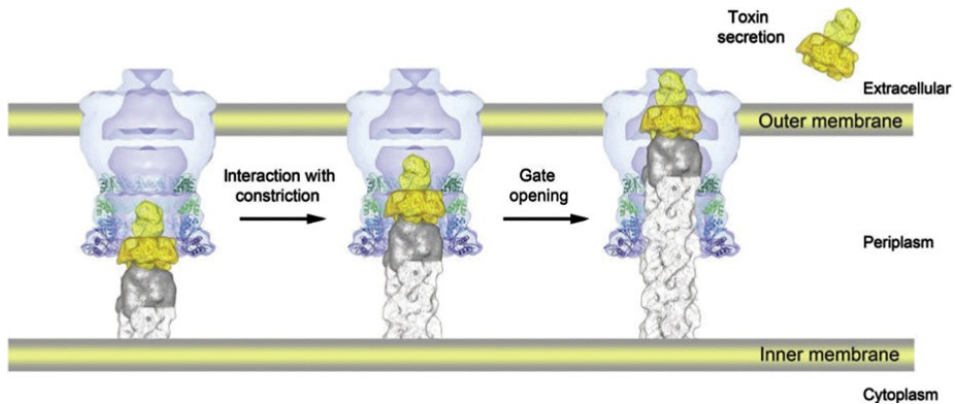


Figure 10. Schematic representation of the secretion of *V. cholerae*'s cholera toxin by a piston-driven mechanism of the T2SS. Cholera toxin (gold) is loaded on the pseudopilus tip (grey). The toxin is then pushed into the periplasmic portion of the membrane channel by the extension of the pseudopilus. Secretion of the toxin is permitted by the opening of the membrane channel and continued growth of the pseudopilus. Modified from (26).

Type III Secretion System

The type III secretion system (T3SS) is also known as the injectisome because its structure resembles a needle and syringe and acts in a similar fashion. This system is found exclusively in Gram-negative bacteria, where it spans the whole cell envelope, as well as the membrane of its target cell. This provides the opportunity for the transport of unfolded proteins directly into the target cell. This transfer of bacterial effectors typically facilitates the creation of a more favorable environment for the delivering bacteria. Three main components of the T3SS have been characterized: the basal body, the needle and the translocon. The needle extends from the base into the extracellular space and consists of a hollow channel that permits transport of unfolded proteins. The translocon is responsible for the transport of effector proteins upon contact with the target cell. The T3SS has been structurally well characterized, and recent studies provided detailed insight into the structural variations of the T3SS in *Chlamydia* and *Salmonella* (Fig. 11).

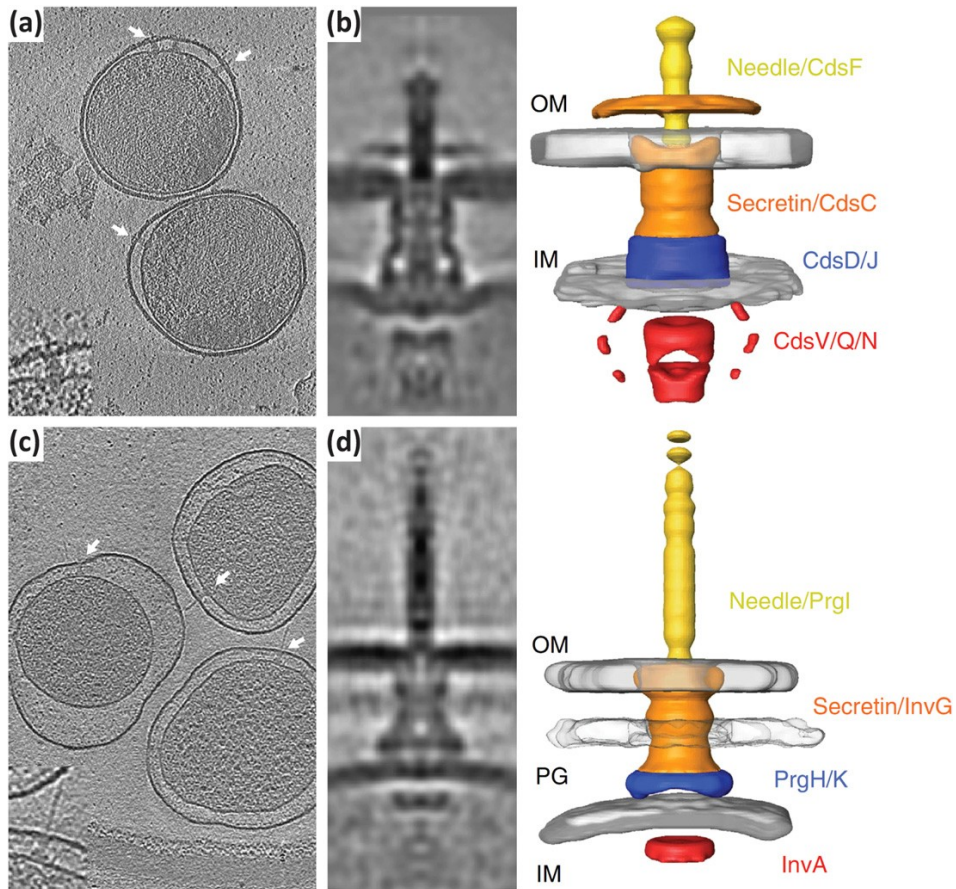


Figure 11. Cryo-EM visualization of the T3SS obtained from *Chlamydia trachomatis* elementary bodies (a, b) and *Salmonella enterica* minicells (c, d). The T3SS apparatus spans the inner and outer membranes (a, c; white arrows). Further image processing provides a detailed view of the T3SS structure (b, d) and can be represented by both electron micrographs (left) and 3D surface rendering (right). OM – outer membrane, PG – peptidoglycan, IM – inner membrane. Scale bars, 200 nm (a, c) and 15 nm (b, d). Modified from (27).

Type IV Secretion System

The function of the type IV secretion (T4SS) system is used for bacterial conjugation, where it enables the cells to secrete a wide variety of molecules including single stranded (ss) DNA and ssDNA-protein complexes directly into a target cell. There are two types of T4SS: the retractable T4aSS and the non-retractable T4bSS. The T4SS spans the CM and OM of Gram-negative bacteria as well as the membrane of the target cell. The secretion system provides the means to export and import DNA, and thus contributes to spread of antibiotic resistance genes. The structure of the T4SS is similar across all identified T4SS variants, though the role of an extracellular pilus in some systems is still unknown. This system is important for virulence in

many bacteria, such as in the pathogen *Legionella pneumophila*, where the structure of this T4bSS has been recently solved (Fig. 12). In this organism, the T4bSS transports effectors into the target cells in order to disrupt the host's defense, and thus enabling bacterial colonization.

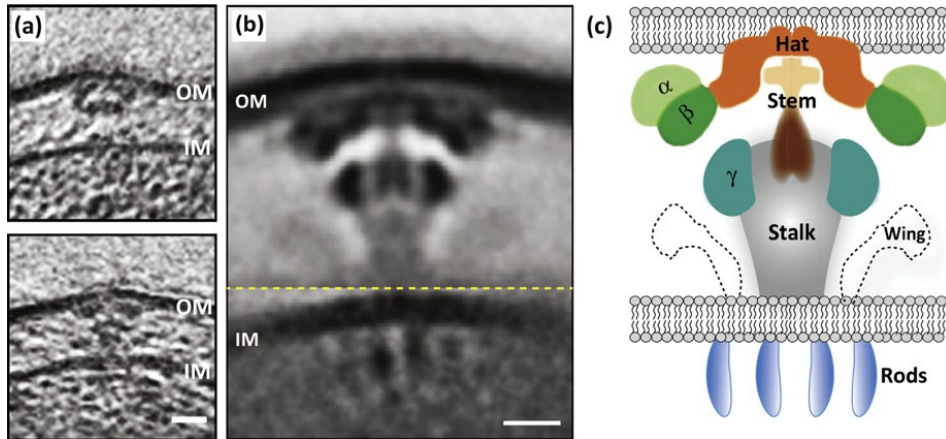


Figure 12. Cryo-EM and advanced image processing reveal the in vivo structure of the T4bSS of *Legionella pneumophila*. The T4bSS spans the outer and inner membrane (OM, IM) of the cell (a) Subtomogram averaging clarifies the structural features (b) and is fitted with known protein components that comprise the complete T4bSS structure (c) Scale bars: 20 nm (a) and 10 nm (b) Modified from (28).

Type VI Secretion System

Similar to the T3SS, the type VI secretion system (T6SS) transports proteins from the bacterial cytoplasm directly into the target cell. Found only in Gram-negative bacteria, this system is thought to be both a form of communication and competition among various bacteria. The T6SS secretes bacterial toxins either into other bacterial cells in the local environment, or into eukaryotic cells. The T6SS is highly efficient in protein transport, and it provides the cells with both defensive and offensive protection against other bacteria that also employ the T6SS. In addition, this system has been implicated in bacterial response to stress and for self-recognition. Furthermore, it contributes to horizontal gene transfer, since it uses this system to kill opponent cells. The resulting lysis frees the DNA that can subsequently be taken up by other secretion systems.

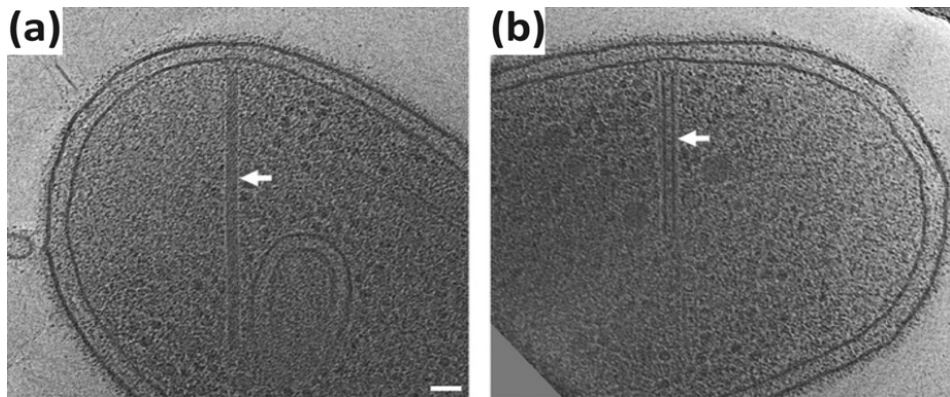


Figure 13. Visualization of the T6SS in vivo by cryo-EM. The T6SS in the extended (a) and contracted state (b) in *Myxococcus xanthus*. The extended version spans a significant portion of the cell and once triggered contraction delivers effectors to the target cell. Scale bar: 50 nm. Modified from (29).

The T6SS is homologous to the tail structure found in bacteriophages. Structurally, the base of the T6SS is anchored to the CM, and upon contraction of a sheath-like structure, the inner tube is propelled into a target cell, puncturing the target cell's membrane with a spike-like protein tip. A well-studied structural model for the T6SS comes from *M. xanthus*. In this organism, the T6SS is characteristic tube-shaped structure within the cell (Fig. 13(a)). The tube structure is extended into the cytoplasm and anchored to the CM. Upon external trigger the sheath of the tube constricts propelling bacterial effectors into the target cell. In the bacterium *Pseudoalteromonas luteoviolacea*, a structure termed the MAC complex induces metamorphosis in tube worms. Here, the T6SS form a large array of tubes held together by a protein mesh, that are released into the environment and act as 'land mines' that induce the metamorphosis of the tube worm.

External Appendages

Pili (Also Known as Fimbriae)

Bacteria and archaea have evolved a number of external appendages that can be used for attachment, secretion, electron uptake, and motility. Such structures include four types of pili. Gram-positive and Gram-negative bacteria have similar types of pili, however their fine structures differ. The chaperone-usher pili are mainly found in Gram-negative bacteria and are used for host attachment and virulence. Chaperone-usher pili are typically 1–2 μm in length with the pilin subunits arranged in a helical pattern. This pilus architecture provides the ability to stretch.

In addition to the functions mentioned for the chaperone-usher pilus, the type 4 pilus (T4P) is also involved in twitching and gliding motility. T4P can be several microns in length with a diameter of 6–9 nm. T4P are unique among the pili because some variants have the ability to extend and retract, which provides the means for the cell's motility. During assembly, pilins are removed from the CM and assembled in the periplasmic space by the T4P basal body, causing the filament to extend out into the extracellular space. There are two types of T4P, Type IVa (T4aP) and Type IVb (T4bP). T4aP has a range of functions including cell motility and DNA transfer, while T4bP is specifically used for host colonization. The Gram-negative organism

V. cholerae has a unique, well-studied form of the T4bP called the toxin co-regulated pili (TCP). The TCP is essential to the *V. cholerae* infection cycle, providing a means of attachment for the bacterium when it enters the mucosal regions of its host. Additionally, it enables the cells to form microcolonies. The different T4P types are remarkably similar in composition and structure, though only T4aP have the ability to retract (Fig. 14). TcpA is the major pilin subunit for both systems, which forms the extracellular appendage.

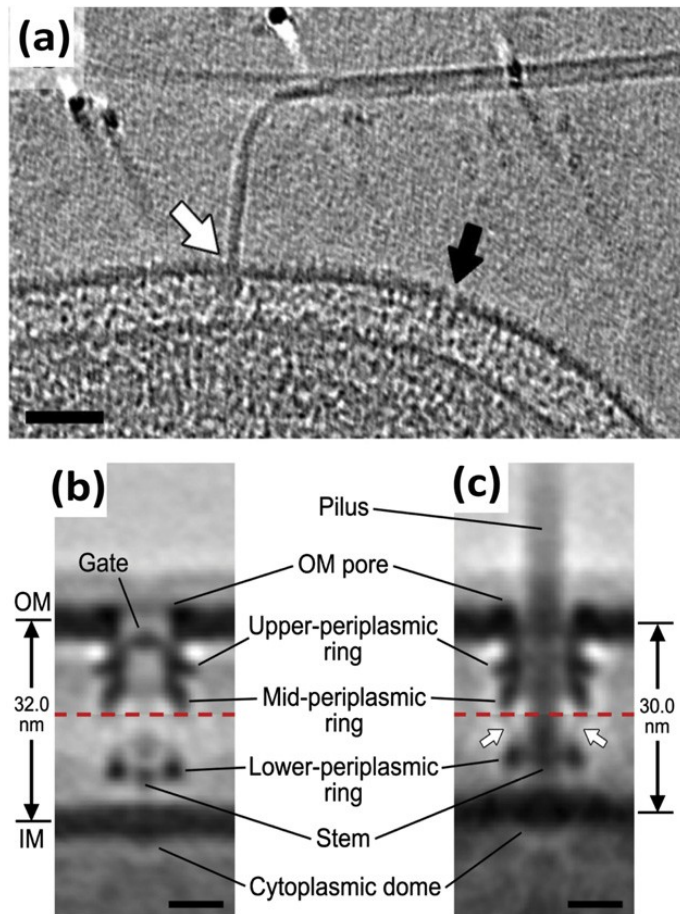


Figure 14. T4P. *V. cholerae* exhibits a unique type IV pilus apparatus called the toxin-co-regulated pilus machine (TCPM). A. Using cryo-EM, the piliated TCPM (white arrow) and non-piliated basal body (black arrow) are identifiable on the cell surface. Image processing enables the user to gain greater detail of the TCPM allowing the comparison of the piliated (b) and non-piliated states (c). Scale bars: 50 nm (A), 10 nm (B, C). Modified from (30).

The conjugative T4P pilus, also called F-pilus or F-like pilus, is the primary method used between bacteria for the transfer of genetic information. This structure is present only in Gram-negative bacteria and requires a specific plasmid that codes for the essential components of this conjugative pilus. This system is unique as it requires the use of a T4SS for assembly. The current model of this system is that once two cells are connected, the pilus is retracted in order to bring the two cells together, thus allowing for the transfer of genetic material.

Lastly, the type 5 pili (T5P) are unique to the *Bacteroides* phylum, consisting of two types of pilin appendages: a long pilus that extends approximately 0.3–1.5 mm from

the cell body, whereas the short pilus is restricted to 80–120 nm. This pilus type has several roles including adhesion, aggregation, biofilm formation, and virulence.

Other Cell Attachment Structures

Hami

Some archaea, such as the *Candidatus Altarchaeum hamiconexum*, have an additional, unique appendage that is used for attachment to surfaces, other cells, as well as important in biofilm formation in extreme environments. Upwards of a hundred of these pilus-like structures extend from the cell surface, with each hamus having a diameter of 6–8 nm and protruding several microns into the environment. The hami are made of three intertwined filaments. The hamus terminates in a characteristic tripartite structure that resembles a grappling hook (Fig. 15). Many hami have three barbs emerging approximately 47 nm apart along the main thread. The assembly of this structure is thought to be mediated by the Sec pathway, moving the three subfilaments into the periplasm for hamus assembly. However, the filaments are not related to known bacterial filaments and recent research suggests that it may have evolved from modified S-layer proteins.

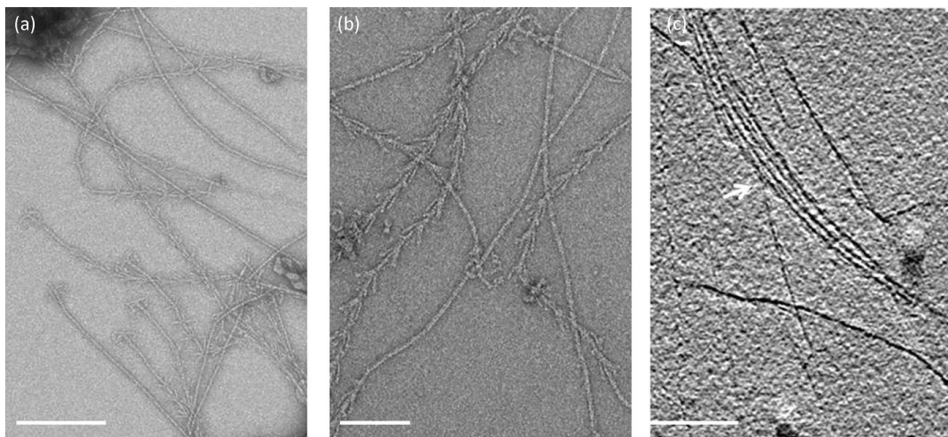


Figure 15. The archaeal hami of *Candidatus Altarchaeum hamiconexum* visualized by negative stain EM (a, b) and cryo-electron tomography (c) demonstrating the characteristic barbed structure filament with tripartite tips. Scale bar: 500 nm. Reproduced from (31).

Further Reading

- Adams, D.W., Errington, J., 2009. Bacterial cell division: Assembly, maintenance and disassembly of the Z ring. *Nature Reviews Microbiology* 7 (9), 642–653. doi:10.1038/nrmicro2198. (32)
- Albers, S.-V., Meyer, B.H., 2011. The archaeal cell envelope. *Nature Reviews Microbiology* 9 (6), 414–426. doi:10.1038/nrmicro2576. (13)
- Briegleb, A., Jensen, G., 2017. Progress and potential of electron cryotomography as illustrated by its application to bacterial chemoreceptor arrays. *Annual Reviews of Biophysics* 46, 1–21. doi:10.1146/annurev-biophys-070816-033555. (24)
- Caccamo, P.D., Brun, Y.V., 2018. The molecular basis of noncanonical bacterial morphology. *Trends in Microbiology* 26 (3), 191–208. doi:10.1016/j.tim.2017.09.012. (33)
- Chang, Y., Kjaer, A., Ortega, D., et al., 2017a. Architecture of the *Vibrio cholerae* toxin-co-regulated pilus machine revealed by electron cryotomography. *Nature Microbiology* 2, 16269. doi:10.1038/nmicrobiol.2016.269. (30)
- Chang, Y., Rettberg, L.A., Ortega, D.R., Jensen, G.J., 2017b. In vivo structures of an intact type VI secretion system revealed by electron cryotomography. *EMBO Reports* 18 (7), 1090–1099. doi:10.15252/embr.201744072. (29)
- Ghosal, D., Chang, Y., Jeong, K.C., et al., 2017. In situ structure of the *Legionella* Dot/Icm type IV secretion system by electron cryotomography. *EMBO Reports* 18 (5), 726–732. doi:10.15252/embr.201643598. (34)
- Green, E.R., Mecsas, J., 2015. Bacterial secretion systems: An overview. *Microbiology Spectrum* 4 (1), doi:10.1128/microbiolspec.VMBF-0012-2015.
- Harshey, R.M., 2003. Bacterial motility on a surface: Many ways to a common goal. *Review of Microbiology* 57 (1), doi:10.1146/micro.2003.57.issue-1. (35)
- Hospenthal, M.K., Costa, T.R.D., Waksman, G., 2017. A comprehensive guide to pilus biogenesis in Gram-negative bacteria. *Nature Reviews Microbiology* 15, 365–379. doi:10.1038/nrmicro.2017.40. (36)
- Kearns, D.B., 2010. A field guide to bacterial swarming motility. *Nature Reviews Microbiology* 8 (9), 634–644. doi:10.1038/nrmicro2405. (37)
- Kim, J.H., Lee, J., Park, J., Gho, Y.S., 2015. Gram-negative and Gram-positive bacterial extracellular vesicles. *Seminars in Cell & Developmental Biology* 40, 97–104. doi:10.1016/j.semcdb.2015.02.006. (38)

Nans, A., Kudryashev, M., Saibil, H.R., Hayward, R.D., 2015. Structure of a bacterial type III secretion system in contact with a host membrane in situ. *Nature Communications* 6, 10114. doi:10.1038/ncomms10114. (27)

Perras, A.K., Daum, B., Ziegler, C., et al., 2015. S-layers at second glance? Altiarchaeal grappling hooks (hami) resemble archaeal S-layer proteins in structure and sequence. *Frontiers in Microbiology* 6, 543. (31)

Reichow, S.L., Korotkov, K.V., Hol, W.G.J., Gonin, T., 2010. Structure of the cholera toxin secretion channel in its closed state. *Nature Structural & Molecular Biology* 17 (10), 1226–1232. doi:10.1038/nsmb.1910 1226. (26)

CHAPTER 3

An economical, portable manual
cryogenic plunge freezer for the
preparation of vitrified biological
samples for cryogenic electron
microscopy

This chapter is published as:

Depelteau JS¹, Koning G², Yang W¹, Briegel A¹. (2020). Microscopy and Microanalysis, 26(3):413-418

¹ Microbial Biotechnology & Health, Institute of Biology, Leiden University, Leiden, The Netherlands

² Fine Mechanics Department, Faculty of Science, Leiden University, Leiden, The Netherlands

Abstract

Visualizing biological structures and cellular processes in their native state is a major goal of many scientific laboratories. In the past 20 years, the technique of preserving samples by vitrification has greatly expanded, specifically for use in cryogenic electron microscopy (cryo-EM). Here, we report on improvements in the design and use of a portable manual cryogenic plunge freezer that is intended for use in laboratories that are not equipped for the cryopreservation of samples. The construction of the instrument is economical, can be produced by a local machine shop without specialized equipment, and lowers the entry barriers for newcomers with a reliable alternative to costly commercial equipment. The improved design allows for successful freezing of isolated proteins for single particle analysis as well as bacterial cells for cryo-electron tomography. With this instrument, groups will be able to prepare vitreous samples whenever and wherever necessary, which can then be imaged at local or national cryo-EM facilities.

Introduction

The ability to visualize biological samples such as purified proteins or cellular organisms in a near-native state is the hallmark of cryogenic electron microscopy (cryo-EM). This technique, popularized over the past 20 years, culminated in its recognition by Nature in 2015 and 2016 [single particle analysis (SPA), cryo-EM, 2016; cryo-electron tomography (cryo-ET), and the Nobel Prize in Chemistry in 2017 (39, 40). Cryo-EM was once thought to be available to only a subset of highly specialized laboratories that were able to prepare samples, collect the data, and provide the proper analysis to answer a specific biology question. However, in recent years, more and more laboratories are utilizing this technique, mainly due to the creation of regional and national facilities with experienced staff that help with the steps in the process (41, 42).

The sample preparation step is a key factor for successful cryo-EM experiments, and a growing arsenal of freezing devices is now available. The three most cited automated devices include the Thermo Fisher Scientific (TFS) Vitrobot, the Leica Microsystems EM GP/GP2, and the Gatan Cryoplunge 3 System. Each provides the user with a semi-automated and reproducible process for plunge freezing samples, including temperature and humidity control, adjustable blotting times, and plunging. The user remains responsible for loading the tweezers that hold the grid, applying the sample to the grid, and transferring the vitrified sample to a storage container. The next generation of automated plungers is now entering the market, offering improvements to the sample application and blotting steps, incorporating glow discharging of the grids, automated application of the sample, and/or a variety of other features (e.g., see 43 and 44). However, all these instruments are large, immobile, and/or expensive.

Even research groups who use cryo-EM as the primary technique may encounter problems in sample preparation when the sample cannot be transported to a fully equipped cryo-EM laboratory. This is the case, for example, when the biological samples need to be cultivated in other laboratories under highly specialized conditions or for biosafety reasons. In such cases, it is often advisable or required that the specimen be prepared on site at the collaborating laboratory.

Because of our own need to prepare samples abroad, our laboratory decided to embark on building a portable manual cryo-plunger (PMCP). The goal was to return to a simple, cost-effective, and sturdily designed instrument that can be easily transported between laboratories. With this device, the local/onsite items required for the plunge freezing step are liquid nitrogen for cooling the device and storage

of the frozen samples, a cryogen (typically ethane) to freeze the sample, and the sample itself. Everything else can be transported with the device, including the container (a dry shipper) to ship the frozen samples back to the laboratory for processing. Onsite convenience items would be a screening microscope, such as a 120 keV transmission electron microscope (TEM) capable of evaluating the quality of the cryogenic samples to optimize sample preparation conditions and a glow discharge unit to negatively charge the grids. For the former item, this is not necessary if the group has a significant experience with a similar sample type, has access to a similar sample to optimize preparation in a cryo-EM laboratory, or a combination of both. For the latter, grids can be discharged prior to travel, but the user should determine how long the hydrophilicity will last for each specific combination of the grid type and sample buffer prior to travel.

We based our design on a published device designed to freeze samples in the field (45). We used their designs as a guide for the development of our PMCP. Specifically, we adjusted the total height of the plunger and redesigned the liquid nitrogen container and insert that holds the cryogen container and the grid boxes. In addition, we added several new features, including a submerged storage space for temporary storage of filled grid boxes, the replacement of the single pole between the top and bottom plates with three adjustable rods that allow for precise centering of the tweezers, a more robust polycarbonate shielding surrounding the plunging chamber, and a baseplate that can be clamped to a countertop or surface to provide additional stability.

We tested our PMCP by plunge freezing samples of the bacterium, *Vibrio cholerae*, and evaluated the quality of the vitreous ice and cells to determine if the samples were suitable for cryo-ET. To demonstrate that the PMCP is equally capable for the specimen preparation of protein complexes for SPA, we also tested the performance of our device with equine apoferritin (molecular weight 443 kDa), a protein complex regularly used as a reference standard for SPA. The updated design was successful in plunge freezing both bacteria and protein complexes, producing thin, vitrified ice that is suitable for imaging with a TEM. This design will expand access to cryo-EM by promoting collaboration among cryo-EM and non-cryo-EM laboratories and invites laboratories that want to include cryo-EM in their research techniques for understanding the biological world without the need to purchase expensive commercial equipment.

Materials and Methods

Design and Engineering of a Manual Portable Cryo-Plunger

To begin, we obtained the original designs to the instrument described by Comolli et. al. (45). However, we sought to optimize the design for our specific needs to travel extensively with the instrument and reduce the overall production cost. The final design schematics are outlined in Fig. 1, and representative images of the final device are presented in Fig. 2. A table of approximate costs can be found in Supplementary Table 1. Our first major change was to reduce the total height of the instrument by 150 mm to create a more portable footprint (Figs. 1a–1c, 2a–2c). This was accomplished by reducing the height of the plunging arm and enclosure. We retained the spring-loaded, piston-based, plunging arm from the original design, as this provides the necessary drop speed to minimize evaporation and ensure vitrification of biological samples. However, we found it necessary to add sorbothane (a hard rubber polymer) rings to provide dampening of the tweezers at the end of the fall.

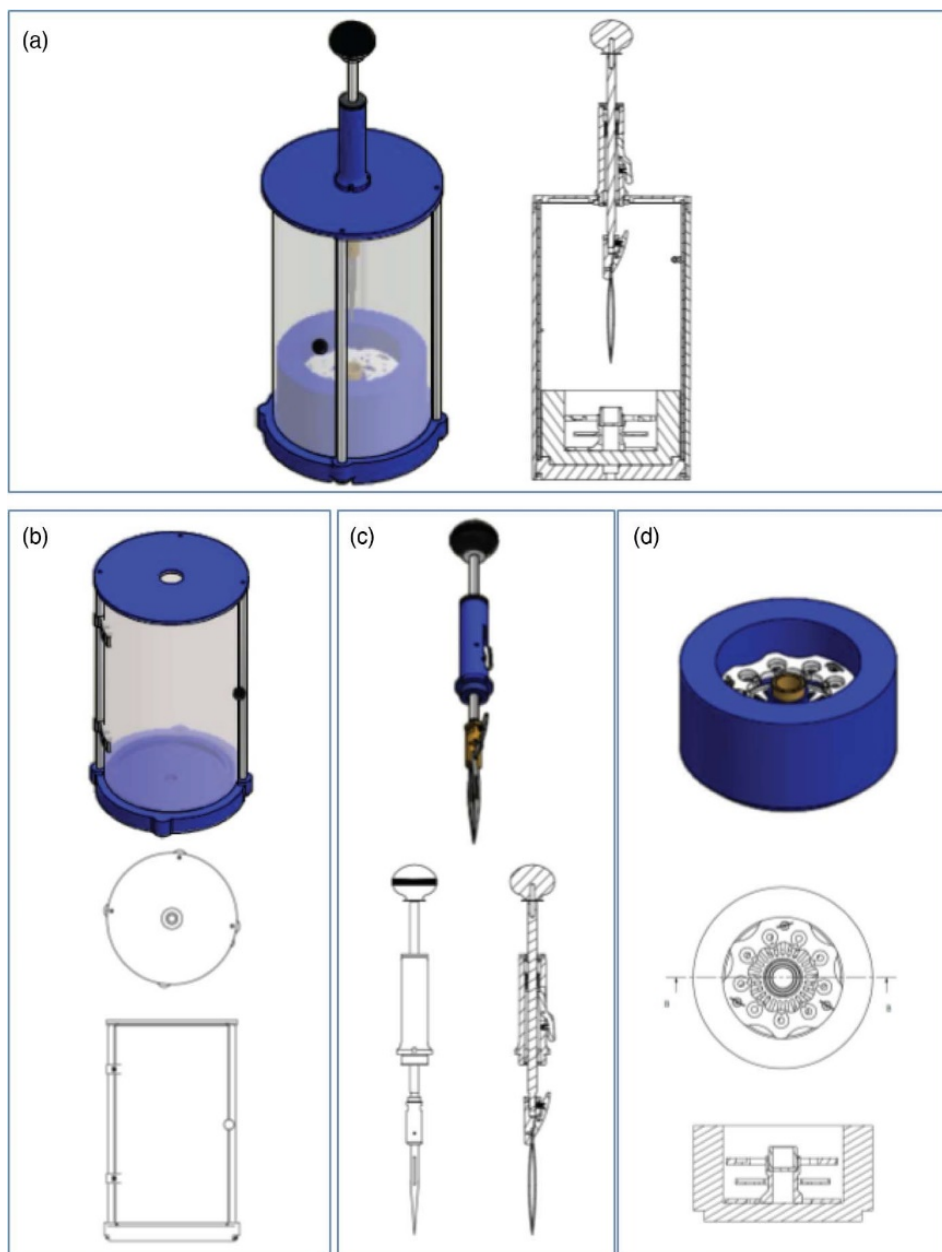


Figure 1. Schematic overview for the components of the PMCP freezer. (a) The assembled PMCP. (b) The body of the PMCP with the top separate because of the need to incorporate the plunging arm and highlighting the door access to the sample area. (c) The spring-loaded plunging arm (spring contained within the blue cylinder) with release lever and tweezers. (d) The cryogen container, which contains three components: the dewar for liquid nitrogen (blue), the grid box storage insert (white), and the cryogen container (gold). Detailed designs are available from <https://briegel-lab.org>.

Next, we replaced the Vitrobot-based cryogen vessel, grid box holder, and liquid nitrogen container (originally from TFS) with a less expensive, combination of commercially available and locally built alternatives (Figs. 1d, 2c, 2d). For the liquid nitrogen container, we chose a lightweight foam cryogenic container (Figs. 2a, 2c; Spearlabs Cryogenic Products). The dewar was customized to fit the base of the plunger. Instead of the “spider design” of the Vitrobot heat exchanger, we incorporated the grid box and a cryogen container holder into a single piece of aluminum (Fig. 2d). As a result, there was no need for multiple parts, while still maintaining the ability to remove the cryogen container from the device at the end of the plunge freezing (which allows for safe evaporation of the cryogen). Furthermore, an extra deep shelf was added to the insert so that the filled grid boxes can be stored completely covered in liquid nitrogen to prevent warming and ice contamination of the samples during lengthy freezing sessions (Figs. 1d, 2c, 2d).

We next decided to improve the stability of the plunger by exchanging the single arm attaching the top and bottom with three adjustable legs, as well as to increase sample protection around the plunger and to add a supporting plate to the bottom of the device (Fig. 2a). The three adjustable legs also allow the user to accurately center the tweezers with respect to the cryogen container. The shield surrounding the device is more user-friendly, as it includes a hinged door, and it is made from a more robust polycarbonate material. The plate can be additionally secured by clamping it to the benchtop, increasing the overall stability of the instrument during freezing. As with the original design, the connection used to attach the plate can also be used to attach the device to a tripod for use in the field.

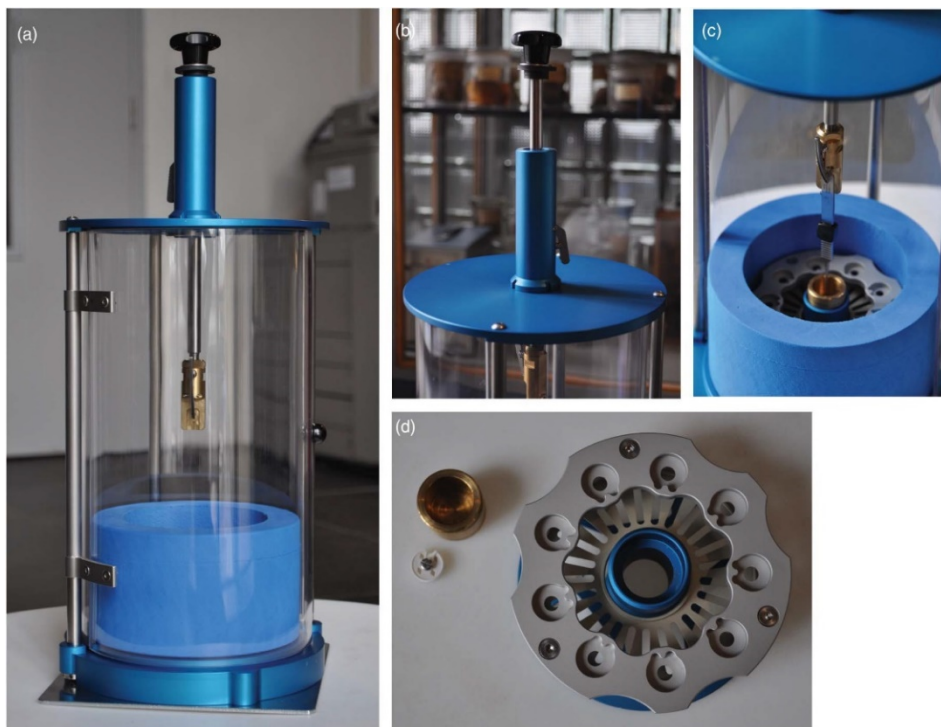


Figure 2. Photographs highlighting different aspects of the PMCP. (a) The assembled PMCP with the plunging arm in the unloading/transport position, shielding door closed, and sitting on the stability plate. (b) The plunging arm in the loaded position, highlighting the release lever of the spring-based plunging mechanism. (c) The position of the tweezers following a press of the release lever, with the tweezers landing in the cryogen cup (gold) of the assembled cryogen container (blue/ silver). (d) Top view of the grid box holder (silver/blue), cryogen container (gold), and representative grid box (white) for comparison.

Lastly, we wanted the device to accommodate the same tweezers (Dumont medical tweezers, clamp style L5) that are used in the commercial devices so that we could exchange the tweezers between the instruments. We adapted the tweezers by drilling a hole in the handle, which is then used to secure the tweezers to the plunger arm.

Once the dimensions of the prototype were finalized, we ordered a custom, padded box to store and transport the instrument (Swanflight.com). We included a separate shelf that allowed for storage of two segmented boxes (Raaco) used for items, such as the tweezers, grid boxes (Molecular Dimensions, UK), and precut pieces of filter paper (Whatman 1) used for manual blotting. The second box is used for spare parts such as additional plunging tweezers, tweezers for transferring the grid boxes, and screwdrivers for tightening the lids of grid boxes.

Testing the Design and Improving the Design

Once we were satisfied with the design, we moved forward with testing of the PMCP. We started with the vitrification of a commonly used bacterium, *V. cholerae*. This curved bacterium is a frequently used sample in cryo-EM studies, as it is naturally thin (ranging from 0.25 to 0.5 μm in diameter and 1–2 μm in length), and it is easily imaged with a screening TEM microscope. In addition, the bacterium has many identifiable features that are apparent in well-prepared samples, such as chemoreceptor arrays, type VI secretion systems, and the flagellar apparatus(46–48).

A typical plunge freezing workflow is as follows: the preparation of the sample to obtain an appropriate concentration in a compatible buffer ready to be pipetted onto the EM grid, cooling of the instrument and cryogen, the application of the sample to a glow discharged grid, incubation, blotting away excess liquid, and plunging the sample loaded grid into the cryogen. Thus, we used a similar process for the PMCP (Supplementary Movie 1). Our sample preparation protocol was to grow a freshly streaked culture of wild-type *V. cholerae* strain A1552 in liquid LB medium overnight at 30°C with shaking at 180 rpm. Once the culture was at an OD600 > 1.3 (typically 12–16 h), 20 μL culture was mixed with 1 μL of 15 nm protein A-treated gold beads (Cell Microscopy Core, Utrecht University, Utrecht, The Netherlands) to produce the sample for freezing. 3 μL of the sample was applied to a glow discharged (25 mA for 60 s, Quorum Q150RS, Electron Microscopy Services) Quantifoil R2/2 Cu 200 mesh grid with extra thick carbon (Quantifoil Micro Tools, GmbH), followed by manual blotting. With manual blotting, it is important to have sufficient lighting to judge the rate of liquid removal. We positioned a light source directly behind the sample to monitor the blotting. Once the liquid halo on the blotting paper stopped spreading, the blot paper was withdrawn within 1 or 2 s, and the lever was immediately depressed causing the sample to drop into the liquid ethane. Vitrified samples were transferred into grid boxes for storage until imaging. A movie demonstrating the blotting process under dry conditions can be found in Supplementary Movie 2.

For the SPA sample, equine apoferritin (Sigma) was diluted into gel filtration buffer [50 mM HEPES (pH 7.5), 150 mM NaCl, 2 mM DTT] and injected onto a Superdex 200 Increase (3.2/300) gel filtration column that was pre-equilibrated in gel filtration buffer. Peak fractions were collected with an OD280 of 1.7, corresponding to a concentration of 2.3 mg/mL. Following purification, 3 μL of the protein sample was applied to a glow discharged Quantifoil R2/2 Cu 200 mesh grid, excess liquid was removed by manual blotting, and the sample was immediately plunge frozen.

For sample screening, we used a Talos L120C (TFS) side entry electron microscope with extended cooling capacity. Samples were inserted into the microscope using a Gatan 626 side entry holder, and images were acquired with a Ceta CMOS camera. For the tomography sample, nominal magnification ranged from 1,200 \times to 22,000 \times , corresponding to a pixel size of 7.97–0.465 nm/pixel (FOV 31.88–1.947 μm^2), respectively. At the highest magnification, defocus used for imaging was $-6\text{ }\mu\text{m}$. For the SPA sample, nominal magnifications used for screening ranged from 380 \times to 92,000 \times , corresponding to a pixel size of 26.4–0.111 nm/pixel (FOV 105–0.444 μm^2), respectively. The apoferritin sample was imaged with settings similar to those that would be used on a Titan Krios: a total dose of 40–50 $\text{e}^-/\text{\AA}$, defocus of $-2\text{ }\mu\text{m}$, and a pixel size of 1.1 $\text{\AA}/\text{pixel}$.

Results

Fig. 3 provides representative images from our sample testing of the PMCP. For these samples, we repeated the standard protocol that we used with our automated plunger but substituted automated blotting for manual blotting as described. For the bacterial sample (Figs. 3a–3c), the ice was clearly vitreous, as demonstrated by a consistent, visually smooth layer across most parts of the grid. On occasion, contamination did occur either from crystalline water or residual frozen ethane. However, most grids had sufficient, similar areas for imaging, and they compared well to our grids prepared by the automated plunger. A progressive zoom in series on the sample supports these conclusions (Fig. 3).

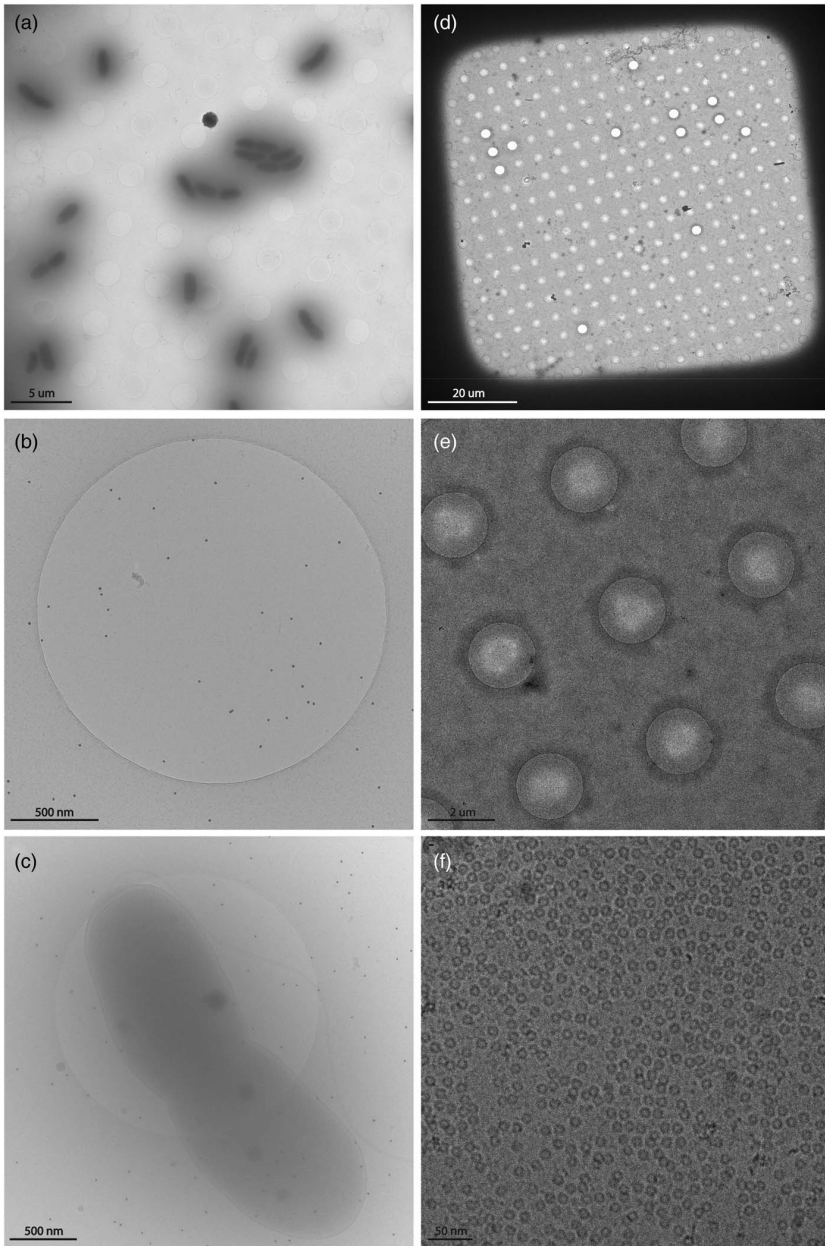


Figure 3. Representative images demonstrating the quality of samples prepared using the PMCP by imaging with a 120 keV TEM. *V. cholerae* sample shows quality of vitreous ice (a-c), the distribution of cells (a) and 15 nm gold beads (b, c), and an example of a single cell suitable for cryo-ET. The chromatography-purified equine apoferritin sample shows the quality of vitreous ice at low (d) and mediate (e) magnifications and the particle distribution (f). (c) and (e) were imaged with a defocus of -6 and -2 μm, respectively.

We next demonstrated that the PMCP was suitable for preparing samples for SPA. For this, we used a sample that is well known in the single particle community, apoferritin. Many adjacent squares on the grid have an ideal area of vitreous ice within the square. Here, the edge of a square's corners appear round, and the edges of the hole on the supporting film are clearly visible (Fig. 3d). A zoom-in within a square shows that the ice thinning within the hole is homogenous, which shows as a concentric gradient in the background intensity from the edge to the center in all holes in the view (Fig. 3e). The thin region in the center of the hole provides a sufficiently large field of view for high magnification imaging of the particles, which appear evenly distributed without excessive contaminants (Fig. 3f). The thin ice also provides good contrast while preserving the sample, providing the necessary balance that is critical for successful SPA projects.

Discussion

Building on the published work, we have optimized the design of a previously reported manual plunger, and we demonstrated that it can prepare samples suitable for both cryo-ET and SPA. With our device, we successfully vitrified samples of *V. cholerae* and apoferritin. Detailed designs are freely available to the academic community, with the hopes of enabling, in cryo-EM laboratories, the flexibility to prepare samples anywhere, or, for non-cryo-EM laboratories, to incorporate this technique into their experimental toolbox at a low cost. We see this as an important step in the larger community goal of democratizing cryo-EM(41, 49).

During the course of the design, we encountered several challenges. First, we found that the ethane level in the cryogen container directly impacted the amount of residual ethane on the grid after freezing. Though this was not a significant issue because it can be evaporated off or physically removed before imaging, some ethane contamination can sometimes be seen on the grids. Our initial path to resolving this issue was to allow the ethane to evaporate by holding the grid just above the liquid nitrogen layer for several seconds (duration depended on the thickness of ethane) before transferring to a grid box for storage. Alternatively, a piece of filter paper was cooled and suspended just above the liquid nitrogen level allowing the excess ethane to be wicked away by carefully side blotting after plunging. This issue became most prevalent following the melting of the frozen ethane using ethane gas, which subsequently increases the total volume of ethane, and causes the tweezers to also retain some liquid ethane. Being very near the freezing point of ethane, which is ideal for sample preservation, also makes the ethane more viscous. This led us to change our method of thawing the frozen

ethane. Instead of introducing additional gaseous ethane during the freezing session, we used a thick metal object such as the back end of a clean tweezer or scalpel handle to melt the ethane. Either technique allows liquid ethane in the cryogen holder to maintain a suitable temperature range for generating vitreous samples but reduces excess ethane being retained by the tweezers or spilling over into the cryogen container. One additional option to avoid issues with contaminating ethane is the use of an ethane/propane mix instead of pure ethane, as the mix remains liquid at liquid nitrogen temperatures(4).

A known challenge inherent to manual plunging is how to precisely and reproducibly control how much sample is wicked off from the grid. Thus, we provide a video demonstrating the process as a supplement (Supplementary Movie 2). Typically, this experience depends on an accumulated practice on a trial-and-error base. To assist the development of some visual assessment of the blotting process, we placed a light source positioned directly behind the grid. The additional lighting allowed for better monitoring of the wicking and easier determination when blotting was optimal. Additionally, a careful retraction of the blotting paper prevents the breaking of the carbon layer on the grid. For the entire blotting procedure, practice was the best method for obtaining suitable, reproducible samples.

Another issue that could present itself is identifying a local site for glow discharging the support grid. This is critical because carbon-coated grids are hydrophobic and thus when an aqueous sample is applied, the liquid will not distribute evenly across the grid. Glow discharging allows one to create a negatively charged surface that is more suitable for aqueous samples. In our hands, using the grid type and glow discharge protocol noted in the methods, we have had a sufficient number of squares with suitable ice thickness from grids that were several days post discharge. Thus, if it is not possible to glow discharge grids on site, then doing so prior to departure, may be a successful alternative. Here, the accumulated experience for judging when optimal wicking has occurred makes adjusting for slightly different hydrophilicities straightforward.

Lastly, our initial goal was to build a device that could be easily transported and conform to airline restrictions for cabin luggage. While the device itself is quite portable, the case that was made for the final design turned out to be slightly bigger than the standard overhead compartment in an airplane. This challenge could be overcome by a significant reduction in the diameter of the instrument and carrying case, but this may come at a cost of its performance, its stability, and unhindered working space. This should be a goal for future iterations. In addition, certain items

are restricted from carry-on luggage, such as the sharp tweezers, scissors, and any of the required gases, which would prevent the device being placed in the overhead bin.

In this communication, we share the designs for an economical, portable manual cryogenic plunger device that allows for the proper freezing of samples for cryo-ET and SPA. In addition to being able to prepare multiple sample types, this device is quite portable enabling the preparation of samples at sites generally not equipped specifically for cryo-EM. Our hope is that this device will expand this technique well beyond the local experts and contribute to the basic understanding of the microscopic biological world.

Supplementary Material

Supplemental Table 1

Materials*	
bearings	€ 60,00
shock absorption	€ 15,00
polycarbonate dish	€ 200,00
foam dewar	€ 104,00
anodize	€ 110,00
aluminum material	€ 250,00
springs	€ 40,00
various materials	€ 150,00
ground bar	€ 20,00
tweezers (x2)	€ 108,00
storage boxes (x2)	€ 12,00
traveling/storage case	€ 190,00
Materials total	€ 1.259,00
Manufacture and assembly**	€ 2.640,00
Estimated total cost	€ 3.899,00

*excludes VAT and shipping

**Costs will vary by location

Overview of costs for the production of the manual plunger at Leiden University. Cost estimates will vary.

Supplementary Movie 1: Overview of the typical plunge freezing workflow.

Supplementary Movie 2: Demonstration of blotting process under dry conditions.

The detailed designs and movies can be found at <http://briegel-lab.org/manual-plunger-files/>

CHAPTER 4

Transition of *Vibrio cholerae* through a natural host induces resistance to environmental changes

Jamie S. Depelteau¹, Ronald Limpens², Dhruvajyoti Nag³, Bjorn Koch⁴, Jeff Withey³, Annemarie H. Meijer⁴, Ariane Briegel¹

¹ Department of Microbial Sciences, Institute of Biology Leiden, Leiden University, Sylviusweg 72, 2333 BE Leiden, The Netherlands

² Department of Cell & Chemical Biology, Leiden University Medical Center, Leiden, The Netherlands

³ Department of Biochemistry, Microbiology and Immunology, Wayne State University, Detroit, Michigan, United States

⁴ Department of Animal Sciences, Institute of Biology Leiden, Leiden University, Leiden, The Netherlands

Abstract

The pandemic-related strains of *Vibrio cholerae* are known to cause severe diarrheal disease in humans and other animal hosts. These pathogenic bacteria must overcome rapid changes in their environment, such as the transition from fresh water to the gastrointestinal system of their host, and then back into the environment. How *V. cholerae* successfully makes this transition is not well understood. To study the morphological adjustments during environmental transitions, we used zebrafish larvae as a natural host model. Using a combination of fluorescent light microscopy, cryo-electron tomography and serial block face scanning electron microscopy, we studied the structural changes that occur during the infection cycle. We show that the transition from an artificial nutrient-rich environment to a nutrient-poor environment has a dramatic impact on the shape of the bacterial cells, most notably a dehiscence of the inner and outer membrane. In contrast, bacteria that are excreted after passage through the gastrointestinal tract of the zebrafish host retain a uniform distance between the membranes as well as their vibrioid shape. Inside the intestine, *V. cholerae* cells predominantly localized in the regions anterior to the mid-gut. The bacteria were observed as micro-colonies associated with the microvilli as well as within the lumen. The cells retained their vibrioid shape, but changed their cell-length depending on their localization within the gut. Taken together, our results demonstrate dynamic changes in morphological characteristics of *V. cholerae* cells during their transition between the different environments encountered during the infection cycle, and we propose that these structural changes are critical for the pathogen's ability to colonize host tissues.

Introduction

Vibrio cholerae is a motile, gram-negative bacterium common to fresh and brackish water environments. The pandemic-related strains of *V. cholerae* are known to cause disease in a multitude of animals including humans, fish, and birds (50–52). Upon ingestion by humans, *V. cholerae* colonizes the small intestine utilizing molecular machines such as chemotaxis arrays, flagella, and pili to locate and establish its niche (53–56). Within hours of colonization, *V. cholerae* expresses the cholera toxin which causes severe diarrhea in the host. In turn, this releases large quantities of the pathogen back into the environment (57, 58). In humans, *V. cholerae* infection causes over a million Cholera cases and 100,000 deaths annually. Therefore, cholera remains a public health threat especially in areas of war, natural disasters, and/or poor sanitation (50).

The journey from its natural habitat, into and through the digestive system, and back into the environment involves extreme changes of the physical and chemical environment. For example, freshwater is considered a sparse environment that contains limited concentrations of salts, minerals, and nutrients (59). When ingested, *V. cholerae* must adapt to a sudden change in osmolarity and drop in pH due to the acidity of the stomach (57). Subsequently, when entering the gut, the bacteria are exposed to bile salts, antimicrobial peptides, and changes in viscosity, all of which are a means of protection against invaders (60–62). While these barriers result in the death of some ingested bacteria, *V. cholerae* can adapt and continue its infection cycle by colonizing the intestine, and ultimately re-enter the external environment. How are *V. cholerae* cells able to thrive during these drastic changes in environmental conditions of the infection process? Previous studies have shown that the cells alter their shape in response to changing environments (63–65). In addition to its shape, *V. cholerae* may also adapt its molecular machines, altering their availability and quantity, to levels that support success in the new environment. For example, the toxin co-regulated pili are generally upregulated as the bacterium approaches the intestinal epithelial cell surface, which aids in attachment and colonization (54, 58). However, we currently have limited insight into the detailed morphological changes during the infection cycle of *V. cholerae* inside a host organism.

Here we use cryogenic electron tomography (cryo-ET) and serial block face scanning electron microscopy (SBF SEM) to study the structural adaptations of *V. cholerae* as it transitions through its infection cycle of a natural host, the zebrafish (*Danio rerio*). We chose this model for several reasons: the larvae of the zebrafish

are easily accessible for bacterial colonization experiments and microscopy, the physiology of the fish is well understood, and *V. cholerae* has been shown to colonize both adult and larval zebrafish in a manner consistent with human infection and resulting in a diarrheal disease (66, 67).

Using cryo-ET, we first characterized the 3D architecture of cells grown under nutrient-rich conditions in the laboratory environment and under the nutrient-poor conditions after transition to the freshwater environment of the zebrafish larvae. Next, we compared the architecture of these cells with that of cells that had been excreted back into the environment by the *V. cholerae*-infected zebrafish host. Finally, we used SBF SEM imaging to characterize the localization and cell shape inside the host organism.

Together, our results demonstrate that *V. cholerae* dramatically changes both its shape and the composition of molecular machines in response to this switch of nutrient-rich and nutrient-poor environmental conditions. In contrast, *V. cholerae* within the zebrafish larval intestine, as well as cells excreted from adult and larval zebrafish, maintain their typical comma-like shape during both colonization and excretion back into the environment. These results indicate that the journey through the digestive system of the zebrafish induces physiological and structural changes that protect the bacteria from severe changes in environment, and thus, supports its ability to infect the next host.

Methods and materials

Strains

Vibrio cholerae El Tor strains A1552, A1552-GFP, and C6706-tdtomato were used throughout this study. A1552 and A1552-GFP are rifampicin resistant (100 µg/ml) strains that were provided by Prof. dr. Melanie Blokesch (École Polytechnique Fédérale de Lausanne, Switzerland). C6706-tdtomato (referred to as VcRed in68) is streptomycin resistant (100 µg/ml) and was provided by Prof. dr. Matt Waldor (Harvard University, Boston, MA, USA). Note that this strain carries a mutation in the *luxO* gene rendering the strain quorum deficient. Each strain was stocked in 25% glycerol or 10% DMSO and stored at -80°C until use.

Animal welfare

All experiments conducted at Leiden University using the ABTL strain were conducted with the approval of the local animal welfare committee (License # 10612) and in accordance with the EU Animal Protective Directive 2010/63/EU. All

experiments using the wildtype ZDR strain were conducted at Wayne State University with the approval of the local IACUC.

Adult fish were maintained according to established protocols published at zfin.org. To generate larvae, on the night before mating, adult fish were separated by sex into small mating tanks containing a removable barrier between the sexes (one female to two males). The following morning, the separation was removed, and the fish were transferred to a medium sized tank containing a mesh-barrier that allows eggs to drop to the bottom of the tank without interference from the adults. Adults were mated in groups of six males to three females per tank for one hour, and then returned to their original housing. Fertilized eggs were collected by pouring the egg-containing system water through a small strainer, washed with system water to remove any debris, and stored in a petri dish until further processing. Eggs generated from the ZDR strain were incubated at 28°C and washed daily until use. ABTL generated eggs were further processed to render them germ-free using the protocol as previously described (69).

Generation of germ-free zebrafish larvae

To generate germ-free larvae, freshly laid eggs were collected and immediately transferred in batches of 150-200 eggs to 15 ml tube containing sterile artificial fresh water (sAFW; 60 mg/L Instant Ocean; Spectrum Brands, Blacksburg, VA, USA). The sAFW was exchanged for sAFW containing amphotericin B (250 ng/ml), kanamycin (5 µg/ml), and ampicillin (100 µg/ml) and incubated for 4-5 h at 28°C. Next, the antibiotic-sAFW was exchanged for sAFW containing 0.1% PVP-I, the eggs were incubated for approximately 45 s, and immediately washed three times with sAFW. The sAFW was exchanged with a 0.003% bleach solution and incubated for 5 m, then rinsed three times in sAFW. This step was repeated a second time, and in the final wash step the sterile eggs were transferred to a sterile petri dish, unhealthy eggs were removed, and the remaining eggs were stored at 28°C until use. Each day, 100 µl of the AFW was plated onto non-selective LB medium to confirm sterility, and then the AFW was exchanged for fresh sAFW.

Infection model

Larvae colonization: Two days before colonization of the larvae, the strain of interest was streaked on selective LB media and incubated overnight at 30°C. The following day, several colonies were collected with a loop and transferred to liquid LB and grown overnight at 30°C with shaking at 180 rpm. On the morning of infection, the OD of the overnight culture was measured and the volume needed for 1e⁸ bacteria per ml was determined, centrifuged at 5000 x g for 5 m, and the resulting pellet was dissolved in 1 ml of sAFW. Simultaneously, the 3-day post

fertilization (dpf) zebrafish larvae were separated into batches of 25 larvae in 24 ml of sAFW per petri dish. Subsequently, the 1 ml of bacterial culture was added directly to the liquid. For uninfected larvae, 25 ml of sAFW was added directly to the petri dish. The bacteria were incubated with the larvae for 24 h at 28°C, at which point the 4 dpf larvae were washed three times in sAFW to remove excess bacteria, and then incubated an additional 24 h before processing. For the germ-free ABTL experiments, infection occurred at 3 dpf, washing away of excess bacteria at 4 dpf (1 day post infection (dpi)), and imaging or fixation at 5 dpf (2 dpi). For the conventionally reared ZDF larvae experiments, the same protocol was used, but infection occurred at 5 dpf and processing was done at 7 dpf (2 dpi).

Adult: Adult, conventionally reared ZDR wildtype zebrafish were transferred to a 500 ml beaker filled with system water and fasted for 12 h before infection. On the day of infection, the water was exchanged for sterile system water and subsequently inoculated with *V. cholerae*. As with the larvae, bacteria were first streaked on a selective LB plate, followed by the growing of an overnight culture. An adequate volume of overnight culture to generate a final concentration of 2.7×10^7 bacteria/ml was centrifuged as above, the pellet resuspended in sterile system water, and then added directly to the beaker. After 24 h of infection, the fish were washed in sterile system water two times, fresh sterile system water was added, and then left for another 24 h. The adult fish were sacrificed for other experiments. The supernatant was collected, centrifuged at 8000 x g for 10 m, and most of the supernatant was carefully removed. The remaining supernatant was used to wash the sides of the tube and redissolve the pellet, and then transferred to an 1.5 ml tube. 1.5 µl of anti-*V. cholerae* antibody was added, incubated for 5 m, and then centrifuged again for 10 m at 8000 x g. The supernatant was carefully removed, the pellet was dissolved sterile system water and 5 nm gold beads were added, and the sample immediately used for plunge freezing.

Fluorescence imaging

Fluorescence imaging occurred using a Leica TCS SPE inverted confocal scanning microscope (Leica Microsystems, Wetzlar, Germany). 5 dpf zebrafish larvae were first anesthetized in 0.2 mg/ml tricaine, and subsequently mounted laterally in a drop of 1.3% low melting agarose on a Willco-dish glass bottom microscopy dish (Willco Wells B.V., Amsterdam, The Netherlands). Once the agarose solidified, the fish were surrounded by 0.2 mg/ml tricaine and then imaged using the 40x long working distance water immersion lens. Z-stacks were acquired using the Leiden Application Suite X (LAS X).

Sample collection and preparation

Samples involving bacteria incubated in LB and AFW were prepared as follows. Bacteria were prepared as described for the infection model. $1e^8$ bacteria per ml were isolated from an overnight culture, pelleted, and redissolved in 1 ml of sAFW. Subsequently, this was added to a sterile petri containing 24 ml of sAFW with or without zebrafish larvae and incubated at 28°C. 2 ml of the diluted bacteria was collected at 1 dpi and 2 dpi, centrifuged for 5 m at 5000 x g, and the resulting pellet was dissolved in 27 μ l sAFW and 3 μ l 10 nm gold beads (Cell Microscopy Core, Utrecht University, Utrecht, The Netherlands). For each time point, grids were prepared using a Leica EM GP (Leica Microsystems, Wetzlar, Germany) by adding 3 μ l of the sample directly to a glow discharged Quantifoil R2/2, 200 mesh Cu grid (Quantifoil Micro Tools GmbH, Jena, Germany), incubated for 30 s, blotted for 1 s and immediately plunged into a liquid ethane cooled to -184°C. Grids were transferred to grid boxes and stored in liquid nitrogen until imaging.

Samples associated with the ZDF zebrafish and larvae were prepared using a portable manual plunger (70). In brief, 3 μ l of sample was added to a glow discharged Quantifoil R2/2, 200 mesh grid, incubated for 30 s, and manually plunged into a liquid ethane/propane mixture cooled by liquid nitrogen (4). For experiments using germ-full larvae and adults, the anti-*Vibrio cholerae* polyclonal antibody (KPL Bactrace, ELITechGroup, Spankeren, Netherlands) was added to the excreted bacteria sample as a way to identify *V. cholerae* cells during target selection for cryo-ET. The addition of the 5nm beads during the sample preparation process acted as a secondary that was easily visualized in the electron microscope.

Cryo-EM

All cryo-EM samples were screened using a Thermo Fisher Scientific (TFS; Waltham, MA, USA) Talos L120C equipped with a Ceta CMOS camera and extended cooling. Samples were inserted using a Gatan 626 side entry holder (Gatan Inc, Pleasanton, CA, USA).

Cryogenic electron tomography data was collected using a TFS Titan Krios microscope equipped with either a Gatan K2 BioQuantum or the Gatan K3 BioQuantum direct electron detection camera, both equipped with a post-column energy filter operating with a slit width of 20eV. The data collected from cells in AFW was collected using UCSF Tomography using a bidirectional tilt scheme of -54° to 54° with 2° increments, the K2 camera with a pixel size of 5.44 Å, a defocus of -6 μ m and total dose of 100 e⁻/Å² (71) The data collected from excreted cells was collected using SerialEM with a bidirectional tilt scheme of -54° to 54° with 2°

increments, the K3 camera with a pixel size of 4.41 Å, a defocus of -8 µm, and total dose of 140 e⁻/Å² (72).

Serial Block Face Scanning Electron Microscopy

After fixing the material for 2 h at room temperature with 2.5% GA + 2% PFA in 0.15 M Cacodylate buffer containing 2 mM CaCl₂, the material was washed 3 times with buffer and then placed into 2% OsO₄ / 1.5% potassium ferrocyanide in 0.15 M Cacodylate buffer containing 2 mM CaCl₂. The material was left for 60 m on ice. After washing 3 times in milliQ water, the material was placed into 1% thiocarbohydrazide for 20 m at room temperature. The material was again washed and then stained with 2% aqueous OsO₄ for 30 m at room temperature. After washing 3 times, the material was placed into 1% Uranyl acetate for 2 h at room temperature. The material was washed with milliQ water then stained with lead aspartate for 30 m at 60°C. The material was again washed with milliQ water and then dehydrated on ice in 20%, 50% and 70% ethanol solutions for 5 m at each step. After replacing the 70% ethanol with a fresh 70% ethanol solution, the samples were kept overnight at 4°C. The next day, samples were dehydrated in 90%, 100%, 100% ethanol solutions for 5 m at each step. Next, the material was kept in dry acetone for 10 m on ice, and another 10 m in fresh dry acetone at room temperature. The material was infiltrated with 25%, 50% and 75% Durcupan ACM solution in acetone for 2 h at room temperature for each step, followed by an overnight step at room temperature in 100% Durcupan resin. The next day, the material was placed in fresh Durcupan resin for 2 h at room temperature, after which the material was flat embedded and polymerized at 60°C for 48 h.

Data was collected with a 3View2XP (Gatan Inc, Pleasanton, CA, USA) unit installed on a Zeiss Gemini 300 field emission SEM (Carl Zeiss Microscopy GmbH, Jena, Germany). The volumes were collected at 1.8kV accelerating voltage and variable pressure at 5 Pascal. The pixel dwell time was 2 microseconds, with a pixel size of 10 nm and a section thickness of 75 nm.

Imaging processing and statistical analysis

Imaging data collected from the cryo-electron microscope was processed using the IMOD image processing suite (73). Initially, frames were aligned using the alignframes feature, and the resulting tilt series were batch processed using batchruntomo (74). The initial tomograms were reviewed for quality, and select tomograms were then further processed to improve the bead model and positioning, and finally reprocessed with a SIRT-like filtered back projection to improve the contrast.

Segmentation and cell length measurements were obtained using the 3dmod component of the IMOD image processing suite (73). Length measurements were normally distributed, variance was compared and then significance was determined using a pool-variance two sample T-test (Statistics Kingdom, 2021).

Results

Environmental *V. cholerae*

For this study, we first characterized *V. cholerae* cells grown in LB media, which is a widely-used nutrient-rich growth condition. *V. cholerae* cells grown overnight in LB exhibit a typical vibroid shape and express the structures associated with bacterial cells in a nutrient-rich environment: chemotaxis arrays, flagella and its motor, uniform spacing between the inner and outer membrane, pili, ribosomes, and storage granules (Fig. 1A). We analyzed the number of cells containing structures related to infection, namely flagella, pili, and the F6 chemotaxis array, as these structures have specific roles in identifying favorable environments and attaching to surfaces. Flagella and F6 chemotaxis arrays were detected in over 80% of bacterial cells and pili in more than 50% (Fig.1B).

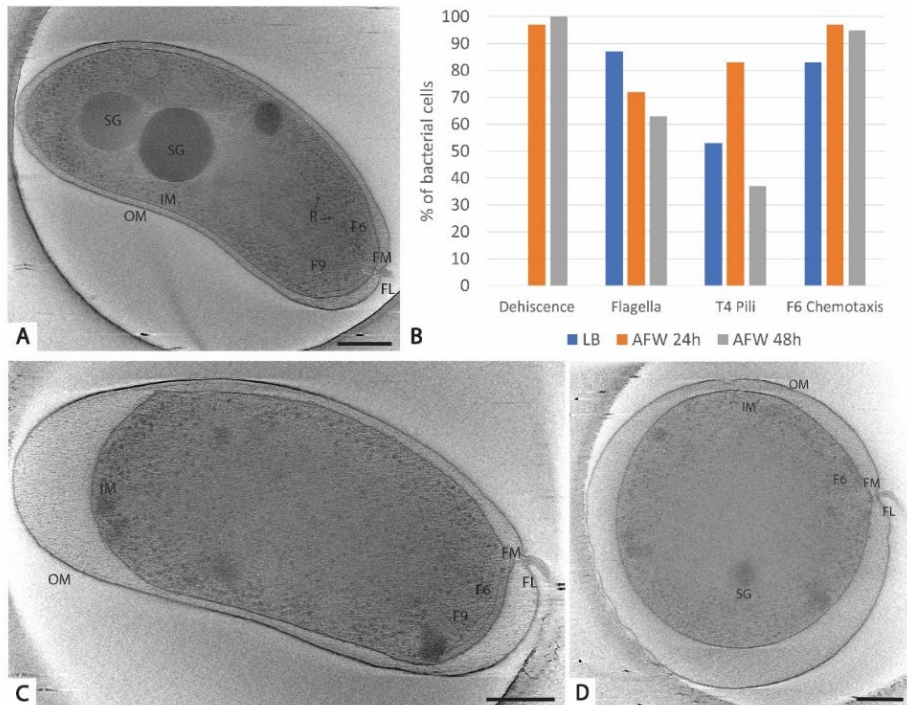


Figure 1. Ultrastructural analysis of *V. cholerae* transition from LB to artificial fresh water. *V. cholerae* A1552 in LB retain their characteristic comma shape and features (A). Quantification of the presence or absence of the dehiscence phenotype and the molecular machines known to be important in infection are detailed in B. After 24 h in AFW, the shape drastically changes, especially between the inner and outer membrane (C), and this dehiscence phenotype continues after 48 h in AFW (D). OM, outer membrane; IM, inner membrane; SG, storage granule; F6, membrane-imbedded chemotaxis array; FM, flagellar motor; FL, flagella; R, ribosome; F9, cytoplasmic chemotaxis array. Scale bar = 250 nm.

We next transitioned the *V. cholerae* grown in LB to artificial fresh water (AFW) and characterized the morphological changes over the course of 48 h. Previous studies have shown that colonization with an El Tor strain peaks at 48 hpi, and thus provided an end point for observation (66). After 24 h of exposure to AFW, the overall morphology of the cells changed drastically (Fig. 1C). While many cells still exhibited an overall vibroid shape, the distance between the inner (IM) and outer (OM) membrane is strongly increased (referred to as dehiscence). Apparently, the inner membrane is constricting while the outer membranes remain the original size. This results in a loose appearance of the OM around the cell and an enlarged periplasmic space. The structures important to the infection cycle, such as the F6 chemotaxis array, the flagella, and the pili were still present in most cells. At 48 h, the morphology changed and dehiscence became the most extreme, while the infection related structures could still be observed in many cells (Fig. 1B).

A detailed comparison of the numbers of infection-related structures between the cells grown in LB (n=15), 24 h in AFW (n=29), 48 h in AFW (n=19) shows a decreasing trend in the presence of the flagella over time (87% vs 72% vs 63%), an increasing trend followed by a decrease of the presence of pili (53% vs 83% vs 37%), and a slight increasing trend in the cells with an F6 chemotaxis array (83% vs 97% vs 95%; Fig. 1B). Finally, it was also notable to find unknown structures within the cells in AFW for 24 h or 48 h (Fig. S1).

Colonization of the zebrafish larvae intestine

As described in previous research, zebrafish and their larvae are susceptible to *V. cholerae* colonization and the subsequent effects (66). However, the two fluorescently labelled strains used in this study have a genetic difference that may impact colonization: C6706-tdTomato is deficient in quorum sensing whereas A1552-GFP is quorum proficient. Fluorescence imaging of 5 dpf larvae infected of C6706-tdTomato showed a similar infection pattern as described in Runft et al (which used a quorum proficient strain), and was analogous to the colonization patterns demonstrated in the mouse model using the same strain (66, 68). In addition, we see significant GFP autofluorescence within the zebrafish larvae which imposed additional challenges for imaging. Thus, we chose to infect germ-free zebrafish larvae with *V. cholerae* strain C6706-tdTomato to explore the ultrastructural features using serial block face SEM. Similar to the mouse model, colonies were primarily found in the in the gastric ventricle, anterior intestine, and anterior portion of the mid intestine (Fig. 2B, 68) at the junction of several villi, or at or near the base of a single villi. In addition, planktonic cells could be seen swimming within the lumen of gastric ventricle, implying the environment was conducive to colonization (Fig. 2B). This phenotype continued until the mid-gut, which begins approximately just past the swim bladder. At the exit of the intestinal system, the cloaca, large pulses of bacteria could be seen being excreted back into the local environment (Fig. 2C).

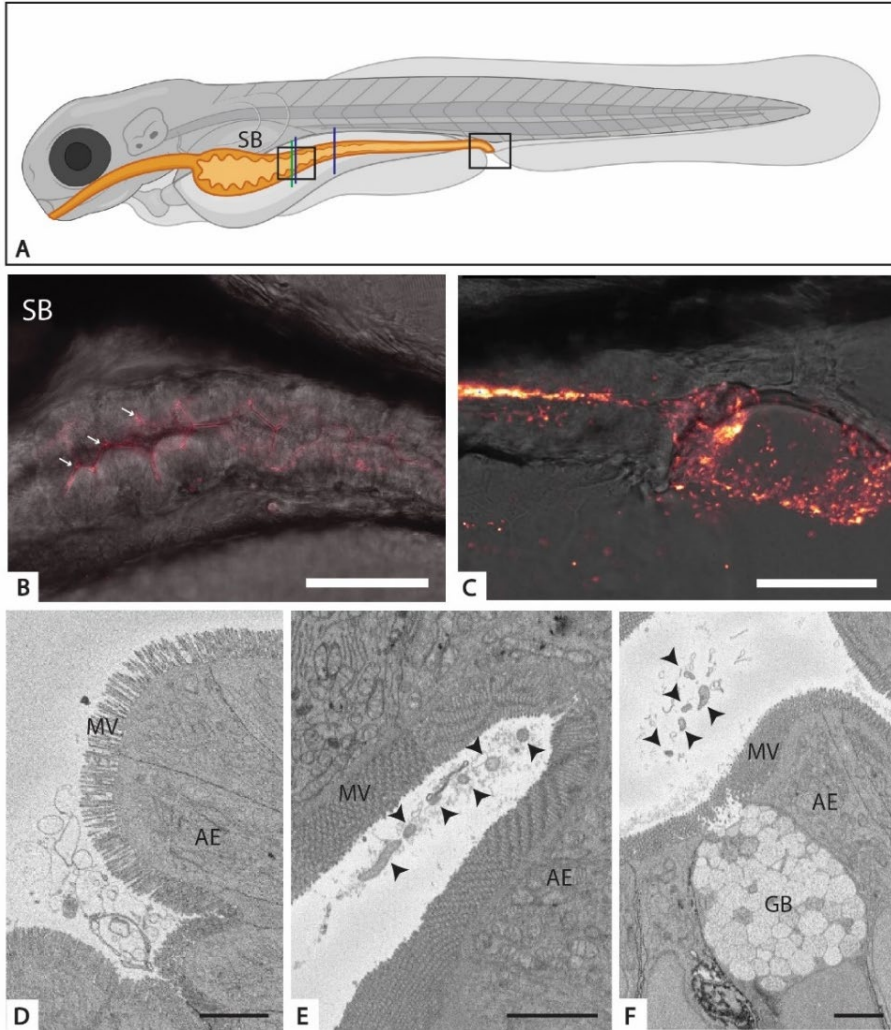


Figure 2. Colonization of the 5 dpf zebrafish larvae with *V. cholerae* C6706-tdTomato characterized by fluorescence and serial block face scanning electron microscopy. A. A schematic of the zebrafish larvae highlighting the gastrointestinal system (orange) and the areas of interest. B. & C. Fluorescent imaging of the anterior intestine (B, left square in A) and posterior intestine and cloaca (C, right square in A). The white arrows in B indicate areas of colonization. D-F. Representative sections of the germ-free (D, green line in A) and C6706-tdTomato infected zebrafish larvae at the anterior (E, left blue line in A) and mid-intestine (F, right blue line in A). *V. cholerae* cells are indicated with black arrows. SB, swim bladder; AE, absorptive enterocytes; MV, microvilli; GB, goblet cells. Panel A was created with Biorender.com. Scale bar = 75 μ m (B); 50 μ m (C); 3 μ m (D-F).

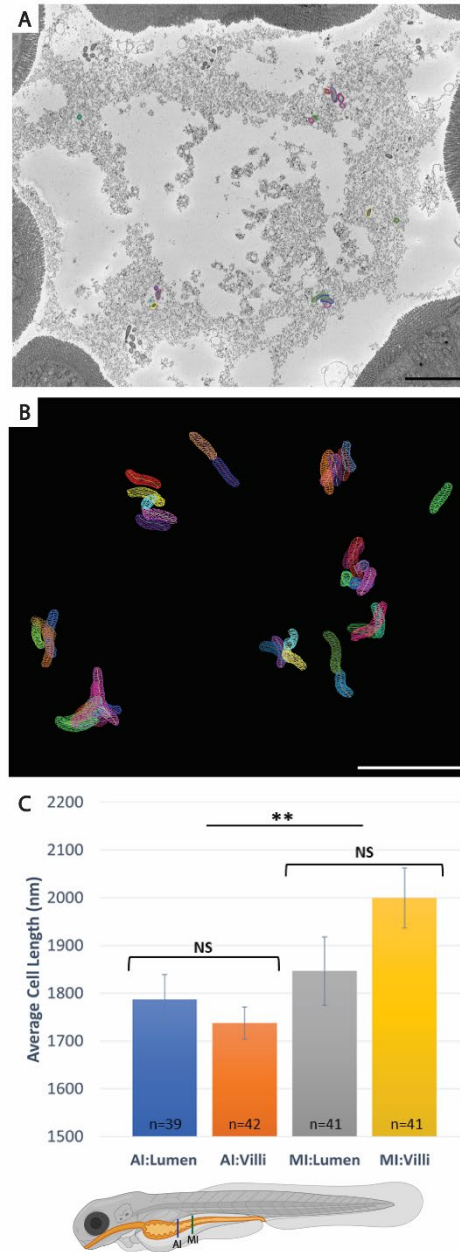


Figure 3. Quantification of *V. cholerae* cell length at different locations in the zebrafish gut. A & B. Representative SBF SEM micrograph (A) from the lumen denoting the location of bacteria and highlighting the ones that had been segmented in that section (B). C. A graph showing the average length of the segmented cells and associated standard error. Groups include anterior intestine lumen and villi (AI:Lumen and AI:Villi, blue line) and mid-intestine lumen and villi (MI-Lumen and MI-Villi, green line). A comparison of total cell length for AI and MI revealed a significant difference. Zebrafish schematic in C was created in Biorender.com. Scale bars = 5 μ m. ** $p < 0.01$.

Based on this information, we prepared *V. cholerae* C6706-tdTomato infected and uninfected 5 dpf zebrafish larvae for SBF SEM. Using this method, we are able to achieve large volumes of three-dimensional data of areas of interest (in our case covering up to 150 μm length of the intestine). An overview of the germ-free, uninfected zebrafish larvae confirmed the absence of a microbiota, the presence of material in the lumen, and an underdeveloped brush border, as shown by the loose packing of the microvilli (Fig. 2D). In contrast, the microvilli of the *V. cholerae*-infected larvae are tightly packed, and microcolonies are present throughout the lumen including the base of villi and unassociated within the lumen (Fig. 2E, arrowheads). Similar to the mouse model, colonization of the intestine wanes as it approaches the mid-intestine and posterior intestine, areas where the majority of the mucus producing goblet cells reside (Fig. 2F; 68).

These volumes allowed the analysis of the overall morphology of the bacterial cells that colonized the intestine. Using segmentation software, we were able to outline the bacteria in different parts of the intestine, and subsequently determine the length of the cells (Fig. 3A). Overall, all cells exhibited a vibroid shape (Fig. 3B). We then determined the length of cells in the villi of the anterior intestine just below the posterior portion of the swim bladder, and the anterior portion of the mid-intestine. A comparison of cell length within each area showed no significant difference in cell length (Fig. 3C). However, a comparison between the two locations showed a significant difference in cell length ($p=0.006$; AI-total 1763.05 nm vs MI total 1924.10 nm): Bacterial cells in the anterior intestine were significantly shorter compared to the cells in the mid-gut.

Excreted *V. cholerae*

Finally, we examined the bacteria that are excreted from infected adult and larval zebrafish. Overall, we observed cells in all conditions that had a vibroid or oval shape (Fig. 4). None of the groups had a noticeable separation of the inner and outer membrane by 24 h ($n=35$, 31% from the larvae, $n=24$; 13% from the adults, compared to nearly 100% of cells in AFW for 24 h or 48 h). For the bacteria that were directly excreted by the adult fish, we observed a similar number of pili (75%) and the F6 chemotaxis arrays (94%) compared to the LB and AFW samples. However, there was a noticeable decrease in the presence of the flagella (10% of cells). The bacteria excreted from the larvae resembled the AFW sample in terms of the presence of the pili (77%) and the F6 chemotaxis arrays (97%), but a noticeable decrease in the presence of the flagella (40% of cells). The presence of storage granules was also noted in the majority of the excreted cells (adult, 88% & larvae, 80% vs. just 31% in the control).

As a control, we exposed bacteria from the same culture that was used to infect the zebrafish to sterile system water without the presence of fish for 24 h. In this case, we wanted to see what would happen to the bacteria when they were not passaged through the fish but exposed to a similar environment. After 24 h, these cells exhibited dehiscence in about 43% of the population, and the presence of flagella was similar to the adult excreted bacterium (45%; n=49)). A number of cells had a reduction in the number of pili (37%) while the F6 chemotaxis array was present in 100% of the cells (Fig. 4). Taken together, these cells do not show as extreme as an affect as seen in cells transition to AFW for 24 h, but seem to be more similar to the cells excreted by the larvae with the exception of the presence of pili.

Finally, as it was noted for the *V. cholerae* isolated from AFW, we also occasionally found unknown structures in the cells excreted from the zebrafish (Fig. S1).

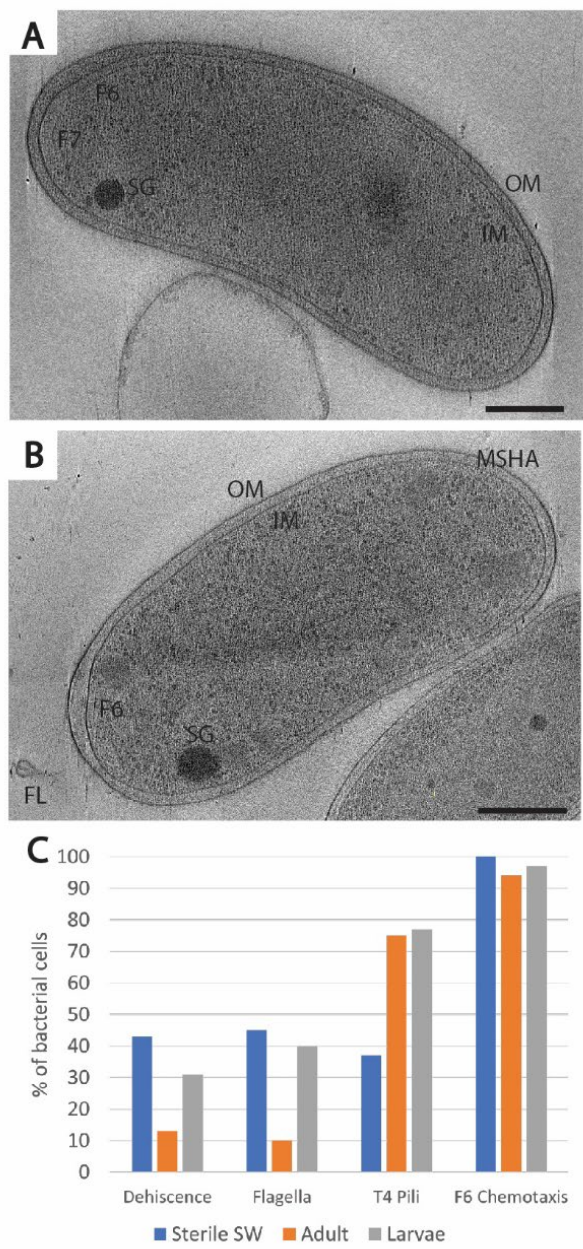


Figure 4. Morphology and machine changes of *V. cholerae* excreted from zebrafish (adult or larvae). Individual micrographs of a cell excreted from the adult zebrafish (A) or larvae (B). C. Quantification of structures important to the infection cycle. OM, outer membrane; IM, inner membrane; SG, storage granule; F6, membrane-imbedded chemotaxis array; FL, flagella. Scale bar = 250 nm.

Discussion

The infection cycle of *Vibrio cholerae* involves a complex series of transitions, from fresh or brackish water, into a host's gastrointestinal system, and then back into the environment. This invariably exposes the pathogen to vastly different environmental conditions, including changes in nutrient availability, pH, and salt concentrations. To what extent the *V. cholerae* cells adjust their ultrastructural morphology to survive and thrive throughout this infection cycle is largely unknown. EM provides an excellent opportunity to explore these changes. The molecular machines of *V. cholerae*, such as the chemotaxis arrays, flagellar motor, and type 6 secretion system, are well characterized and easily identifiable using cryo-ET (46, 75–77). However, most of these structural analyses were done in *in vitro* conditions and not associated with a natural host. Here, we studied the morphological characteristics of the pathogen during the infection cycle in the natural host model system of the zebrafish.

Using a variety of microscopy techniques, we demonstrate the impact of the environmental changes on the cell morphology of the pathogen at the nanoscale. Using cryo-ET, we show the drastic morphological changes that occur when *V. cholerae* transitions from a high-nutrient and high-salt environment to a low-salt and low-nutrient environment. Upon introduction to artificial fresh water, the bacterial morphologically changes, most notably by the increasing distance between the inner and the outer membrane. Dehiscence within bacteria, including *V. cholerae*, has previously been described and it has been associated with the transition to viable but non-culturable states, in which cells have a very low metabolic activity (64, 65). As noted in previous research, *V. cholerae* also expresses unknown structures in response to stressful environments (78). In this study, we also observed unknown structures including the previously described 'wavey filament' and several types of other filaments (Suppl. Fig. S1). It is possible that these structures are related to either nutrient storage or DNA compaction, but further study is needed to clarify their identity and role in the adaption to changes in environmental conditions.

We next examined the bacteria that had transitioned through the zebrafish and been excreted back into a low-salt and low-nutrient environment (sterile system water). Interestingly, unlike the bacteria that were transitioned from LB to AFW, cryo-ET showed that the cells altered their morphology to a lesser extent in response to the environmental change, and a majority retained a vibroid or ovoid shape and displayed MSHA pili and F6 chemotaxis arrays at similar levels to LB-cultured cells. In addition, we observed a decrease in the number of flagella present

in the cells excreted from the adult host. This loss of flagella could be the result of flagellar ejection that has been previously observed in response to the transition to a low nutrient environment (79). Together, these results suggest that the transition through the gut of the zebrafish likely primes the bacterium for release into the environment (in our case artificial freshwater or sterilized system water). The majority of the cells retain their cell envelope structure with consistent distance between the IM and the OM. Furthermore, the excreted cells appear to be equipped with the molecular machinery necessary to explore the new environment.

Previous research suggested that *V. cholerae* excreted from the mouse model, as well as cells within or recently dislodged from biofilms, are hyperinfectious, meaning that less cells are needed to continue the infection cycle in another host (80, 81). Our research supports these findings as the excreted cells did not show typical stress responses such as dehiscence. In addition, they contain molecular machinery, such as the chemotaxis array to sense their environment, the flagella to move towards a favorable environment and MSHA pili to attach to a favorable host, which are necessary to effectively transition to another host. Lastly, we also noted that the excreted cells contain storage granules, likely glycogen or polyphosphate, and it was previously shown that these types of storage granules also impart a resistance to the transition from the host back into the environment (82, 83).

Finally, to examine bacteria that had colonized the gut of the zebrafish we focused on the 5 dpf larvae infection model because of its ease of use for imaging and suitability for preparation for serial block face SEM. In our study, we were able to visualize the *V. cholerae* infection of large parts (covering about 150 μm along the length of the larval intestine) at cellular resolution and in three dimensions, which is a substantial improvement in volume compared to previously applied techniques. These data show that the bacteria colonized several parts of the intestine, have the typical vibroid morphology, are actively dividing, and that microcolonies are directly associated with the microvilli or free floating in the lumen. Previous studies suggested that the toxin coregulated pilus (TCP) is involved in this attachment, but the resolution of the SBF SEM is insufficient to confirm or refute this hypothesis at present. In addition, previous research has shown that colonization of the zebrafish model with a ToxT mutant (which lacks TCP and cholera toxin) had no colonization defect compared to the wildtype bacterium, indicating that there are other factors involved in colonization (66). In the future, other methods will be necessary to accurately describe this cell-to-cell interaction and to determine what bacterial appendages play a role in the attachment. Recent developments in large volume

sample preparation for cryo-ET are promising options for future studies, but not yet routinely available (9, 84, 85).

While our study gives new insights into the morphological characteristics of a *V. cholerae* infection, many questions remain about the lifecycle of this pathogen. In our study, we used a recently described model for infection, and we chose to do this in a germ-free environment to ease the identification of the bacterium in the various microscopy methods. However, understanding our findings in the context of a natural environment will be an essential next step to determine how the intestinal microbiota affects *V. cholerae*'s ability to colonize the host. This is especially true for the understanding how the bacteria interact with the intestinal lining. Current methods do not allow for high resolution imaging at the structural level, as was done with the bacteria in AFW or excreted from the fish.

In summary, we describe the *V. cholerae* infection lifecycle at unprecedented detail using the natural host model, the zebrafish. We show that in laboratory conditions, the transition from nutrient-rich to nutrient-poor conditions causes dramatic morphological changes over 48 h, yet those cells retain factors that are known to be important for infection. We then show that *V. cholerae* excreted from the zebrafish do not show the same changes in morphology, demonstrating that the passage of the bacteria through the intestinal track plays an important role in preparing the bacteria for release back into a freshwater-like environment. Finally, SBF SEM provided insight into the cell morphology and microcolony structure within the lumen. Together, our research provides additional details about the transitions between environments and its role in the infection cycle. Further research will need to be done to confirm physiological mechanism that link structure to function, and this research helps to focus those questions for future studies.

Acknowledgements

The authors would like to thank Prof.dr. Melanie Ohi and Louise Chang of the University of Michigan for the use of their glow discharger during sample collection at Wayne State University, and the Netherlands Centre for Electron Nanoscopy and its operators for assistance during data collection.

Funding

This work is funded by a Building Blocks of Life grant 737.016.004 to A.B. and A.H.M. from the Netherlands Organization for Scientific Research. Microscope access was supported by the Netherlands Centre for Electron Nanoscopy and partially funded by Netherlands Electron Microscopy Infrastructure grant 84.034.014.

Supplementary Figure

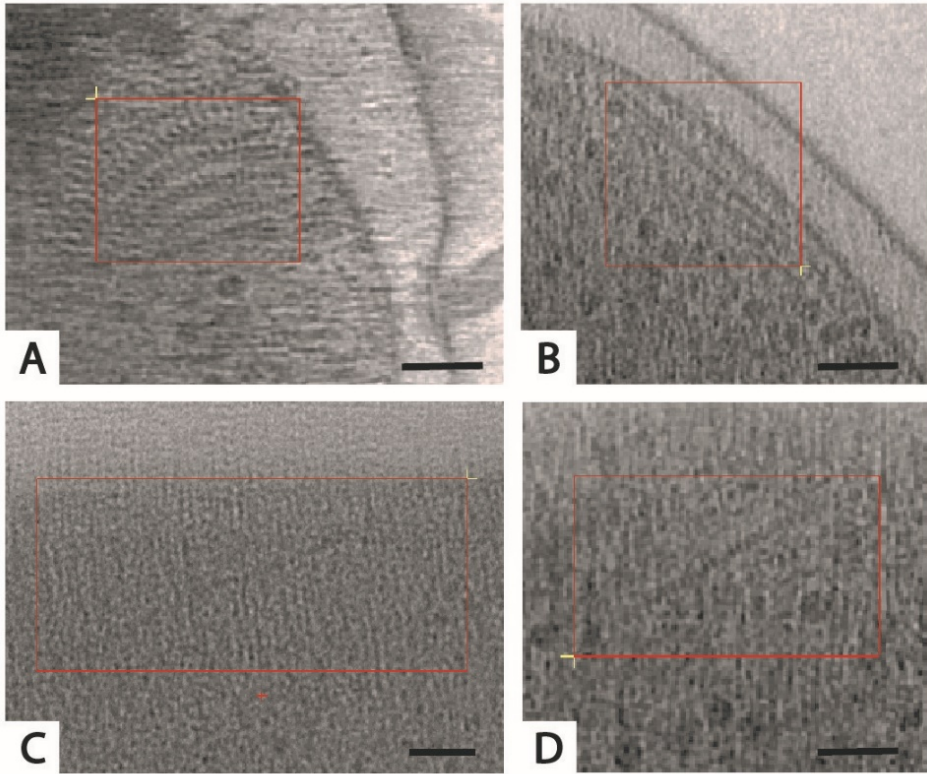


Figure S1. Unknown structures observed in cells in freshwater environments. (A) Wavy filament. (B) Linear filament 1. (C) Periplasmic filament. (D) Linear filament 2. Red boxes identify boundaries of structures. Scalebars 50 nm.

CHAPTER 5

UVC inactivation of pathogenic samples suitable for cryo-EM analysis

Depelteau JS¹, Renault L², Althof N¹, Cassidy CK³, Mendonça LM^{4†}, Jensen GJ⁵, Resch GP⁶, Briegel A^{1,2}

¹ Department of Microbial Sciences, Institute of Biology, Leiden University, Sylviusweg 72, 2333 BE Leiden, The Netherlands

² Netherlands Center for Nanoscopy (NeCEN), Leiden University, The Netherlands

³ Department of Biochemistry, University of Oxford, Oxford, United Kingdom

⁴ Biology and Bioengineering Department, California Institute of Technology, Pasadena, CA, USA

⁵ Biology and Bioengineering Department, California Institute of Technology, Pasadena, CA, USA and Department of Chemistry and Biochemistry, Brigham Young University, Provo, UT USA

⁶ Nexperion e.U. – Solutions for Electron Microscopy, Vienna, Austria

[†]Division of Structural Biology, Wellcome Trust Centre for Human Genetics, University of Oxford, Oxford, United Kingdom

Abstract

Cryo-electron microscopy has become an essential tool to understand structure and function of biological samples, from individual proteins to whole cells. Especially for pathogens, such as disease-causing bacteria and viruses, insights gained by cryo-EM can aid in developing cures. However, due to the biosafety restrictions of human pathogens, samples are often treated by chemical fixation to render the pathogen inert, affecting the delicate ultrastructure of the sample. Alternatively, researchers use *in vitro* or *ex vivo* models, which are non-pathogenic but lack the complexity of the pathogen of interest. Here we show that ultraviolet-C (UVC) radiation at cryogenic temperatures can be used to eliminate or dramatically reduce the infectivity of two model organisms, a pathogenic bacterium (*Vibrio cholerae*) and a virus-like particle (the ICP1 bacteriophage). We show no discernable structural impact of this treatment of either sample using two cryo-EM methods: cryo-electron tomography (cryo-ET) followed by subtomogram averaging (STA), and single particle analysis (SPA). Additionally, we applied the UVC irradiation to the protein apoferritin (ApoF), which is a widely used test sample for high resolution SPA studies. The UVC-treated ApoF sample resulted in a 2.1 Å structure that did not reveal any discernable structural damage. Together, these results show that the UVC irradiation dose that effectively inactivates cryo-EM samples does not negatively impact their structure. This research demonstrates that UVC treatment is an effective and inexpensive addition to the cryo-EM sample preparation toolbox.

Introduction

Cryogenic electron microscopy (cryo-EM) has emerged as a powerful technique for determining the structural characteristics of individual proteins, protein complexes, whole viruses, and even intact cells. The major advantage of this method is that it does not require any of the potentially artifact-inducing preparation steps needed for traditional transmission electron microscopy, such as dehydration, staining, or plastic embedding. Instead, the samples are simply flash-frozen into a glass-like ice (vitrified) and remain in a near-native state. Such samples can then be directly imaged using cryo-EM, providing high resolution structural information which in turn enables scientists to answer a wide range of specific biological questions.

The power of this technique is becoming increasingly apparent. For example, cryo-EM has given important insight into how components of SARS-CoV-2, the coronavirus causing the COVID-19 epidemic, interact with host cells, potential drugs, and candidate vaccines (for examples, see 50–54). However, many of the structure-related studies resulted from either *in vitro* expressed proteins, isolated proteins from inactive virus, or a virus from the same family but lacks pathogenicity for humans. In other words, the information, while important to the understanding of how this virus infects its host and how to treat it, lacks structural information from the actual pathogen in a natural setting.

This is not only a limitation for the virus, but it is also the case for pathogens in general: the sample preparation for cryo-EM by flash-freezing is optimized to minimize structural damage. Therefore, precautions according to the specific biosafety level of any given sample need to be maintained throughout the entire sample preparation and imaging workflow. This limits the applicability of cryo-EM for obtaining structural information from such infectious pathogens, as cryo-EM facilities may not be equipped or approved to work with pathogens of biosafety level 2 or higher, or researchers are limited to specialized centers which host specialized, dedicated equipment such as a Titan Krios within a BSL2 or higher environment. This is a limiting factor for the research community's ability to study these medically important organisms in real-life scenarios.

A recent study by Jin *et al.* demonstrated that ultraviolet (UV) irradiation of cryopreserved mouse embryonic fibroblasts has little-to-no effect on elemental distribution of the frozen hydrated samples (91). With similar ideas, we began testing whether UV irradiation could be applied to pathogens without compromising the ultrastructure of the samples. We tested this by applying ultraviolet-C (UVC) irradiation to inactivate two pathogenic organisms. UVC

irradiation was chosen because of its well-described ability to inactivate pathogens (92, 93). Inactivation occurs by altering the DNA of the organism, leading to the prevention of transcription and replication (12, 94). UVC irradiation is also known to impact proteins, mainly by disulfide bond breakage and the creation of reactive oxygen species (95, 96). A combination of the above effects leads to the loss of viability of the organism, but the detailed effects on the structure of the pathogen are not well documented.

Here we describe a simple, inexpensive proof-of-principle prototype for administering UVC irradiation to cryo-EM samples under cryogenic conditions. We initially tested this device on two model organisms: the pathogenic bacterium *Vibrio cholerae* and the bacteriophage ICP1, a virus-like particle that infects *V. cholerae*. These organisms were chosen to test the applicability of the UVC inactivation for two different cryo-EM methods. The bacterium was used for cryo-electron tomography (cryo-ET) and subtomogram averaging (STA) workflows. These methods are used to study heterogeneous samples like whole bacterial cells and typically results in resolutions limited to macromolecular resolution (2-4 nm, 20-40 Å). Single particle analysis (SPA) was used to evaluate the ICP1 bacteriophage sample, a method which allows the structure determination of identical particles to higher resolution (below 1 nm, 10 Å). Finally, we used SPA of the protein apoferritin (ApoF) to determine structural changes at high (near-atomic) resolution that might result from UVC irradiation. ApoF is a common validation standard used in the EM community and resolutions of better than 3 Å are routinely achieved.

Here we show that UVC irradiation effectively inactivated both the pathogenic bacterium and the bacteriophage. We further show that the effects of this treatment on the structural information are non-discernable in the tested STA and SPA samples. Our study demonstrates that UVC irradiation of vitrified pathogen samples is a promising alternative to chemical fixation or the use of *in vitro* systems when access to a cryo-EM facility with sufficient biosafety clearance is not feasible. Combined with a simplified plunging device, it may be possible to freeze and UVC-treat samples locally, which can then be imaged at a lower safety level without compromising the structural information. In summary, this study provides significant evidence that UVC irradiation of cryo-EM samples may be a viable solution for structural investigations of a broad range of pathogen with cryo-EM.

Methods and materials

Bacteria and bacteriophage strains and conditions

Vibrio cholerae strains A1552 wildtype (WT; rifampicin resistance, 100 µg/ml), N16961 WT (streptomycin resistance, 100 µg/ml), and N16961-TndsRed (gentamycin resistance, 10 µg/ml) were provided by Dr. Melanie Blokesch (Ecole Polytechnique Fédérale de Lausanne, Switzerland). *V. cholerae* were grown overnight in lysogeny broth (LB) containing antibiotic at 30°C with shaking at 180 rpm. Equal volumes of an overnight culture and sterile 50% glycerol or 10% DMSO were mixed, frozen in liquid nitrogen, and stored at -80°C until use.

The ICP1 bacteriophage was provided by Andrew Camilli (Tufts University, Massachusetts, USA). The ICP1 phage was propagated using *V. cholerae* N16961 WT as described previously (97). Briefly, 10⁶ ICP1 phage was added to a 50 ml culture (starting OD₆₀₀ = 0.2) containing 5 µM CaCl₂. The culture was incubated for 4-6 h at 30°C with shaking at 180 rpm and the bacteria was pelleted by centrifugation (5000 g at 4°C for 30 m) and discarded. The supernatant is filtered through a 0.20 µm filter, subsequently ICP1 is precipitated out using 20% PEG8000/2.5 M NaCl solution overnight. Finally, ICP1 is pelleted by centrifugation (3000 g at 4°C for 1h) and dissolved in phage storage buffer (100 mM NaCl, 10 mM MgSO₄, 10 mM Tris-HCl (pH 7.5), 1 mM EDTA) and stored at 4°C until use.

Sample preparation

V. cholerae was streaked onto a selective LB plate and grown overnight at 30°C and stored at room temperature. The night before the freezing session, several colonies were resuspended in liquid LB containing antibiotic and grown overnight at 30°C with shaking at 180 rpm. An aliquot of this culture was used for freezing as described below. For ICP1, an aliquot from the phage stock was used directly for sample freezing. To minimize lipid vesicles in the ICP1 sample, Tween-80 (Sigma Aldrich, St. Louis, MO, USA) was added to the UVC-treated sample shortly before freezing to a final concentration of 0.05%.

The bacterial and phage samples were prepared using a Leica EM GP (Leica Microsystems, Wetzlar, Germany). For the bacterial sample, 15 nm gold beads was added to the bacteria prior to freezing (Cell Microscopy Core, Utrecht University, Utrecht, The Netherlands). For both samples, 3 µl was applied to a glow discharged Quantifoil R2/2, 200 mesh Cu grid (Quantifoil Micro Tools GmbH, Jena, Germany), and incubated prior to blotting (30 s for *V. cholerae* or 10 s for ICP1) at 18°C with approximately 90% relative humidity. The grid was blotted for 1 s and automatically plunged into liquid ethane. Vitrified samples were transferred to storage boxes and

stored in liquid nitrogen until use. All grids were screened using a Talos L120C cryo-electron microscope (Thermo Fisher Scientific (TFS), Waltham, MA, USA) equipped with a 626 side entry holder (Gatan, Inc., Pleasanton, CA, USA) to determine suitability for data collection.

Human apoferritin (ApoF) sample was used at a concentration of 4 mg/mL and applied to glow discharged Quantifoil R2/2, 200 mesh grid before being double-side blotted for 3 s in a Vitrobot Mark IV (TFS) and plunge frozen into liquid ethane. Frozen samples were stored in liquid nitrogen until UVC treatment and imaging.

UV irradiation device and protocol

The UV irradiation device was constructed using easy-to-acquire materials. Working with our local fine mechanical department, we created a sandwich of three quartz glass slides (Fig. S1A). Quartz glass was chosen because it does not interfere with UVC radiation, as shown with spectroscopy. This sandwich design allows for the accurate placement of the frozen grids during the UVC irradiation process (Fig. S1B). A holder for the grid box and quartz slide sandwich was designed using styrofoam and inserted tightly into a modified blue foam liquid nitrogen dewar (Fig. S1C; Spearlabs Cryogenic Products). The styrofoam holder contains a shallow well sized to the assembled quartz glass sandwich and is lined with aluminum foil to encourage omnidirectional irradiation (Fig. S1C arrow). This assembly allowed for the loading and unloading of grids under liquid nitrogen conditions (Fig. S1D), and it permitted the placement of the UVC light source directly above the samples.

The UVC light source (6W Germicidal Light T5 Tube UVC Sterilizer, Lcamaw via Aliexpress.nl) was mounted to the underside of a box to allow the placement of the blue sample assembly and a UVC sensor (UV Light Meter LS126C, Linshang Technologies, China) directly below the light source (Fig. S1E). The UVC sensor was placed adjacent to the sample assembly at sample height to confirm irradiation and dose rate. At the sample, the dose rate from the light source reached a maximum of $490 \mu\text{W}/\text{cm}^2$, as determined with the final reading before discontinuing UVC treatment. Based on this setup, a box was designed to properly contain the light source, sensor, and sample assembly (Fig. S1F).

Samples were irradiated as follows: During each irradiation experiment, four sample-containing grids were processed. Three of the grids are transferred to a position of the quartz grid holder. The fourth grid was left in the grid box with the lid closed to act as a control (grid box lid is opaque and grid remains perpendicular to the light source, preventing the passage of UVC to the sample). The liquid nitrogen level was then raised to a level of 0.5 cm above the sample, which we have

marked on inside of the blue foam container (91). Prior to irradiation, the UVC light was switched on for one minute (prewarming step) and then switched off. Immediately after sample assembly and pre-warming, the lamp is placed over sample assembly, and the lamp switched on for the treatment time. For the bacterial sample, grids were treated on the carbon side only; for the bacteriophage sample, irradiation occurred on both the carbon and copper side of the grids (by inverting the sandwich in the liquid nitrogen/vapor layer). Once treatment was complete, the grids are transferred back to the grid box and stored in liquid nitrogen until the confirmation of inactivation and or imaging.

CFU and PFU

To determine the exposure time for UVC treatment of *V. cholerae* or the ICP1 bacteriophage, the viability of the samples was determined by either colony forming units (CFU) for the *V. cholerae* WT, or plaque forming units (PFU) for the bacteriophage exposed to *V. cholerae* N16961-TndsRed. The treated grids were transferred to LB, pulse vortexed several times to resuspend the bacteria/phage and then subjected to serial dilution. CFUs were determined by plating 100 μ l of the serial dilution onto non-selective LB plates and incubated overnight at 30°C. The PFU were determined as follows: *V. cholerae* N16961-TndsRed containing soft agar was overlayed on square LB plates containing 10 μ g/ml gentamycin. 5 μ l from each dilution step was spotted onto the top layer and the plate left to grow overnight at room temperature. Clearance zones were noted the following day, and PFU were roughly determined. The duration of UVC exposure to inactivate greater than 99.99% of the phage was determined based on the amount of time needed to prevent ICP1 predation of *V. cholerae*, demonstrated by the lack of clearance zone.

Imaging conditions

Cryogenic electron tomography

Suitable grids containing vitrified, UVC-treated *V. cholerae* were clipped and loaded into a CS-corrected Titan Krios (TFS) equipped with a K2 direct electron detector and a post-column energy filter (Gatan, Inc.) set to zero loss imaging with a 20 eV slit. Targets were chosen based on the presence of the flagellar pole in a hole. This extracellular feature is a good indicator for the presence of the F6 chemotaxis array that is located at the same cell pole. A tilt series of each target was collected using SerialEM v3.8.5 set to a dose symmetric tilt scheme between -54° and 54°, with 2° increments, with a pixel size of 3.49 Å (72, 98). A defocus of -8 μ m and a cumulative dose of 140 e⁻/Å were used as targets.

For the untreated data set, we used data collected during a previous session. This data was collected on a Titan Krios (TFS) microscope equipped with a K3

BioQuantum direct electron detector and energy filter (Gatan, Inc) set to zero loss imaging with a 20 eV slit. Whole cells in a hole were selected as targets. Tilt series were collected using a bidirectional scheme between -60° and 60° with 2° increments with a pixel size of 5.86 Å. The target defocus was set to $-8\text{ }\mu\text{m}$ and the estimated total dose $170\text{ e}^-/\text{Å}^2$.

Single Particle

Suitable treated and untreated ICP1-containing grids were clipped and loaded into a Titan Krios (TFS) microscope equipped with a K3 BioQuantum direct electron detector and energy filter (Gatan, Inc.) set to 20 eV. Micrographs were collected using the TFS EPU software equipped with AFIS (aberration free image shift) with a pixel size of 0.685 Å in super-resolution mode. Defocus was set cycled between -1 and $-3\text{ }\mu\text{m}$, and a dose of $34\text{ e}^-/\text{Å}^2$ per image.

Apoferitin samples were treated as described in Diebolder et al (99). Briefly, grids were loaded into a Titan Krios electron microscope (TFS) operated at 300keV, equipped with a Gatan K3 BioQuantum direct electron detector (Gatan, Inc). Movies with 50 frames and an accumulated dose of $50\text{ e}^-/\text{Å}^2$ were acquired in super resolution counting mode using EPU (TFS) at the magnification of 130,000X, corresponding to a calibrated pixel size of 0.328 Å/pixel with a defocus range of -0.5 to $-2.5\text{ }\mu\text{m}$. A total of 1,040 movies were collected at The Netherlands Centre for Electron Nanoscopy (NeCEN). Detailed data acquisition parameters are summarized in Supplementary Table S1.

Data processing

Vibrio cholerae

Motion correction and tomogram generation were done using the IMOD v4.11.1 image processing suite (73). In brief, once the tilt series were motion-corrected using the alignframes function, the batchruntomo function was used to generate the initial tomograms to determine if the structure of interest was present in the cell (final bin = 3 without CTF correction)(74). Tomograms containing the feature of interest were further processed by refining the bead model or using patch tracking if insufficient beads were present. Subsequently, the boundary model was improved, CTF correction was applied, and a back-projected, SIRT-like filtered tomogram was generated (100). A final bin of 2 was used for the UVC treated data (pixel size = 6.98 Å) and a final bin of 1 for the untreated data.

The resulting tomograms were used for STA using the Dynamo v9.6.0 imaging suite (101, 102). Subtomograms were manually picked from chemotaxis array top views. Two rounds of iteration steps were performed, using a template generated from particles picked from a single tomogram, and a mask that encompassed a single

hexagon. All final maps were calculated from weighted back-projection SIRT-like filtered tomograms. The resolution of the final maps were calculated using ResMap v1.1.4 (103).

ICP1

Reconstruction of the ICP1 capsid was done using Relion 3.1.2 (104). The data was binned by 4 for the initial particle picking, 2D, and 3D refinements. GPU enabled MotionCorr2 was used to correct particle movement as part of the Relion processing suite and gCTF v1.06 was used for CTF estimation (105, 106). Initially, 150 phage full and empty heads were manually picked for 2D classification to generate reference templates for autopicking. Following autopicking and extraction, 2D classification was performed using the T4 phage head, PDB 8661, filtered to 70 Å as a reference (107). 3D classification was performed with a subset of particles using the 2D classification full head as a template. The full head class was auto-refined using “1” symmetry. Post processing used a mask generated by Relion. Particles were re-extracted with a pixel size of 1.637, 3D autorefine and postprocessing was repeated yielding the final structure.

Apoferitin

RELION-3.1 beta software was used for ApoF image processing (104, 108). Collected movies were subjected to beam induced drift correction using MotionCor2, the contrast transfer function was estimated by CTFFIND-4.1.18 (106, 109). RELION Gaussian picker was used to automatically pick 251,350 particles. After two rounds of 2D classification, false positive and contaminating features were discarded resulting in a 66,920 particles dataset. Ab-initio model generation followed by 3D classification and 3D refinement yielded a 2.6 Å map. Corresponding particles were subjected to CTF refinement for optical and beam-tilt and aberration correction, as well as per-particle defocus, and per-micrograph astigmatism correction followed by Bayesian polishing (110, 111). A second 3D refinement was then performed yielding a 2.1 Å map.

Map resolutions were estimated at the 0.143 criterion of the phase-randomization-corrected FSC curve calculated between two independently refined half-maps multiplied by a soft-edged solvent mask. Final reconstructions were sharpened and locally filtered in RELION post-processing. Model refinement and validation statistics are summarized in Supplementary Table S2. Maps were displayed using UCSF ChimeraX (112).

Molecular modeling and simulations

A model of the major capsid protein was constructed using the gp122 sequence (YP_004251064.1) and AlphaFold Colab (113, 114). A hexameric complex was

assembled into each map by rigid docking using UCSF Chimera v1.13 (115). A 5-ns molecular dynamics flexible fitting (MDFF) simulation was performed on each hexamer using NAMD v2.13 and the cascade-MDFF protocol with default parameters (116, 117). Fittings were carried out with an MDFF coupling constant of 0.1 and symmetry restraints applied on the backbone atoms of each monomer. Structural visualization and trajectory analysis were performed in VMD v1.9.4 (118).

Accession numbers

The structures resulting from single particle analysis of the untreated and UVC-treated ICP1 bacteriophage data (EMD-13403 and EMD-13402, respectively), and the UVC-treated ApoF (EMD-13364; PDB ID-7PF1) data have been deposited in the EMDB and or PDB.

Results

UV inactivation of *Vibrio cholerae*

As an initial test of the UV inactivation device, we determined the UVC exposure time necessary to inactivate the pathogen, *V. cholerae* A1552 WT. Our experiments showed a significant reduction in vitrified, viable cells after 20 s of UVC exposure, and complete inactivation with 30 s of UVC exposure. Based on this information, we chose 30 s as the timepoint for inactivation and subsequent imaging.

Following the UVC treatment of the *V. cholerae* cryo-EM sample, the grids were transferred to a Titan Krios electron microscope for data collection. To determine the effect of the UVC irradiation, we collected tilt series of the flagellar poles of individual cells, with the aim of imaging the F6 chemotaxis array, which are located at the same pole. Chemotaxis arrays are well-studied by ECT and STA, and thus provided a good model system for determining of macro-level damage to cells. Following data collection and subsequent processing, tomograms with top views of the F6 chemotaxis array were identified and further processed using STA (Fig. 1A/C). For the control sample, and using 219 particles, we were able to achieve a resolution of 22.6 Å (Fig. 1B), whereas with the UVC-treated sample and 170 particles, we were able to achieve a final resolution of 26.7 Å (Fig. 1D).

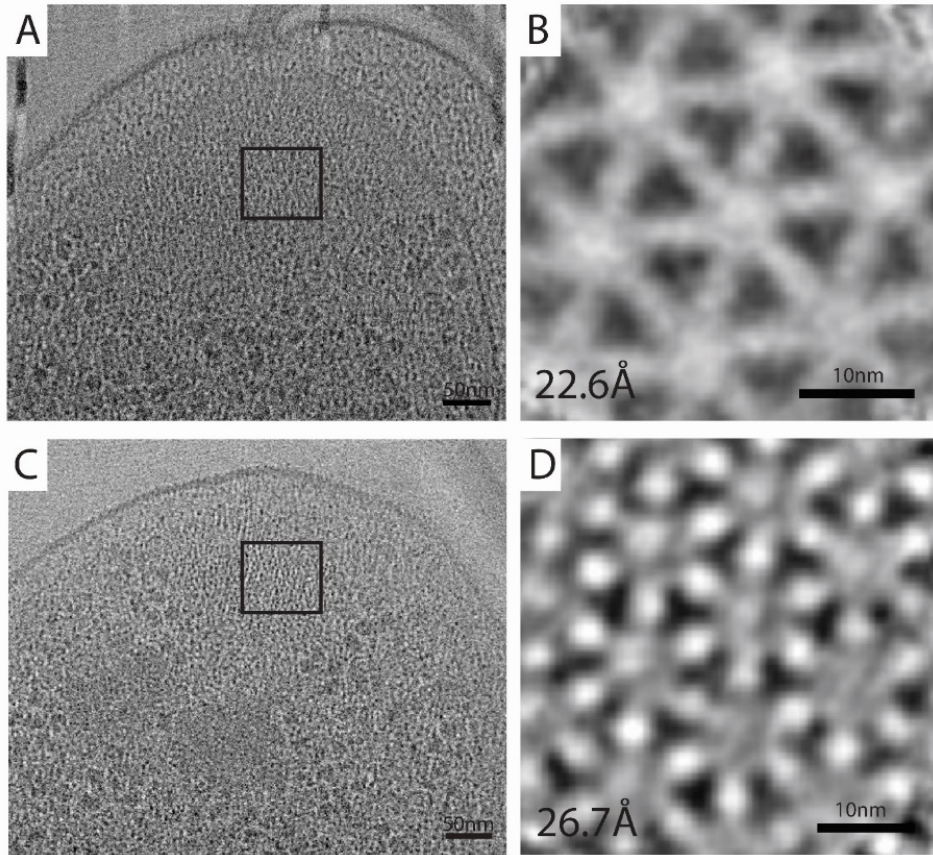


Figure 1. Effect of UVC irradiation on *Vibrio cholerae* and its chemotaxis array. Panels A and C show the flagellar pole region of untreated (A) and UVC-treated (C) *V. cholerae* cells, highlighting the top view of the F6 chemotaxis array (black box). Panels B and D are the results of subtomogram averaging of F6 chemotaxis cluster, showing the typical hexagonal arrangement of the trimer-of-dimer receptors in extended arrays.

UV inactivation of ICP1 phage

The ICP1 bacteriophage was chosen as a model for a virus-like particle. We determined the UVC exposure time that was necessary to inactivate greater than 99.99% of the phage. This was determined to be 60 s for the carbon side and 30 s for the copper side (Fig. 2A). We then UVC irradiated a new set of ICP1-containing grids, confirmed inactivation of phage, and used the remaining grids for imaging (Fig. 2B).

Following imaging, the number of particles and classes was determined before subsequent processing. For the UVC-treated sample, 6577 particles were separated into two classes: capsid containing DNA and empty capsids. This was done because previous research in our group had shown that the size of the empty capsid is

slightly larger than the capsid containing DNA (unpublished results). Here, only capsids containing DNA were used for 3D classification and refinement. Ultimately, 2845 particles resulted in a final resolution of 5.1 Å. A similar methodology was used for a separate, untreated data set, which resulted in a final resolution of 6.0 Å using 4096 particles. A comparison of the two structures using Chimera Fit in Map yielded a correlation value of 0.9855. The achieved resolutions allowed for the identification of the T number ($T=13$; Fig. 2E; (119)) which is a metric for the icosahedral symmetry, and the flexible fitting of the putative major capsid protein (gp122) into the map (Fig. 2F).

To compare the local quality of the two maps, we used each to structurally refine a hexameric assembly of the major capsid protein (Fig. 2F). For this purpose, we carried out molecular dynamics flexible fitting (MDFF) simulations (Methods), which use a density-derived potential to optimize model-map overlap (116). The refined hexamer models were nearly identical, possessing a backbone root-mean-square-deviation (RMSD) of 1.9 Å for all residues and 1.1 Å for non-loop residues. The backbone RMSD between the refined and initial hexamer models was 3.4 Å and 3.3 Å, respectively, for the untreated and UVC-treated maps. The structural information contained in both maps is therefore of comparable quality.

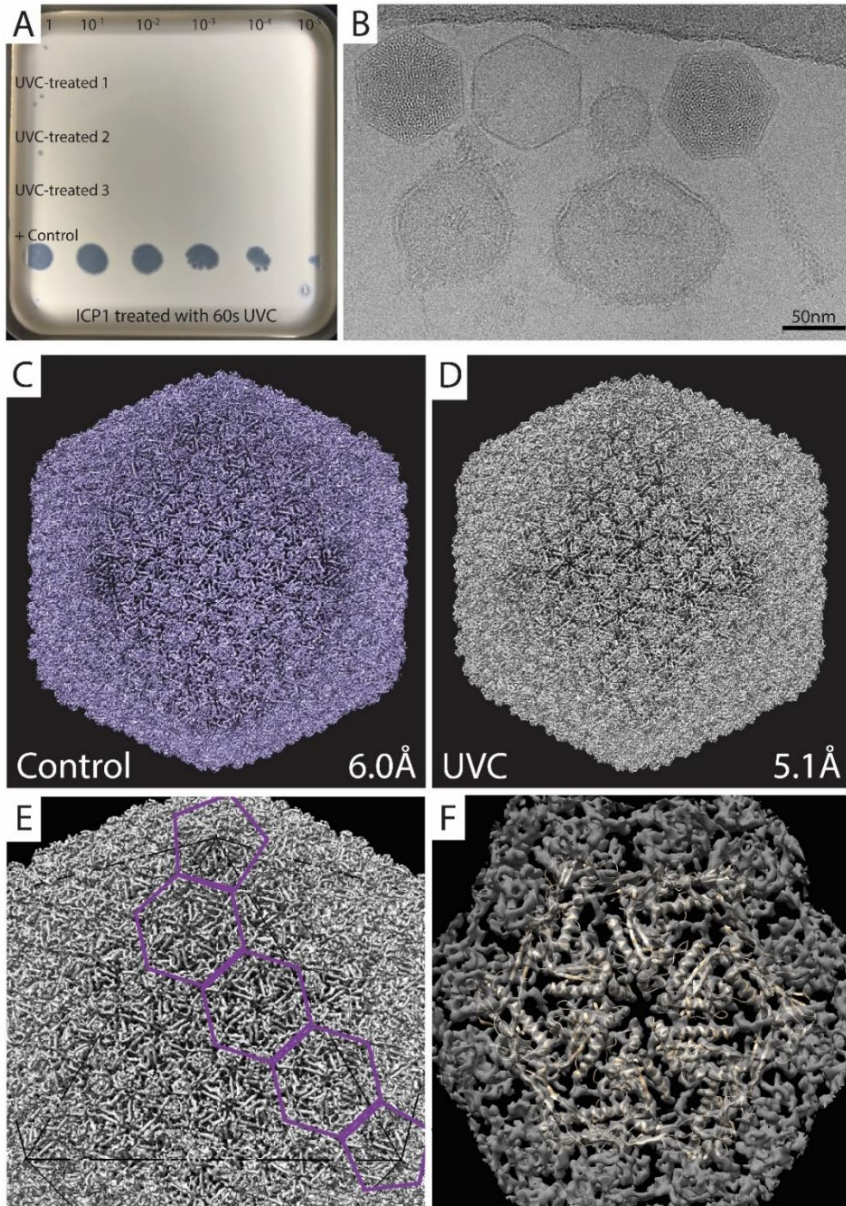


Figure 2. UVC treatment and SPA of ICP1. A. UVC treatment of ICP1 resulted in a significant reduction in viable phage. Rows 1-3 are UV treated and show 0-2 infective phages in three replicates when undiluted (dilution factor noted at the top of panel). Row 4 is a negative control, a grid containing ICP1 that remained in the grid box during treatment. B. A representative micrograph of UVC-treated ICP1 showing an assembled phage (far right), an empty and full head (middle/left), and liposomes (round, bottom). C & D. SPA analysis resulted in structures of the control and UVC treated ICP1 phage with resolutions of 6.0 Å and 5.1 Å, respectively. E. Determination of the T number = 13, which a measure of the icosahedral symmetry. F. Flexible fitting of putative major capsid protein, gp122, as a hexamer, and docked into the ICP1 capsid of the UVC-treated structure noted in D.

UV inactivation of ApoF

Finally, we wanted to determine the effect of UVC irradiation at resolutions similar to x-ray crystallography, which allow the visualization of individual amino acids. To do this, we used the protein complex, apoferritin (ApoF). ApoF is commonly used in EM facilities to determine the performance of microscopes and it has been well characterized by the scientific community using cryo-EM and x-ray diffraction. Using the same UVC exposure time as ICP1, grids containing apoferritin were treated with UVC for 60 s on the carbon side and 30 s on the copper side. These grids were subsequently imaged and the data processed using SPA. Our experiments demonstrate that we were able to achieve a final resolution of 2.1 Å in the UVC-treated sample, which is on par with structures published in the Protein Data Bank (<https://www.ebi.ac.uk/pdbe/node/1>).

A comparison of the UVC treated apoferritin with untreated samples and published structure found no difference between the two structures (Fig. 3; EMD-3853 (unpublished), PDB5N27 (120)). A closer analysis of selected regions of the structure of the treated apoferritin sample highlight the structural preservation (Fig. 3B, C).

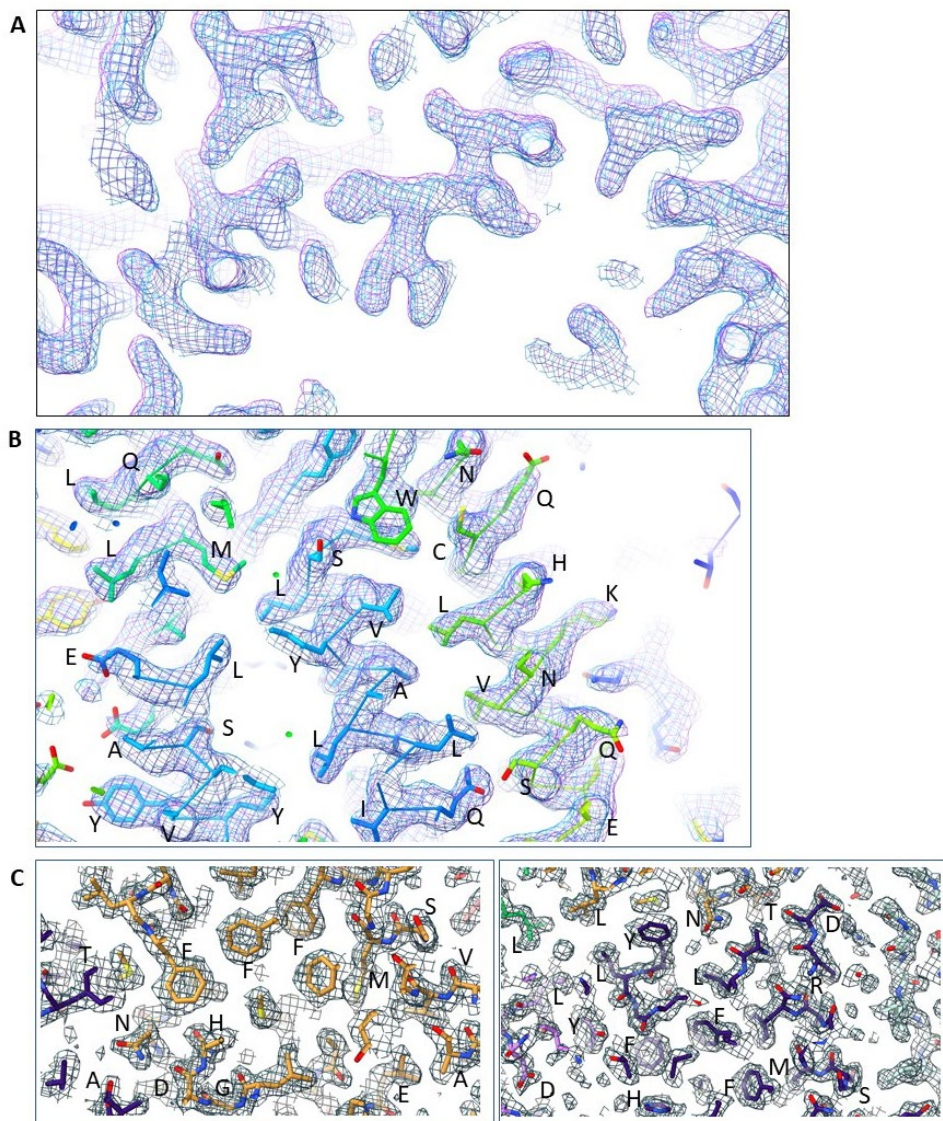


Figure 3. Representative ApoF amino acids show no difference between crystal structure and UVC-treated ApoF cryo-EM map A. A comparison of the UV-treated ApoF map (blue) with a previously published, untreated structure (purple; EMD-3853) shows no difference between structures. B. The UV-treated ApoF map (blue) superimposed with an untreated map (EMD-3853) and fitted model (PDB-5n27) confirms no significant differences. C. Close-up view of UV-treated map with the fitted model (PDB-5n27), highlighting no difference between representative amino acids that might be impacted by irradiation.

Discussion

UVC irradiation is a widespread technique used for disinfection (121, 122). In this paper, we demonstrate that UVC irradiation is also suitable for inactivating pathogens in cryogenic samples intended for structural analysis by cryo-EM. Our results confirm a significant reduction and or elimination of the ICP1 bacteriophage and its target organism, *V. cholerae*. We characterized the effects of this treatment by comparing cryo-EM data of control (untreated samples or previously published structures) with samples after treatment and inactivation. Here, we show at multiple scales that UVC irradiation has no discernable effect on the structural information of the biological cryo-EM samples.

Cryo-EM has become a valuable method for understanding bacterial cell biology. Using cryo-ET, the organization of bacterial cells and their molecular machines have become accessible for structural analysis. Thus, we began by determining the effects of UVC irradiation on a widely studied bacterium. We show that while the bacterial pathogen *V. cholerae* is completely inactivated by UVC, the cell's ultrastructure is indistinguishable from untreated samples. More specifically, using the F6 chemotaxis array as an example, we show that the STA results (reaching resolutions between 2-3 nm) are similar to the published literature for complexes of similar size and in cells with similar thicknesses(88, 123–125).

We next wanted to test the suitability of this treatment method on a virus-like particle. We therefore tested the UVC treatment on ICP1, a bacteriophage that infects *V. cholerae*. Similar to the bacterial sample, the bacteriophage was also effectively inactivated using the UVC treatment of the cryogenic samples. The resolution reached here (~ 5 Å) allowed for the identification of individual alpha helices, turns within the protein, and groups of beta sheets. This information was used gain structural information about the ICP1 capsid, including its overall structure as demonstrated by its T number, a spike protein complex at the vertices (data not shown), and the docking of the putative major capsid protein into the capsid hexamer. This result further illustrated the suitability of the UVC inactivation method for low-resolution SPA of virus-like particles.

Finally, we demonstrated the applicability of this method for high-resolution SPA. At resolutions of better than 3 Å, structural damage would likely be visible by the lack of disulfide bonds and damage to aromatic amino acids. Our experiments show that UVC irradiation had no impact on our ability to obtain a final structure of ApoF at a resolution of 2.1 Å (Fig. 3). This resolution is comparable to other reported structures (EMD-3853 (unpublished), PDB5N27 (120)). A closer examination of the

treated and untreated data did not reveal any noticeable differences between the two structures (Fig. 3).

The results of this study are of particular significance to groups studying pathogens with a potential for human infection. We show a 5-fold reduction in infectious particles when ICP1 is treated with UVC. The treatment, combined with the significant reduction of infectious particles that are associated with the blotting step of plunge freezing reduce the remaining viable particles. Furthermore, in the case of unintentional dropping of the sample at any point during loading, imaging or removal from the cryo-EM, the particles are subject to the ambient environment or the vacuum of the microscope, which further increases the likelihood of their inactivation. Therefore, pathogenic specimen would likely be safe to image on a cryogenic electron microscope approved for lower safety levels.

This research did not come without some challenges. For instance, our initial experiments to determine PFU used the same strain of *V. cholerae* as used for the cryo-ET and STA. However, we found that this strain and antibiotic combination gave inconsistent PFU counts and thus necessitated a switch to a strain more similar to the ICP propagation protocol. When working with the ICP1 sample, we also found many factors could influence the reduction in infectious particles, including contamination from forceps, bending of the grids during transfer, and the presence of outer membrane vesicles/lipid containing particles in the sample preparations. Thus, it will be important to determine the needs for their specific sample prior to imaging.

Together, this research demonstrates that UVC irradiation of vitrified samples can provide significant structural information for a variety of samples and across scales. We believe this information is especially useful for labs who study pathogens that may not be approved for imaging at their local, regional, or national facilities. We demonstrate that UVC treatment of the samples directly on the grid preserves the structural information while rendering the pathogen with reduced or no infectivity. It is important to note that the inactivation protocol will have to be adapted to each pathogen of interest. Researchers will need to work with their local biosafety officers to determine the applicability to their specific pathogen and research environment. Regardless, this inactivation method provides an affordable, straightforward method to inactivate pathogens for cryo-EM studies and will be useful for all laboratories lacking access to cryo-EM facilities that are certified for higher biosafety level microorganisms.

Acknowledgments

We are grateful to Davi Ortega for helpful discussions. We also wish to thank Dr. Weng Yang and Dr. Willem Noteborn of NeCEN for assistance during data collection, and Gert Koning (Department of Fine Mechanical) for assistant with the construction of the prototype UVC inactivation box.

Funding

This work was funded by the Building Blocks of Life Grant 737.016.004 from the Netherlands Organization for Scientific Research and Instruct-ULTRA (Horizon 2020 Coordination and Support action Number ID: 731005. Microscope access was partially funded by Netherlands Electron Microscopy Infrastructure (NEMI) grant 84.034.014.

Author Contributions

JSD, LMM, GJJ, GPR and AB designed the research. JSD, LR, NA performed experiments. JSD, LR, NA and CKC analyzed data. JSD, LR, NA, CKC and AB wrote the manuscript. All authors read and commented on the manuscript.

Competing interests

The authors declare no competing interests.

Supplemental Figures

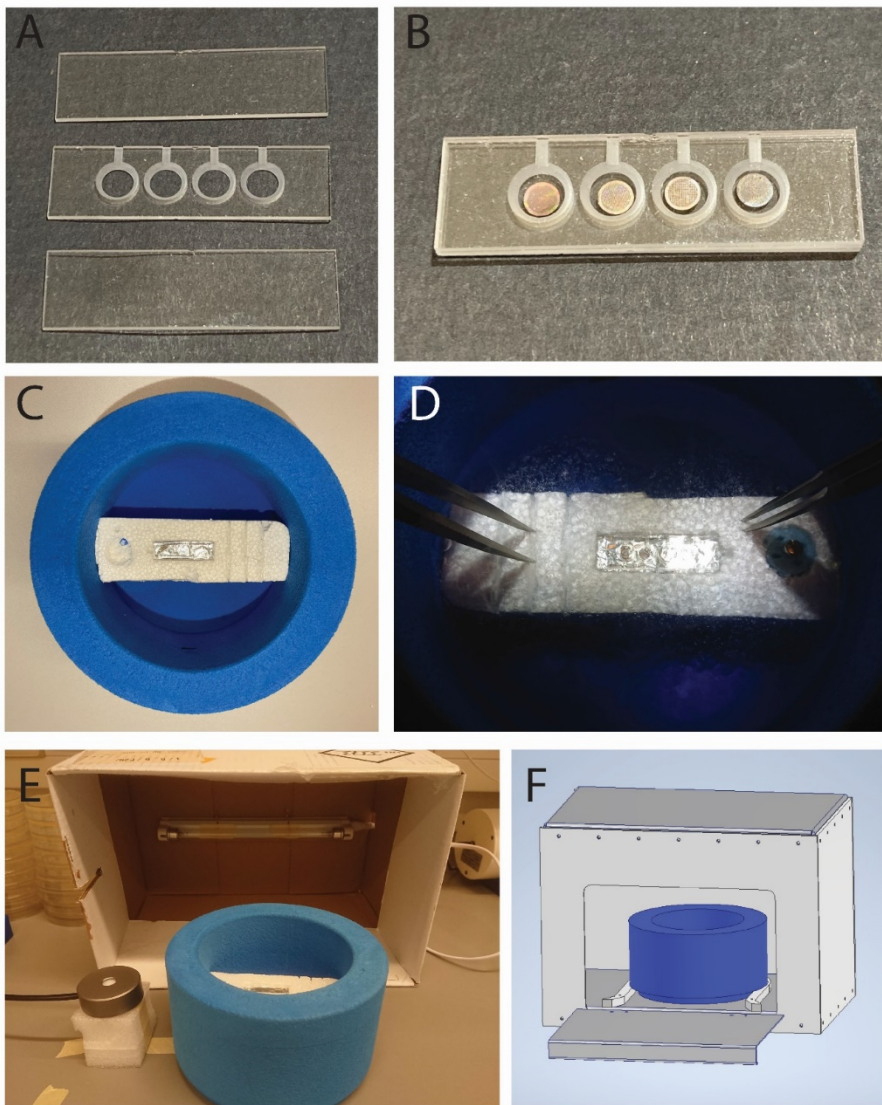


Figure S1. Details of UV inactivation device. Sample containing grids can be loaded into a quartz glass grid holder (unassembled (A) and assembled with grids (B)) under liquid nitrogen conditions. A foam dewar contains a Styrofoam platform for the placement of the quartz glass sample holder during assembly and inactivation, and includes a place for the grid box, an aluminum-lined well for the assemble sample holder (white arrow) and slots for storing each quartz plate (at room temperature (C) and cooled with liquid nitrogen (D)). The initial design of the UV light box mounted the light source to the inside of a cardboard box that could be placed over the cooled sample and UV sensor (E). The final design of the UV light box allows for insertion of the foam dewar into the side (visualized in F).

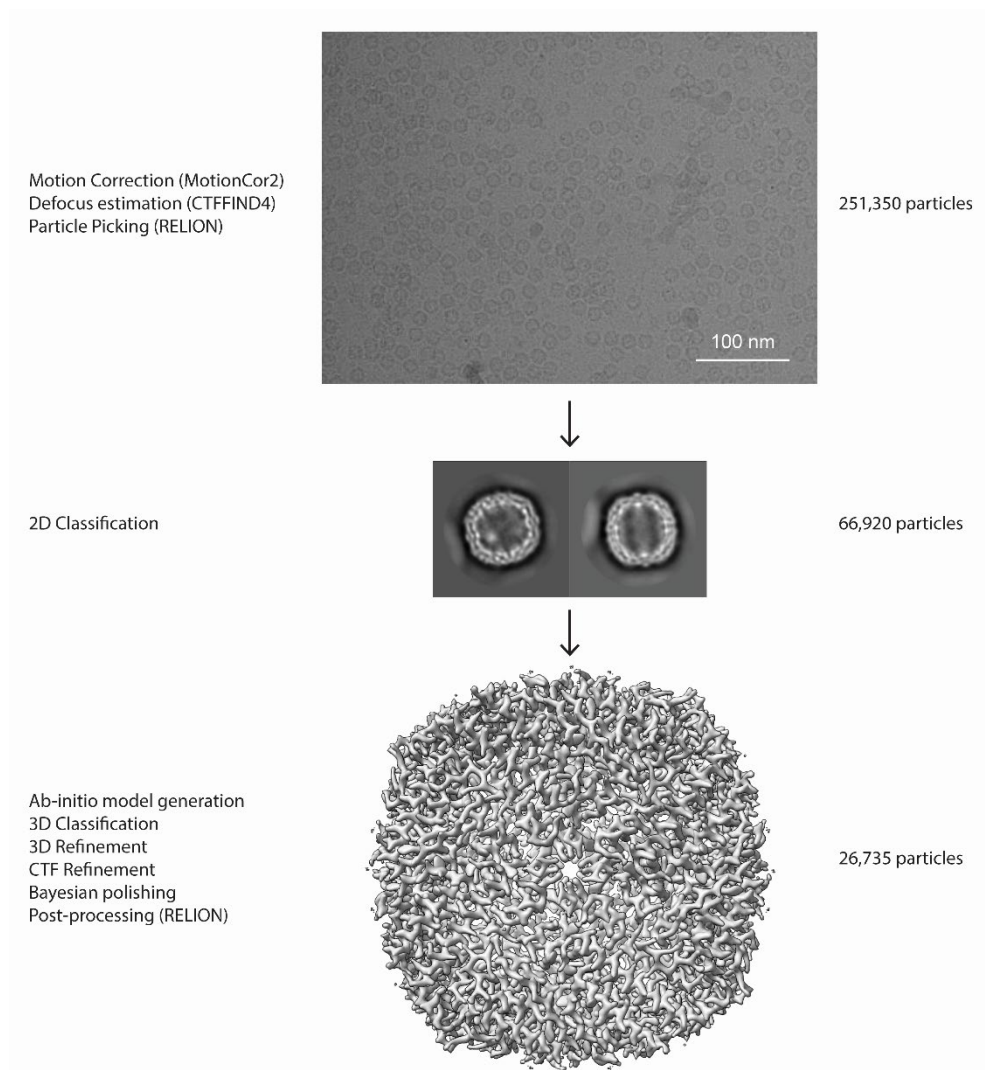
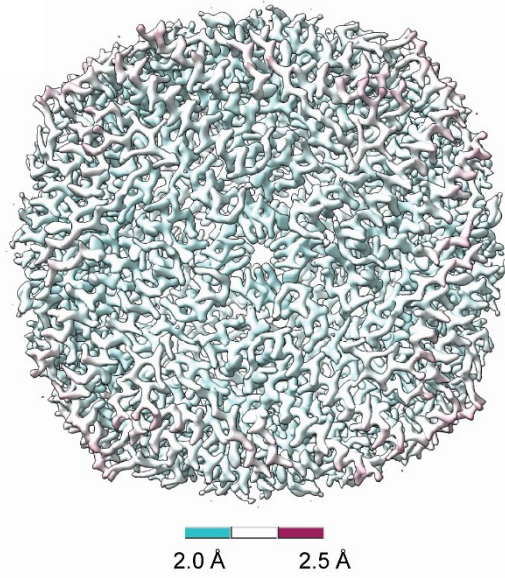


Figure S2. Cryo-EM data processing workflow. A typical micrograph shown as well as representatives 2D classes. 3D classification was performed to distinguish heterogeneity in the sample and the final refined map is showed.

A



B

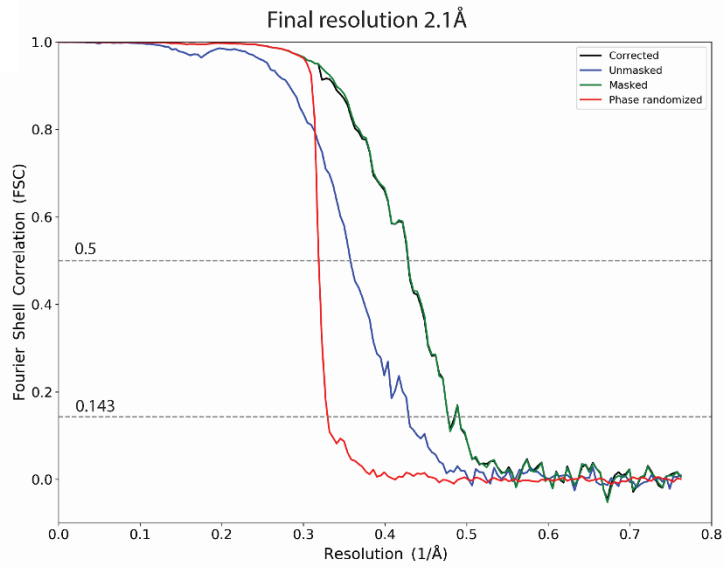


Figure S3. Resolution assessment of cryo-EM structure. A. Local resolution map. B. Global resolution assessment by Fourier shell correlation at the 0.143 criterion.

Table S1. Cryo-EM data collection parameters and processing

	Apo ferritin
Magnification	130,000
Pixel size (Å)	0.328
Voltage (keV)	300
Electron exposure (e⁻/Å²)	50
Frames	50
Defocus Range (μm)	-0.5 to -2.5
Number of movies collected	1040
Particles extracted	251,350
Final	26,735
Symmetry	C ₃
Masked resolution at FSC=0.143 (Å)	2.1
Map sharpening B-factor (Å²)	-44

Table S2. Model refinement and validation statistics

	UVC treated Apoferritin
PDB	
Model compositions	
Amino Acids	4123
Glycans	N/A
Mean B factors (\AA^2)	
Amino Acids	15
Glycans	N/A
R.M.S. deviations	
Bond lengths (\AA)	0.002
Bond angles ($^\circ$)	0.434
Validation	
MolProbity score	1.36
Clashscore	6.54
Rotamers outliers (%)	0.25
EMRinger score	6.91
Ramachandran plot	
Favored (%)	98.28
Allowed (%)	1.50
Outliers (%)	0.22

CHAPTER 6

Advanced methods for processing of large volume samples for cryogenic electron tomography

Jamie S. Depelteau¹, Jeroen Mesman², Janine Liedtke¹, Katrina A. Gundlach¹, Ariane Briegel¹

¹ Department of Microbial Sciences, Institute of Biology Leiden, Leiden University, Sylviusweg 72, 2333 BE Leiden, The Netherlands

² Department of Fine Mechanics, Leiden University, The Netherlands

Abstract

To understand complex biological systems, we need to gain insight into individual cells in the context of multicellular systems. However, the structural details about how cells interact with each other in complex systems remains elusive, mainly due to their volume. Recently, techniques such as cryogenic electron tomography (cryo-ET) can be used to visualize individual cells at macromolecular scale. A variety of techniques have been developed for examining large volume samples, including high pressure freezing, freeze substitution, ultramicrotomy, and cryogenic focused ion beam scanning electron microscopy (cryo-FIB SEM). In combination, these techniques have provided the means to gain unique insights into multicellular structure, but their application are still not routine and they are affected by artifacts from sample preparation steps. Here, we set out to develop a new workflow based on new and already available methods to prepare large volume samples suitable for cryo-ET. We tested our workflow using variety of different samples, including animal and plant tissue as well as bacterial colonies. We found that conventional pulled glass needles were unsuitable for nanobiopsies, leading us to explore the 3D printing of acrylic needles. These needles allowed us to successfully obtain core samples from bacterial colonies on an agar plate and demonstrated the potential to obtain a sample from soft tissue. The isolated nanobiopsy samples were then high pressure frozen, recovered, and stored for trimming steps. In addition, we were able to freeze samples directly on grids, which were then further processed by ultramicrotomy and imaged using cryo-FIB SEM. Together we show that the acrylic needles offer a unique opportunity to collect a sample at the micrometer scale which is suitable for subsequent processing as preparation for cryo-ET.

Introduction

Understanding the complex biological world at the nanoscale is a challenging endeavor. A key component to achieving this goal is visualizing these processes within the cellular and multicellular context. In the past, many imaging techniques have been developed to examine individual cells and their contents. However, only a few of these methods can resolve details at a high resolution to visualize individual large proteins or protein complexes.

In the past years, cryogenic transmission electron microscopy (cryo-TEM) has become an essential tool to study biological samples in a near-native context with optimal structural preservation (2, 75). For cryo-TEM, thin samples such as small cells or isolated protein complexes can be used. The typical workflow of the cryo-TEM sample preparation consists of pipetting a sample onto an EM support grid, removal of the excess liquid by blotting with filter paper, and plunge freezing the sample into a liquid nitrogen cooled cryogen. This preparation step immobilizes the sample in non-crystalline, amorphous ice while preserving its delicate ultrastructure (1). Once inserted into the cryogenic electron microscope, the sample can be imaged. Subsequent computational methods are then used to reconstruct a 3D volume of the sample.

Two types of cryo-TEM are regularly used for imaging of biological samples: single particle analysis and cryogenic electron tomography (cryo-ET). Single particle analysis focuses on protein or protein complexes and relies on a homogeneous sample. However, for samples that are heterogeneous, such as entire small cells or tissues, the method of choice is cryo-ET. This technique requires tilting of the sample while collecting multiple images of the same target. The resulting set of images can then be used to generate a 3D volume of the target at macromolecular resolution. Both techniques are now routinely used to address a wide variety of biological questions, including protein complex structures and their conformational changes, to the structure and function of macromolecular machines in their cellular context (for example, the flagellar motor; the spike complex of SARS-CoV-2 ; and the F6 chemotaxis array)(79, 86, 125).

To truly understand how those molecular machines are used and function within an even more complex system like tissue, biofilms and others, detailed insight into the structural interactions between cells and tissues is necessary. To address such research questions, cryo-ET has also proven very powerful for exploring the inner depths of cells and tissues (84, 88, 126–128). However, imaging such highly complex samples to investigate interactions between cells and tissues poses many

challenges that have so far limited the application of cryo-ET. The goal of this work is to develop techniques and workflows that allow for the ultrastructural analysis of large volume samples (LVS) using cryo-ET. LVSs are defined as samples that cannot be processed through the well-established cryo-EM workflow outlined above.

Plunge freezing is limited to a sample thicknesses of approximately 5-10 μm depending on the type and contents of the sample (1). Widely used samples that reach this thickness limitation are eukaryotic cells that are directly grown on gold support grids. When the cell attaches and spreads across the grid, the outer regions of the cell are within the vitrification range of plunge freezing. However, the cell thickness increases around the nucleus of the cell. These thicker areas of the cell often cannot be properly vitrified. Instead, crystalline ice formation is common in these areas, and the result of this improper freezing compromises the ultrastructural information of the sample. Thus, any sample that exceeds the thickness limitation for vitrification by plunge freezing is defined as a LVS and requires an alternative preparation process (Fig. 1). In this case, samples are prepared primarily by high pressure freezing (HPF). HPF is able to fully vitrify samples up to a thickness of about 250 μm using high pressure, extreme cold, and short freezing protocols (5, 129).

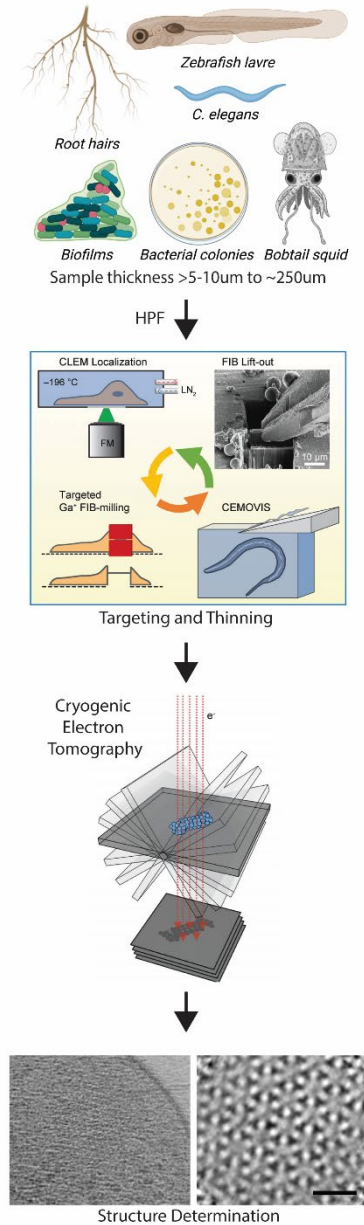


Figure 1. Overview of large volume workflow for cryogenic electron microscopy. Examples of large volume samples (created in Biorender.com). Once the sample is vitrified by high pressure freezing (HPF), additional sample thinning must occur. Traditionally this occurs using cryo-FIB SEM to either directly make lamella or in combination with a cryo-lift out device, or by direct thinning using CEMOVIS. These thinning methods can be targeted to areas of interest using CLEM. Once the target thickness of ~200 nm is achieved, the sample is transferred to the EM for image cryo-ET. The 3D volume is computationally reconstructed, which can then be used for structure determination (left, top view of F6 chemotaxis array in a *Vibrio cholerae* cell; right, sub-tomogram averaging of the top of F6 chemotaxis system revealing the hexagonal structure). Adapted from (2).

Despite the possibility to vitrify such large samples, they remain too thick for direct imaging with cryo-TEM. For instance, using the eukaryotic cell example noted above, as you approach the nucleus, the electron beam is unable to penetrate the sample, which produces a black image that is devoid of useful information. The general rule of thumb for suitable sample thickness is that two times the electron voltage is the maximal sample thickness (in nanometer) that can be effectively imaged with cryo-EM (130). For example, using a cryo-EM with an electron source operating at 300 keV, samples with a thickness of up to 600 nm are considered the upper limit that will result in interpretable data. However, in the case of cryo-electron tomography, the sample is tilted during data collection, which increases the thickness at higher tilt angles. In general, thinner samples lead to higher resolution data, and the optimal sample thickness for imaging is about 150-200nm. Thus, cryo-EM is still significantly limited by the types of samples that can be imaged. To make this imaging method accessible for LVSs, the samples need to be both properly vitrified and subsequently thinned to a thickness that is compatible for the commercially available cryo-electron microscopes (Fig. 1).

One established method for the thinning of thick cryo-TEM samples is to thinly section the frozen sample using glass or diamond knives in a cryo-ultramicrotome. This procedure is similar to preparing plastic sections for traditional EM. However, in the case of the cryo-TEM sample, the ultramicrotome has a cryo-chamber attached, and specialized knives are used for trimming and producing sections of 70-300 nm at cryogenic temperatures. This technique is called cryogenic electron microscopy of vitreous sections, or CEMOVIS (Fig. 1) (6, 7, 131–133). CEMOVIS has been used successfully for the last twenty years, though it is known to require specialized training to do it well. Additionally, the sectioning process cause a number of known artifacts, such as compression and tears in the sections (134). The challenges and artifacts caused by CEMOVIS have limited its application for cryo-ET to a few specialized research groups. Nevertheless, it remains a valuable technique for thinning of LVS.

In recent years, advances in cryogenic focused ion beam (FIB) scanning electron microscopy (SEM) (cryo-FIB SEM) have made this method increasingly popular to process LVSs. With this technique, the SEM beam is used for targeting and monitoring of the vitrified sample, and an ion beam is used to remove enough material to allow imaging in the cryo-TEM (Fig. 1). The target thickness of these lamella is roughly 200 nm, though thinner is possible and may be advantageous depending on the biological questions. Currently this process is most often applied to eukaryotic cells that have been grown on a grid. But cryo-FIB SEM has also been used for the processing of even thicker samples such as biofilms and even an intact

C. elegans worm (84, 88, 135). Despite its proven potential for answering crucial biological questions, this technique can be daunting and time consuming. It requires many transfer steps that can introduce contamination to the sample, and it can take seven to eight hours to generate a limited number of lamella. Furthermore, the starting sample thickness before milling is limited to 20 μm or less. Thus, for samples of greater size, additional thinning steps are required before it is possible to mill with a cryo-FIB SEM and subsequent imaging with cryo-TEM.

Here we set out to develop novel LVS preparation methods for cryo-EM imaging. Building on established methods, we developed a biopsy needle designed to collect samples directly from the organism of interest. The sample-filled needle is then subjected to HPF, and ready for subsequent trimming either a cryo-ultramicrotome or cryo-FIB SEM, or both. The resulting thinned samples are destined for the cryo-TEM. After several iterations, we successfully collected core samples of *Streptomyces coelicolor* grown on solid media. This study provides evidence that biopsies at the microscale are obtainable, and with continued experimentation, this technique could open a new avenue for LVS processing and imaging by cryo-ET. Ultimately this technique will provide a new route to visualizing the multicellular complexes with unprecedented resolution.

Methods and materials

Biological specimens

Streptomyces coelicolor M145 was grown on minimal media supplemented with 1% mannitol and 1% glycerol as a carbon source. Production of the dark brown color was due to a pigmented antibiotic, actinorhodin, which its concentration was increased by adding 0.1% methyl jasmonate.

Zebrafish (*Danio rerio*) larvae used in these experiments were obtained by mating wild-type AB/TL adults according to established protocols (zfin.org), with the approval of the local animal welfare committee (DEC) of Leiden University (License # 10612), and in accordance with the EU Animal Protective Directive 2010/63/EU. All larvae were 4 or 5 days post fertilization and before the feeding stage and thus exempt for the EU Animal Protective Directive 2010/63/EU. Eggs were collected immediately after mating and were maintained at 28°C in artificial fresh water (60 mg/L Instant Ocean) until use.

Radishes were obtained from the local market within a few days of processing. The tips of the main root were used for sample testing.

Glass needles

Two types of glass needles were tested for use in obtaining samples. In our initial attempt we used borosilicate glass capillary tubes that are routinely used to create microinjection needles. In this case we used borosilicate glass capillaries GC100F-10; 1.0 mm outer diameter, 0.58 mm inner diameter (Harvard Apparatus, Kent, United Kingdom). The tubes were loaded onto a Flaming/Brown Micropipette Puller (Model P-97, Sutter Instrument Co., USA) with settings of heat = 50, EL = 40, and time = 15. These settings reliably produced needles with an outer diameter of approximately 200 μm and an inner diameter of 180 μm . Two needles were produced from each event. Subsequently, the tips were trimmed using a scalpel or fine tweezers (Fig. 2A). The resulting needles were then used on two types of material: 1.2% agarose plates and zebrafish larvae in two different sites: tail or gut.

The second type of needle did not require pulling to achieve desired inner diameters. In this case, BGCT 0.1 borosilicate capillary tubes were purchased (Capillary Tube Supplies Ltd., Cornwall, United Kingdom). These needles had an outer diameter of 0.1mm and wall thickness of 0.01mm. In this case we developed attachments that allowed for easy handling and targeting of the needles (Fig. 2B-E). The glass needle is attached to a handle (Fig. 3C), which could then be used to manipulate the needle during the polishing step (Fig. 2D) and the sample targeting and collection step (Fig. 2E). Once the needles were polished to sharpen the tip, they were tested on agar plates of various concentrations.

3D printed needles

As an alternative to glass needles, we decided to 3D print needles to our desired specification to gain increased precision and reproducibility. The needles were 3D printed using the Nanoscribe Photonic Professional GT 3D printer (Nanoscribe GmbH & Co. KG, Karlsruhe, Germany) and photo activatable resin. The needle design went through several iterations, each being tested using agar plates of various concentrations. Once an ideal design was identified, additional needles were printed and tested on various biological samples. Success was defined as the ability to retrieve a core sample from the material, with little visual evidence of significant distortions.

For the final testing of the needle design, the 3D printed needles were glued to a 200 μl pipette tip containing a pin (Fig. 4D, S1B). The pipette tip was then attached to a spring loaded injection device (Fig. S1A, S1B), which was mounted to a movable, mechanical arm that was magnetically anchored to the table. The needle was positioned approximately perpendicularly to the agar pad containing sample. Using a dissecting scope, the sample was aligned with the needle, and then the needle

was injected approximately 3mm into the sample. The agar plate was then moved away from the needle and the needle was transferred to the HPF for the freezing protocol.

High pressure freezing

Sample isolation was immediately followed by HPF using the Leica EM ICE (Leica Microsystems GmbH, Austria). Sample-containing needles were separated from its base at the tripartite junction (arrow, Fig. 2, S1C) and then loaded into the 200 μm deep side of a 3 mm 'type A' copper carrier prefilled with 1-hexadecene. An additional drop of 1-hexadecene was added to the μm deep side of a second 'type A' carrier and then combined with the sample containing carrier (the resulting total height inside the carrier was 300 μm). The carrier was then inserted into the carrier holder and automatically processed through the ICE. In some cases, a grid was inserted in between the sample and top carrier in an effort to freeze the sample directly to the grid. Frozen samples were retrieved and stored in a grid box liquid nitrogen until further processing (Fig. S1D).

For samples obtained without the needle, the samples were trimmed with a scalpel, inserted into the 200 μm deep side of a 3 mm 'type A' carrier, filled with 10% Ficoll, topped with a Quantifoil R2/2, 200 mesh copper grid, followed by the flat side of a 'type B' 3 mm carrier. For the plant root, the root sample was directly frozen with the Leica EM ICE using a similar set as the needle. For the zebrafish larvae, the sample was high pressure frozen with a Baltec HPM010.

Sample thinning

Frozen samples were removed from the carriers under liquid nitrogen or in liquid nitrogen vapor. Samples were either frozen directly on grids or mounted to a grid prior to thinning using a cryo-glue (3:2, 2-propanol:100% ethanol). Initial thinning occurred using the Leica EM UC7 mounted with the Leica EM FC7 cryo-chamber and equipped with an EM Crion antistatic device (Leica Microsystems). Trimming of the samples occurred at -160°C using a cryo-Trim 45 knife (Diatome). Fine sectioning occurred using the cryo immuno diamond knife (Diatome). Trimmed samples were transferred to the Aquilos cryo-FIB SEM (Thermo Fisher Scientific (TFS), Waltham, MA, USA). The cryo-FIB SEM provided a general impression of the trimming quality and suitability for subsequent milling with the FIB.

Results

Zebrafish larvae processed through the traditional workflow

Our initial test of LSV preparation was done by directly freezing and milling of 5 dpf zebrafish larvae. Here, the tail and head were trimmed immediately prior to HPF so that it fit into the carrier, and an EM support grid was placed between the sample and the flat side of the carrier. After high pressure freezing, the sample naturally dislodged from the carrier sandwich and remained attached to the grid (Fig. 2). The sample-containing grid was clipped and evaluated using the Aquilos cryo-FIB SEM. The larva was found to be attached the grid (Fig. 2A-B). Rough milling was performed (blue circle in Fig. 2A), however, after several hours it became clear the sample would require extensive milling over several days using Aquilos to be suitable for cryo-ET (Fig. 2C, blue asterisk). After storage of the sample, we found the tissue had dislodged when the sample was loaded again into the Aquilos (Fig. 2D), ending the milling attempt. Based on this experience, we decided to explore additional options for thinning of the sample before and after it was frozen, leading us to the testing of a biopsy needle.

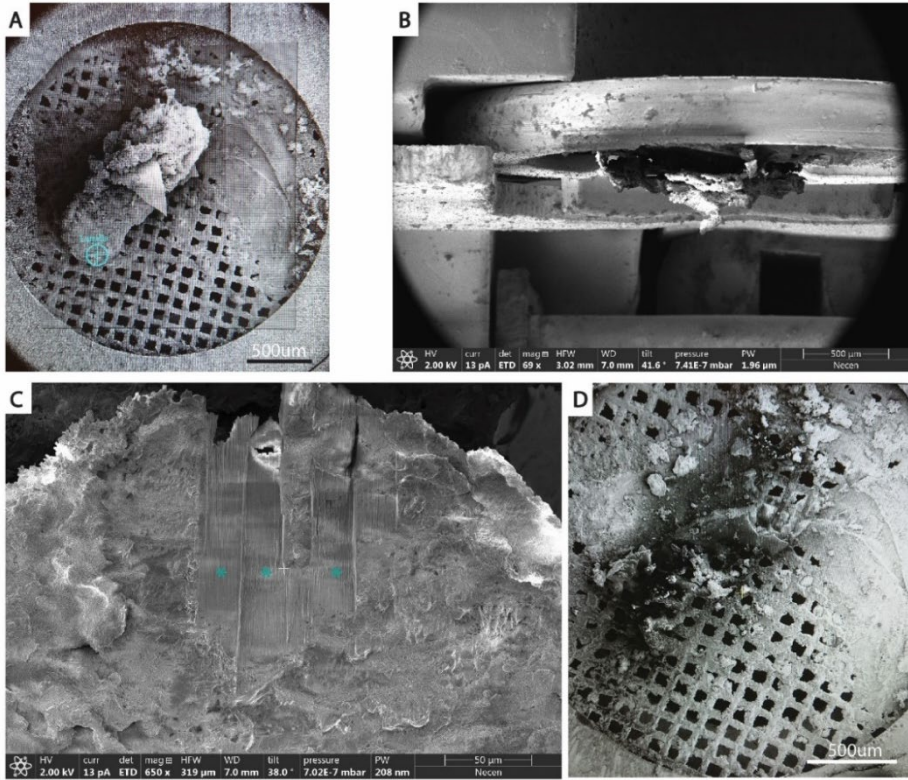


Figure 2. Overview of milling attempt of 5dpf zebrafish larvae. The trimmed zebrafish larva was trimmed and high pressure frozen directly on a grid. Upon visualization with the cryo-FIB SEM, the tissue appeared attached to the grid (A & B). FIB milling was attempted (A, blue circle is site of milling; C, blue asterisks) on the site noted in A and magnified in C. Following milling the sample was stored until the next milling session, which demonstrated a lack of tissue on the grid (D).

Glass needles

We next attempted sample extraction utilizing glass needles that had been pulled to specific inner diameter of approximately 100-200 μm . The needles proved to be too fragile and tips were too jagged and brittle to obtain an intact sample (Fig. 3A). In addition, during sample extraction it became clear that the needles were insufficiently sharp to puncture tissue with precision, especially in places where the sample was soft and pliable.

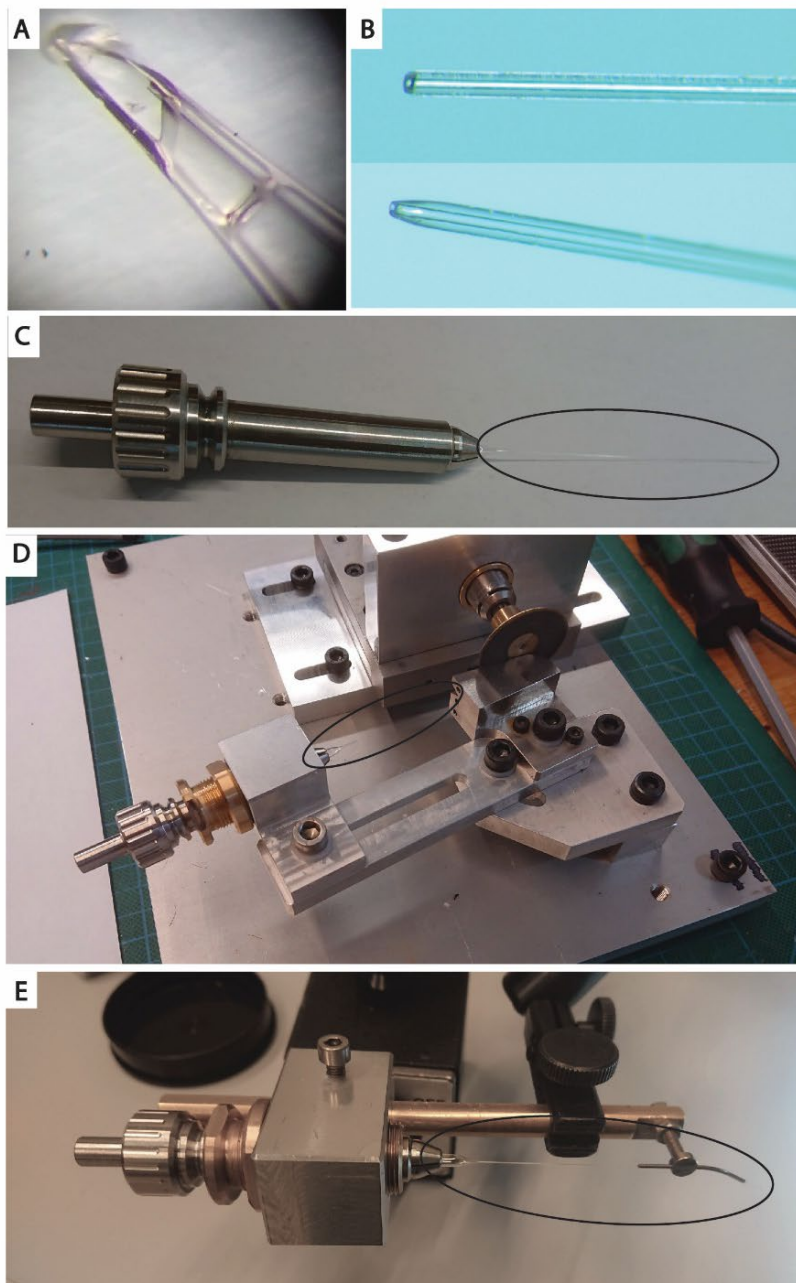


Figure 3. Example of glass needles and tools used to manipulate the needle. A. A representative image of a pulled glass needle following an attempt to extract a sample from an agar plate. B. Alternative needle design that required polishing of the edge rather than pulling of the needle. Due to the size and flexibility of the needle (black oval), tools were created to help with the handling (C), polishing (D), and targeting (E).

In an effort to increase consistency between the needles, we purchased glass capillary tubes with a specific inner and outer diameter, and then polished the tips to form a sharp point (Fig. 3B, top: unpolished, bottom: polished). In addition, we developed several tools used for handling of these needles, which improved our ability to move the needles between processing stages and sample extraction (Fig. 3C-E). In this case, we only tested the needles on agar plates of various concentrations. The needles continued to be too blunt and too flexible for suitable sample extraction, thus we explored alternative methods for needle production.

3D printed needles

After several unsuccessful attempts with the glass needles, we next explored the option of 3D printing needles to exact specifications. Most commercially available 3D printers do not have the ability to print accurately at the micron scale. Therefore, we used a specialized instrument that was available through our fine-mechanics department and that is capable to 3D print such items. In our case, we utilized the Nanoscribe Photonic Professional 3D printer, which uses two-photon technology to polymerize resin in a specific pattern. We designed and printed several versions of needles, keeping in mind the need for a sharp end that could help with the targeting and the incision. A common design feature included a three-prong tip with a thickness of 20 μm that was used for targeting of the needle at the site of injection. The needle was 1.65 mm in length with an inner diameter of 140 μm (size varied depending on the iteration but remained close to this diameter). An important component of the needle was the tripartite slits at the base of the needle (Fig. 4B arrow). These allowed any air pressure build up release when the sample enters the needle and prevents the sample from slipping out during retraction. The slits also provided a break point for the needle: once the sample was in the needle, it could be broken off and directly transferred to the sample carrier for subsequent high pressure freezing. Initial testing of this design achieved a core from 1.2% agarose plate (Fig. 4C, blue arrow highlighting the end of the sample). We next attempted to sample from a *Streptomyces coelicolor* colony, proved successful (Fig. 4D, arrow).

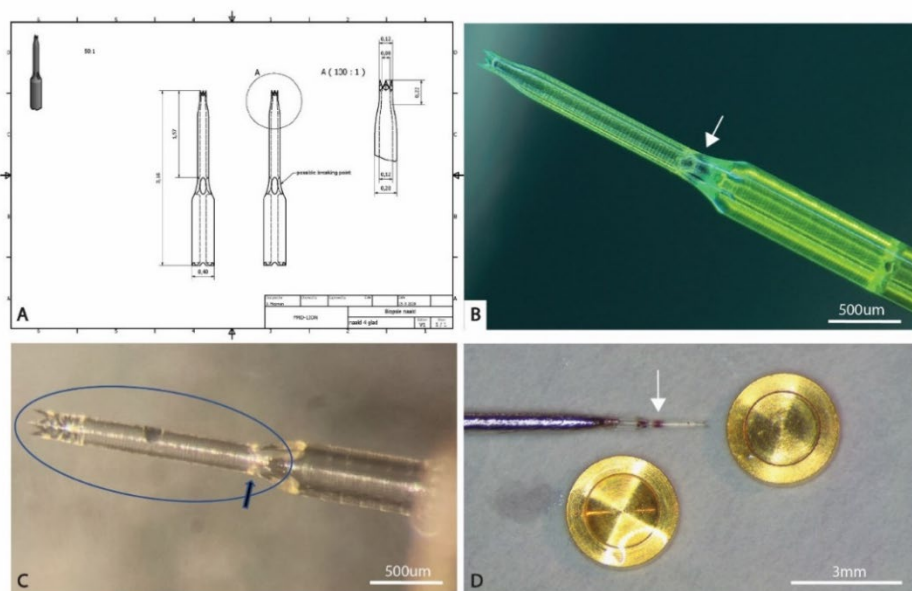


Figure 4. Overview of needle design and testing. A. Representative design of a 3D printed needle. B. Actual printed needle. The green color is due to autofluorescence of the resin. C. Proof of principle demonstrating the ability of the needle used to obtain a core from an agar plate. D. A mounted needle was used to obtain a core of a *Streptomyces coelicolor* colony from an agar plate. For reference, the two 3 mm carriers that will be used for HPF are located beside the sample filled needle.

High pressure freezing of sample filled needles

Prior to loading the sample-filled needle, the carrier is filled with a cryoprotectant to support the formation of vitrified ice. We tried various combinations of carriers and settled on the following assembly as the most optimal for the high-pressure freezing step: We placed the filled needle into a 200 μm deep side of a 'type A' carrier and sandwiched it with another cryoprotectant-filled 100 μm deep 'type A' carrier (Fig. 4D). The sandwich is then inserted into the high-pressure freezer, triggering the freezing process. We also tested a range of typically used cryoprotectants, such as 10% and 30% Ficoll and 1-hexadecene. 1-Hexadecene proved to be the most ideal cryoprotectant for our setup as it allowed for reasonable removal of the needle from the carrier without significant force. In addition to the cryoprotectant, we also coated our carriers in 1% soy lecithin dissolved in chloroform, which has been shown to ease the separation of the carrier sandwich and in releasing the sample from the carrier cavity. Once the frozen needle was removed, it was stored in a grid box until further processing.

Mounting and thinning of the sample

Following HPF, our intention was to directly mount the recovered needles to a cryo-EM support grid. This was done using the FC7 cryo-chamber of the ultramicrotome, cooled to -160°C . The grid box containing needles were transferred to the cooled chamber and allowed to acclimate while a grid was attached to the manipulator. When ready, the grid was placed in the chamber, cryo-glue (100% ethane: 2-Propanol in a 2:3 ratio) was dabbed onto the grid, and the needle was immediately transferred to the grid and attached to the glue. However, this process proved more challenging than expected. The needles themselves were frequently dropped in the chamber and unrecoverable. In addition, we found that the cryo-glue solidified too quickly, preventing the needle from attaching properly to the grid.

For samples that were frozen directly onto a grid, the grid had to be mounted before sectioning could begin. One sample, the radish root tip, made it to this step in the process (Fig. 5A). A 'type B' carrier was mounted to the chuck, with the 300 μm deep side facing the user. Cryo-glue was applied to the edges of the carrier and then the grid was quickly attached with a little pressure to create the bond (Fig. 5B). At this point the sample was allowed to equilibrate for several minutes before sectioning began. We successfully trimmed the sample using the cryo-Trim 45 diamond knife (note the reflective flat surface in Fig. 5B). Once trimming was complete, a cooled scalpel blade was used to detach the grid from the carrier, and transferred to a grid box for further processing in the cryo-FIB SEM. Imaging with the cryo-FIB SEM demonstrated that it was possible to successfully transfer the grid from the cryo-ultramicrotome, and that the sample was successfully trimmed and appeared structurally sound (Fig. 5C).

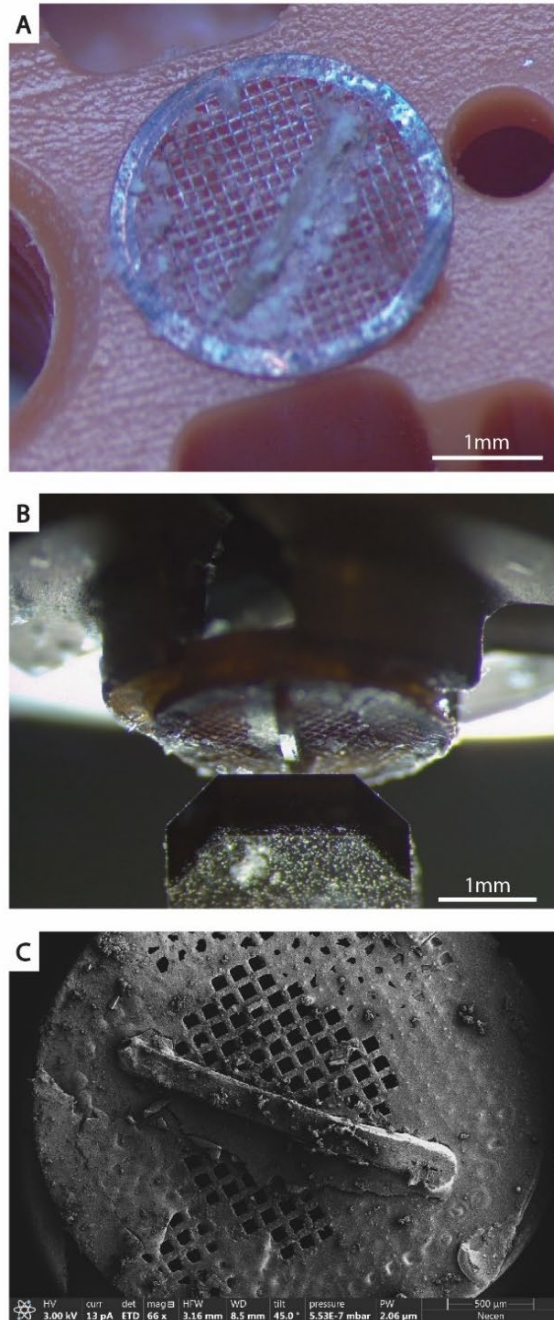


Figure 5. A radish root tip was isolated and HPF frozen directly on a grid (A). The sample-containing grid was then transferred to the cryo-ultramicrotome for sample thinning using a diamond knife (B). The sample was then transferred to the cryo-FIB SEM for inspection of sample quality following cutting.

Discussion

In this study we demonstrate the first few steps of a proposed LVS pipeline that is designed to prepare multicellular samples for cryo-ET. Our first attempts of sample recovery with glass needles were unsuccessful, demonstrating that a lack of a sharp edge and extreme flexibility were limiting factors. We could overcome these issues by using 3D printed needles. These needles could then be successfully used for sample collection and high pressure freezing of the sample. Using the 3D printed needle, we were successful in obtaining a core sample from a bacterial colony of *S. coelicolor*. When further analyzed, this type of sample could provide significant structural details about the aerial hyphae layer as well as the transition into the substrate. However, it remains to be demonstrated that the sample-filled needles can be taken through the remaining steps of the proposed workflow: sample thinning with the cryo-ultramicrotome and the cryo-FIB SEM, and ultimately imaging with the cryo-EM.

We were also able to directly freeze a sample on a grid using high pressure freezing. This protocol was successfully applied using a radish root tip: upon collection of the sample, the root tip was frozen directly on the grid, and subsequently trimmed using cryo-ultramicrotomy. This is an important step because it eliminates the need to mount the frozen sample to the grid before trimming. For the 3D printed needles, this processing step has proved challenging for us due to the size of the needle and the glue used to attach the needle to the grid. However, we believe additional practice in handling and transfer will allow this step to succeed. The root tip sample also demonstrated that following trimming, the sample can be successfully transferred to the cryo-FIB SEM for imaging and trimming. Again, this proof on concept supports our intended workflow. It is important to note that we have not completely processed a sample through the entire workflow. Instead, we have been able to successfully complete individual steps, which when combined with the right sample, we believe will prove to be a valuable tool for routine LVS processing.

Despite the challenges of LVS preparation, we see our workflow as the next step in the evolution of sample processing for cryo-ET. We combine several different methods, that are usually intended to be used individually or for different techniques, into a single workflow. As a way to make the LVS more manageable, we designed and implemented a 3D printed needle for obtaining biopsies from different samples. Up to this point, we have twelve versions of the needle that have been, or are being tested in different types of samples. We believe that with some trial and error, and intentional design, we will be able to apply the biopsy needle to

multiple sample types. The idea to use biopsy needles for sample collection is not a new one, as it is regularly used in the medical diagnostics. In addition, several successful attempts of creating a needle for sample preparation for EM were previously published (136, 137) that demonstrate that it is possible. Our study benefits from technological improvements, especially with 3D printing, which allows us to quickly redesign and implement changes that could be tissue specific. In addition, we have not reached the limits of the 3D printer, thus if we can get the current designs to work, we can reduce the size of the inner diameter of the needle which in turn reduces the amount of trimming necessary and would therefore ease the workflow.

The ultimate goal of this project is to better understand how bacteria interact with their host. Using the techniques developed here, we aim to structurally examine three different model systems: *V. cholerae* infected zebrafish larvae, endophytic bacteria found in plate roots, and the symbiotic relationship of *V. fischeri* with the Hawaiian bobtail squid (58, 138, 139). Each of these provides a unique opportunity to better understand how the bacteria's morphology and molecular machines impact their ability to interact with their respective hosts. For example, when *V. cholerae* colonizes a host, it uses a number of molecular machines in this effort: the F6 chemotaxis array to sense its environment, the flagella to move towards its desired niche, and the mannose-sensitive hemagglutinin (MSHA) pili for attachment to the epithelial cell surface (58). Using our LVS workflow, we could then use a natural host model of *V. cholerae* infection, the laboratory zebrafish, to better understand these steps in colonization and dissemination back into the environment (66). This model is especially interesting because other unknown factors might play a role in colonization. Being able to visual the bacteria:epithelial cell interaction could provide new details about molecular machines that are involved in this process.

The next big advancements in cryo-ET lie in large volume sample processing. In the past several years, different commercial tools have been developed, such as the cryo-FIB SEM and the cryo-lift out device, which are beginning to allow researchers to shed light on complex, multicellular systems. However, opportunities for new technology such as our biopsy needles still exist. With this research we provide proof of principle that using micrometer length needles is a unique tool for obtaining cryo-ET suitable samples from LVS.

Acknowledgements

We are grateful for the assistance of Jan de Weert and Frederic Leroux for their training and assistance throughout the freezing and trimming workflow. We are also grateful to Carmen Lopez Inglesias and prof. dr. Peter Peters of the Maastricht Multimodal Molecular Imaging institute, M4i at Maastricht University for their assistance in our initial attempts to freeze the zebrafish larvae directly on a grid.

Supplementary Material

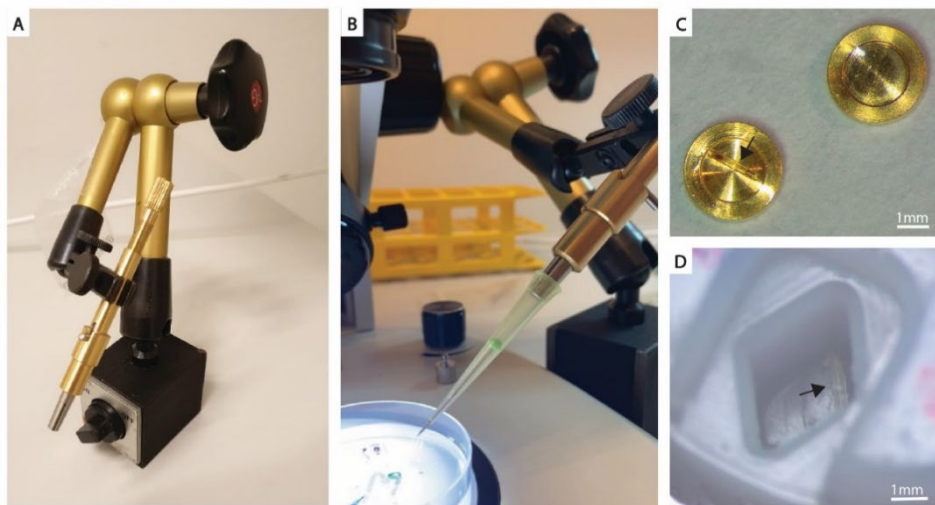


Figure S1. Overview of the sample acquisition process. A spring-loaded injector was attached to a mechanical arm (A) and the pipette tip with a needle was attached to the injector (B). Following sample retrieval, the needle was separation from the pipette tip, loaded into the 200 μm cavity of a 3 mm type A carrier containing 1-hexadecene (C, black arrow), and a second carrier was placed on top to form a sandwich. The sandwich is then high pressure frozen, the sample filled needle is recovered under liquid nitrogen in a grid box until further processing (D, black arrow).

CHAPTER 7

General Discussion & Summary

General Discussion and Summary

To understand the biological world around us, we need to investigate it across multiple scales. While some of it can be directly observed with our own eyes, such as large organisms interacting with their environments, most of the fundamental processes enabling life occur inside individual cells and tissues and thus are hidden from plain sight. To gain insight into how cells work at the (macro)molecular scale, we rely on specialized tools including model systems and a wide range of light and electron microscopes.

Laboratory animal models, such as the zebrafish (*Danio rerio*) system, have allowed us to gain a better understanding of a variety of fundamental processes. This has been possible due to the ability to manipulate the organism genetically and to directly observe the resulting effects on the larvae using fluorescence microscopy (140). However, many cellular processes and interactions between cells and invading pathogens occur on an even smaller scale and cannot be understood by using light microscopy techniques alone.

To better understand cells and how they interact with their environment at the micro- and nanoscale level, we must zoom in using other, more powerful microscopy methods such as cryogenic electron microscopy (cryo-EM)(75). For questions at the cellular level and involving heterogeneous samples, cryogenic electron tomography (cryo-ET) has become a tool of choice because it can peer directly into samples at near-native preservation. For example, we can examine whole bacteria (**Chapter 4**) and analyze different macromolecular machines such as their chemotaxis arrays, flagella, or pili (**Chapters 2, 4, 5**). For looking at isolated protein complexes in purified, homogenous samples, we can apply another cryo-EM method called single particle analysis (SPA). This technique enables us to visualize individual proteins or protein structures with nanometer resolution. In this thesis, I used this method to examine a bacterial virus, the ICP1 bacteriophage, and a human protein, apoferritin (**Chapters 3, 5**).

The investigation of cells, viruses, or protein complexes with cryo-EM requires specialized sample preparation techniques. For samples less than 5-10 μm in thickness, we can use plunge freezing to embed the sample in vitreous ice (**Chapters 3, 4, 5**). Samples with greater thicknesses, such as larger cells, tissues or microbial biofilms, require high pressure freezing to avoid artefacts caused by ice crystal formation and subsequent sample thinning (**Chapter 6**)(5, 129). In this thesis, I developed new tools and workflows based on these methods to gain new

insight into the ultrastructure of the pathogen *Vibrio cholerae* and how it adapts to changing environments during the infection of a natural host, the zebrafish.

In the past two decades we have gained much insight into the ultrastructure of microbes. Much of these insights into bacterial ultrastructure have been gained using cryo-ET (75, 141). In **chapter 2**, I review our current knowledge on the cellular ultrastructure and how specific macromolecular machines enable the cells to interact productively with their environments. First, I outline how the different structures of the cell envelope act as boundaries between the cell's inner contents and its external environment. I then link these to cell shape and discuss the process of cell division. Finally, I discuss structures that directly interact with the external environment, such as the various appendages and secretion systems.

Advances in cryo-EM specimen preparation

While we have gained a lot of insight into structure and function of bacterial cells in laboratory monocultures, less is known about bacterial ultrastructure in natural environments, such as when bacteria are interacting with a host during infection. However, this poses a major practical challenge: the biological experiments for host infection must be performed in specialized laboratories that often lack the necessary equipment for cryo-EM specimen preparation. Commercially available machines are cost prohibitive for a non-EM focused lab and require dedicated space and expertise for their operation. Therefore, I created a device that could simply and affordably prepare samples for cryo-EM that could be easily used in any laboratory. I designed the device to be suitable for travel (lightweight and compact design for easy to transport), as well as capable of producing high quality samples for both cryo-ET and SPA. Only some generally available accessory components need to be acquired onsite, such as liquid nitrogen and a cryogen for the vitrification (generally pure ethane or ethane propane mixture). After testing and optimizing the device on a variety of samples in our own laboratory, I used it to prepare samples in our collaborators' laboratory at Wayne State University (Detroit, MI USA). This device was pivotal in collecting data that contributed to **chapter 4**. In addition to my own experiments that relied on the device, it will be directly applicable to labs that have very specialized animal housing or other set-ups for generating biological samples. For example, the device would be useful to study bacteria that rely on specialized anaerobic environments or pathogenic organisms requiring stringent safety measures.

Vibrio cholerae interaction with a natural host

In my thesis, I focused on the ultrastructural changes of the bacterium *Vibrio cholerae*, which must rapidly adjust to changing environments during its infection

cycle. The pandemic-related strains are the cause of cholera, a severe diarrheal disease that affects humans and animal hosts (51, 52, 57, 66, 142, 143). The bacterium primarily lives in environmental water bodies including fresh-, brackish- and salt-water, where it exists as free floating bacteria, or in multicellular biofilms attached various surfaces such as copepods (57). When a human ingests contaminated water, the bacterium quickly transitions through the hostile environment of the stomach to the small intestine where colonization occurs (Fig. 1.2; Peterson & Gellings, 2018; Singh & Barnard, 2016). Within hours of ingestion, dissemination back into the environment occurs in the form of diarrhea, which typically restarts the infection cycle (58).

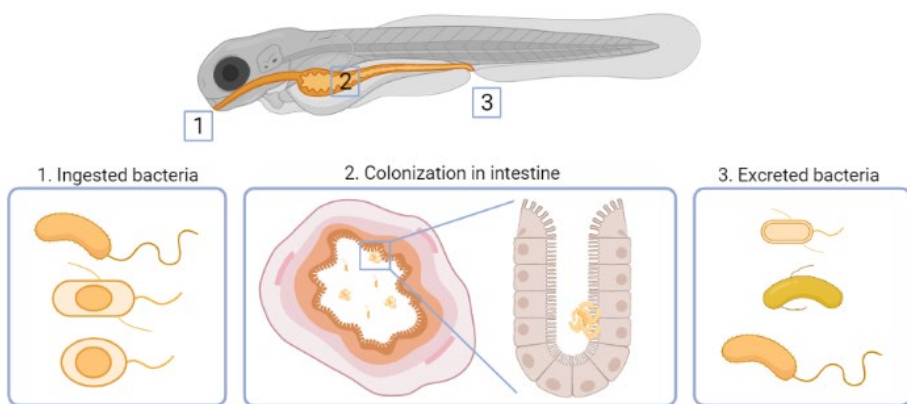


Figure 1. Overview of *V. cholerae* infection cycle in the zebrafish larvae characterized by cryo-EM and SBF SEM (Chapter 4). Bacteria in the environment (1) are ingested naturally by the zebrafish larvae leading to the colonization of the intestine (2) and eventual dissemination back into the environment (3). Created in Biorender.com.

Here, I wanted to gain a better understanding of how the bacterial ultrastructure changes during the infection cycle. To do this, I used a recently described natural host of *V. cholerae*, the laboratory model organism of the zebrafish (66). Our study in **chapter four** first describes the morphology and molecular machines of cells that are transitioned from the laboratory environment of a nutrient rich culture media (LB) into a controlled nutrient poor freshwater environment (AFW). I paid specific attention to cell shape, and the molecular machines that had previously been shown to be involved in colonization: the F6 chemotaxis array, the flagella, and the pili (53, 57, 58, 63). I found that while there are significant changes in cell shape, including a significant increase in the fraction of cells with a large periplasmic space (dehiscence), the expression of the molecular machines changes only slightly (Fig. 1.1). Next, I was interested in understanding the colonization dynamics within the

zebrafish intestine. I infected zebrafish larvae with *V. cholerae*, and then used serial block face scanning electron microscopy (SBF SEM) to characterize sites of colonization and the cell shape. I found that the bacterium typically exists in small microcolonies that can be found free floating in the lumen and associated with the microvilli (Fig. 1.2). Segmentation of individual cells revealed a typical vibrioid morphology, as expected, and measurements of cell lengths were comparable to cells found in a nutrient rich environment. Lastly, I was interested in the cells that were excreted back into the environment from *V. cholerae*-infected zebrafish, both from the adult fish as well as the larvae. To do this, I travelled to Wayne State University with the manual plunger device produced in **chapter three**, and working with the local experts, infected adult fish and larvae with *V. cholerae* and collected the bacteria that were excreted over a 24 h period. Using cryo-ET, I examined the same features as the cells in LB and AFW and found significant differences when comparing their morphology. The cell shape was either typical vibrioid or ovoid in structure, and much less occurrences of dehiscence were seen in these cells (Fig. 1.3). From this research, I conclude that the transition through the zebrafish gut primes the bacteria for release back into a nutrient poor environment, likely aiding the bacteria in colonizing another host and continuing its infection cycle. In addition, I also noted that storage granules were present in the cells that colonized the zebrafish larvae intestine and the excreted bacteria, which has also been shown to support a successful transition from the host back into the environment (82). Lastly, these finding support the use of the zebrafish model for understanding colonization and dissemination factors.

Taken together, this piece of work is the first time the detailed, subcellular, ultrastructural changes of a pathogen have been investigated throughout the entire infection cycle. It provides further insight into why cells found in stool samples or cells in biofilms as used in other studies, are hyperinfectious, thus requiring a less infectious dose than cells that might be found in freshwater alone (80, 81).

Ultraviolet light inactivation of pathogens for cryo-EM

Working with a pathogen such as *V. cholerae* (biosafety level II, BSL-II) can be quite challenging as it requires strict adherence to biosafety procedures and containment measures. At the onset of this thesis, the local microscopy cryo-EM center, the Netherlands Centre for Electron Nanoscopy (NeCEN), was not certified to image BSL-II pathogens. While the BSL-II certification was obtained for NeCEN in the course of this thesis, it demonstrated that access to cryo-EM can be limited for BSL-II or higher samples. Therefore, I was interested in developing methods for reducing the activity of a microorganism to facilitate easy access to cryo-EM facilities that are not certified for higher biosafety level samples. In this case, I used a well-known

disinfectant, ultraviolet-C (UVC, wavelengths 185-280nm) irradiation, to inactivate cryo-EM samples of two types of microorganisms, *V. cholerae* and its associated bacteriophage, ICP1 (a bacterial virus). While much is known about how UVC affects the activity of microorganisms at ambient temperatures, what the impact of UVC light on ultrastructure and viability at cryogenic temperatures was still unknown (12, 96, 122, 145). Here, I took a step-by-step approach by using cryo-ET and SPA methods to determine both viability after UVC treatment and to investigate if resolution was adversely affected using the bacterial and viral samples (**Chapter 5**). A vitrified grid containing *V. cholerae* was inactivated completely (as quantified by colony forming units) in just 30 s of UVC irradiation. Importantly, there was no visible damage to the cells, and subtomogram averaging of its F6 chemotaxis array achieved resolutions ranging from 22-26 Å, which is comparable to data collected from cells that were not UVC irradiated. For the ICP1 bacteriophage, treatment of the vitrified sample with UVC for 60 s on the front of the grid and 30 s on the back resulted in a 99.9999% reduction in phage activity. Using SPA, I achieved cryo-EM structures of 5.1 Å and 6 Å for the UVC-treated and untreated DNA-containing capsid, respectively. As with the bacterial sample, visual inspection of the phage did not show any obvious damage, and the achieved resolution was well within expectations for the number of phage particles used in the analysis. The resolution was actually slightly higher for the UVC treated sample. This can be partially explained by having more data for the averaging and is consistent with the UVC treatment not causing any detectable damage despite rendering the samples harmless.

Because we found no obvious damage of the structures at resolutions up to 5 Å, I finally aimed to determine the structural effects of the UVC treatment using apoferritin (ApoF), a sample that is often used for high-resolution structural testing. I exposed the purified ApoF to UVC using the same conditions as the ICP1 phage sample and used SPA to determine the resolution. Similar to other published apoferritin structures, I achieved a resolution of 2.1 Å. A detailed comparison with other untreated structures did not show any noticeable changes. Ultimately this study demonstrated that UVC is a viable method for inactivating potentially dangerous cryogenic samples, and that there is no detectable impact on the structural information of proteins and protein complexes that can be achieved from this method up to resolutions of 2 Å. This is an important contribution to the field because it expands the toolbox for sample preparation and could increase access to the microscope infrastructure by reducing the pathogen's safety level to one that is acceptable by the facility.

However, questions remain about what the actual impact of the UVC is having on the sample, and additional experiments would need to be done to show how UVC is inactivating the vitrified samples. At room temperature, UVC is known to damage DNA by causing the formation pyrimidine dimers, but the extent of this damage is not known at cryogenic temperatures (12, 96). Presumably the damage caused by UVC irradiation would be randomly dispersed within the sample. However, this randomness would pose a challenge with the averaging required to improve the signal-to-noise ratio in cryo-EM, as any small defects are averaged out, making them effectively invisible within the dataset. While this method is useful for reducing the biosafety level without negatively impacting the final result, characterizing the precise damage would be a challenge.

Pushing the boundaries of sample thickness for cryo-EM

As noted in **chapter four**, I was interested in understanding the colonization dynamics of the *V. cholerae* within the zebrafish host. To do this, we used SBF SEM, which, while capable of providing important information about colonization, does not achieve the resolution required to see most of the molecular machines that are involved in colonization. In contrast, cryo-ET is capable of seeing these complexes at a near-native state. However, this method is typically applied to individual or small groups of cells because the technology is currently limited by sample thickness. For cryo-ET, ideal sample thicknesses are approximately 200 nm, though depending on the wavelength of the electron beam, can be greater than 400 nm (3). Ultimately, what this means is that any samples that are larger than 400 nm in thickness require an additional processing step for sample thinning to ensure the highest possible resolution. The potential for gaining new insights has been demonstrated by large volume samples, including new insights into septal junctions in cyanobacteria, pore structures important to RNA replication in a coronavirus infected cell line, and a structural understanding of cytosolic 80S ribosomes in a *Caenorhabditis elegans* worm (8, 88, 146). Thus, the development of new methods for gaining insight into even thicker samples would enable the application of this method to other biological disciplines, such as cancer research where studying the intact tumor tissue is critical, or intracellular pathogens.

The current methods for cryo-EM of thin samples utilizes plunge freezing, and thus can go directly into the cryo-FIB SEM to create lamella for imaging using cryo-ET. Alternatively, thicker samples that are high pressure frozen use the cryo-FIB SEM to create trenches at specific sites in the large volume, and then a cooled micro gripper to remove the remaining tissue (less than 20 μm in width and 5 μm in depth), which can then be thinned using the ion beam to create lamella. However, both techniques require extensive training and time and offer relatively low

throughput. Thus, I set out to improve this process, especially when very thick samples are involved.

In **chapter 6**, I describe an updated workflow for the processing of extremely thick samples such as tissues with a thickness greater than 50 μm and without the use of a micro-gripper. These samples require high pressure freezing, which can vitrify a sample up to 250 μm (5, 129). After vitrification, additional thinning steps must be developed to make these samples amenable to cryo-EM analysis. Here, I applied available tools and techniques such as cryo-ultramicrotomy and cryo-FIB SEM (7, 9, 147) on samples extracted with a novel type of 3D printed biopsy needle. The needle is critical to obviating the need for a micro-gripper. In our case, we succeeded in obtaining an initial sample from a *Streptomyces coelicolor* colony. In the future, we aim to optimize the current design to be suitable for tissue extraction from animal and plant systems. This will be done by further iterations of the needle design that inherently allows rapid changes, printing, and testing.

With the bacterial sample we were able to high pressure freeze the sample, retrieve it from the carrier, and store the sample for further processing. This became quite routine for agar-based samples, and testing is ongoing with a variety of different samples (bacterial colonies, plant roots, zebrafish larvae, etc.). So far, we have tested eleven different versions of the needle design. In conjunction with the needle development, we were also successful in freezing a plant root sample directly on a grid, trimming the sample with a cryo-ultramicrotome, and subsequently imaging within the cryo-FIB SEM. By freezing the root directly on a grid, we remove one step in the processing pipeline, which suggests that some additional focus should be given to freezing a needle directly on a grid. This project is still in progress, and each successful step in the process brings us closer to being able to use cryo-ET on multicellular samples. Current methods do exist for examining large volume samples, but most rely on chemical fixation and dehydration or techniques that require specialized training (9, 128, 148, 149). These all introduce unavoidable artifacts that preclude examination of complexes at the molecular level.

Concluding remarks and outlook

Taken together, this dissertation uses a variety of sample preparation techniques for cryo-EM to better understand how *V. cholerae* is impacted by changes in the environment. I was able to demonstrate morphological changes in *V. cholerae* bacteria when they pass through the zebrafish gut, which likely aid the released bacteria in colonizing a new host (outlined in Fig. 1, **Chapter 4**). This information is important for understanding how bacteria adjust to a new host, and how this

interaction prepares the bacterium for life unassociated with the host. Improvements in the preparation of large volume samples for cryo-EM would greatly benefit this research area.

The technical developments in sample preparation and new knowledge could be applied to a number of up-and-coming biological systems including a better understanding of the microbiome and its role in disease, an example of microbiome disruption by *V. cholerae*, and the role of various molecular machines such as type 4 pili in the gut (150–153). Combined with other techniques, such as correlative light and electron microscopy for targeting of trimming efforts or *in vivo* click chemistry, it is possible to hone in on specific areas that answer biological questions. However, without addressing the challenges regarding the processing of large volume samples for cryo-EM, many of these systems can only be explored to a limited extent. Currently, cryo-EM of large volume samples lags behind compared to other techniques such as light microscopy that offers much higher throughput and better statistics for comparable resource investment. Instead, my hope is that once our workflow is optimized, it will be possible to automate it and quickly adapt it to new biological questions, especially without the need to have a very specialized skill set.

With the continued development of new tools for sample processing, it will also be important to re-examine how we use our current tools and innovate in new methods. For instance, our current method of high pressure freezing was established in the 1980s and little has changed in its design and use. Other groups are focusing on different ways of vitrifying samples, such as constant volume freezing or microfluidic vitrification (154, 155), though neither technique has become routine. Besides the freezing step, advances in the cryo-FIB SEM instrumentation could also benefit the large volume workflow. Efforts are being made to replace the current gallium-based FIB with an oxygen plasma source, which would improve the beams milling ability to larger volume samples without a significant loss in precision (156). Additional efforts are also being made in integrating a fluorescent light microscope directly into the cryo-FIB SEM. In addition to reducing transfer steps between instruments, this advance would also allow better targeting during the sample thinning process (157, 158). Taken together, these types of advances would simplify the workflow by removing transfer and thinning steps, thereby increasing access to these highly specialized sample preparation techniques. Once the tools are developed I can next focus on simplifying the techniques for the non-expert, thereby answering more biological questions that require high resolution information to better understand the biological world.

In summary, this thesis contributes to important developments in the field as cryo-EM, providing access to techniques that have traditionally been restricted to a limited number of well-equipped labs. With the creation of regional and national facilities that house the microscopes, new users are invited to prepare samples locally before engaging these facilities. In addition, for users who work with organisms that are considered BSL II or higher, I introduce a new tool for sample preparation that could allow these higher-level organisms to be brought down to levels acceptable for such facilities. Combining the UVC technique with the manual plunger significantly reduces the investment for preparing these samples and will yield tremendous insight into the *in vivo* organism. These techniques together with other emerging techniques in large volume sample preparation and new models of host pathogen interactions, offer an entirely new set of tools for exploring microbes and how they interact with their environments.

REFERENCES

REFERENCES

1. Dubochet, J., Adrian, M., Chang, J., Homo, J., Lepault, J., McDowell, A. W., and Schultz, P. (1988) Cryo-electron microscopy of vitrified specimens. *Q. Rev. Biophys.* **21**, 129–228
2. Turk, M., and Baumeister, W. (2020) The promise and the challenges of cryo-electron tomography. *FEBS Lett.* **594**, 3243–3261
3. Yonekura, K., Braunfeld, M. B., Maki-Yonekura, S., and Agard, D. A. (2006) Electron energy filtering significantly improves amplitude contrast of frozen-hydrated protein at 300 kV. *J. Struct. Biol.* **156**, 524–536
4. Tivol, W. F., Briegel, A., and Jensen, G. J. (2008) An improved cryogen for plunge freezing. *Microsc. Microanal.* **14**, 375–379
5. Moor, H. (1987) Theory and Practice of High Pressure Freezing. *Cryotech. Biol. Electron Microsc.* 10.1007/978-3-642-72815-0_8
6. Al-Amoudi, A., Chang, J. J., Leforestier, A., McDowell, A., Salamin, L. M., Norlén, L. P. O., Richter, K., Blanc, N. S., Studer, D., and Dubochet, J. (2004) Cryo-electron microscopy of vitreous sections. *EMBO J.* **23**, 3583–3588
7. Chlanda, P., and Sachse, M. (2014) Cryo-electron microscopy of vitreous sections. *Methods Mol. Biol.* **1117**, 193–214
8. Schaffer, M., Pfeffer, S., Mahamid, J., Kleindiek, S., Laugks, T., Albert, S., Engel, B. D., Rummel, A., Smith, A. J., Baumeister, W., and Plitzko, J. M. (2019) A cryo-FIB lift-out technique enables molecular-resolution cryo-ET within native *Caenorhabditis elegans* tissue. *Nat. Methods.* **16**, 757–762
9. Kuba, J., Mitchels, J., Hovorka, M., Erdmann, P., Berka, L., Kirmse, R., König, J., De Bock, J., Goetze, B., and Rigort, A. (2021) Advanced cryo-tomography workflow developments – correlative microscopy, milling automation and cryo-lift-out. *J. Microsc.* **281**, 112–124
10. Wanner, A. A., Genoud, C., and Friedrich, R. W. (2016) 3-dimensional electron microscopic imaging of the zebrafish olfactory bulb and dense reconstruction of neurons. *Sci. Data.* **3**, 1–15
11. Tsang, T. K., Bushong, E. A., Boassa, D., Hu, J., Romoli, B., Phan, S., Dulcis, D., Su, C.-Y., and Ellisman, M. H. (2018) High-quality ultrastructural preservation using cryofixation for 3D electron microscopy of genetically labeled tissues. *Elife.* **7**, e35524
12. Pattison, D. I., and Davies, M. J. (2006) Actions of ultraviolet light on cellular structures. in *Cancer: Cell Structures, Carcinogens and Genomic Instability* (Bignold, L. P. ed), pp. 131–157, Birkhäuser Verlag/Switzerland, 10.1007/3-7643-7378-4_6
13. Albers, S. V., and Meyer, B. H. (2011) The archaeal cell envelope. *Nat. Rev. Microbiol.* **9**, 414–426
14. Skennerton, C. T., Haroon, M. F., Briegel, A., Shi, J., Jensen, G. J., Tyson, G. W., and Orphan, V. J. (2016) Phylogenomic analysis of Candidatus “Izimaplasma” species: Free-living representatives from a Tendercutetes clade found in methane seeps. *ISME J.* **10**, 2679–2692
15. Gan, L., Chen, S., and Jensen, G. J. (2008) Molecular organization of Gram-negative peptidoglycan. *Proc. Natl. Acad. Sci.* **105**, 18953–18957
16. Bharat, T. A. M., Kureisaite-Ciziene, D., Hardy, G. G., Yu, E. W., Devant, J. M., Hagen, W. J. H., Brun, Y. V., Briggs, J. A. G., and Löwe, J. (2017) Structure of the hexagonal surface layer on *Caulobacter crescentus* cells. *Nat. Microbiol.* **2**, 1–6
17. Danilova, O. V., Suzina, N. E., Van De Kamp, J., Svenning, M. M., Bodrossy, L., and

- Dedysh, S. N. (2016) A new cell morphotype among methane oxidizers: A spiral-shaped obligately microaerophilic methanotroph from northern low-oxygen environments. *ISME J.* **10**, 2734–2743
18. Jiang, C., Brown, P. J. B., Ducret, A., and Brun, Y. V. (2014) Sequential evolution of bacterial morphology by co-option of a developmental regulator. *Nature*. **506**, 489–493
 19. Wanger, G., Onstott, T. C., and Southam, G. (2008) Stars of the terrestrial deep subsurface: A novel “star-shaped” bacterial morphotype from a South African platinum mine. *Geobiology*. **6**, 325–330
 20. Briegel, A., Ortega, D. R., Huang, A. N., Oikonomou, C. M., Gunsalus, R. P., and Jensen, G. J. (2015) Structural conservation of chemotaxis machinery across Archaea and Bacteria. *Environ. Microbiol. Rep.* **7**, 414–419
 21. Szwedziak, P., Wang, Q., Bharat, T. A. M., Tsim, M., and Löwe, J. (2014) Architecture of the ring formed by the tubulin homologue FtsZ in bacterial cell division. *Elife*. **3**, e04601
 22. Beeby, M., Ribardo, D. A., Brennan, C. A., Ruby, E. G., Jensen, G. J., and Hendrixson, D. R. (2016) Diverse high-torque bacterial flagellar motors assemble wider stator rings using a conserved protein scaffold. *Proc. Natl. Acad. Sci. U. S. A.* **113**, E2759
 23. Daum, B., Vonck, J., Bellack, A., Chaudhury, P., Reichelt, R., Albers, S. V., Rachel, R., and Kühlbrandt, W. (2017) Structure and in situ organisation of the pyrococcus furiosus archaeellum machinery. *Elife*. **6**, 1–21
 24. Briegel, A., and Jensen, G. (2017) Progress and Potential of Electron Cryotomography as Illustrated by Its Application to Bacterial Chemoreceptor Arrays. *Annu. Rev. Biophys.* **46**, 1–21
 25. Schrempf, H., Koebsch, I., Walter, S., Engelhardt, H., and Meschke, H. (2011) Extracellular Streptomyces vesicles: Amphorae for survival and defence. *Microb. Biotechnol.* **4**, 286–299
 26. Reichow, S. L., Korotkov, K. V., Hol, W. G. J. J., and Gonen, T. (2010) Structure of the cholera toxin secretion channel in its closed state. *Nat. Struct. Mol. Biol.* **17**, 1226–1232
 27. Nans, A., Kudryashev, M., Saibil, H. R., and Hayward, R. D. (2015) Structure of a bacterial type III secretion system in contact with a host membrane in situ. *Nat. Commun.* **6**, 10114
 28. Ghosal, D., Chang, Y.-W., Jeong, K. C., Vogel, J. P., and Jensen, G. J. (2016) Structure of the Legionella Dot/Icm type IV secretion system in situ by electron cryotomography. *EMBO Rep.* **10.1101/085977**
 29. Chang, Y.-W., Rettberg, L. A., and Jensen, G. J. (2017) In vivo structures of an intact type VI secretion system revealed by electron cryotomography. *EMBO Rep.* **10.1101/108233**
 30. Chang, Y.-W. W., Kjær, A., Ortega, D. R., Kovacicova, G., Sutherland, J. A., Rettberg, L. A., Taylor, R. K., and Jensen, G. J. (2017) Architecture of the Vibrio cholerae toxin-coregulated pilus machine revealed by electron cryotomography. *Nat. Microbiol.* **2**, 16269
 31. Perras, A. K., Daum, B., Ziegler, C., Takahashi, L. K., Ahmed, M., Wanner, G., Klingl, A., Leitinger, G., Kolb-Lenz, D., Gribaldo, S., Auerbach, A., Mora, M., Probst, A. J., Bellack, A., and Moissl-Eichinger, C. (2015) S-layers at second glance? Altiarchaeal grappling hooks (hami) resemble archaeal S-layer proteins in structure and

REFERENCES

- sequence. *Front. Microbiol.* 10.3389/fmicb.2015.00543
32. Adams, D. W., and Errington, J. (2009) Bacterial cell division: Assembly, maintenance and disassembly of the Z ring. *Nat. Rev. Microbiol.* **7**, 642–653
33. Caccamo, P. D., and Brun, Y. V. (2018) The Molecular Basis of Noncanonical Bacterial Morphology. *Trends Microbiol.* **26**, 191–208
34. Ghosal, D., Chang, Y., Jeong, K. C., Vogel, J. P., and Jensen, G. J. (2017) *In situ* structure of the *Legionella* Dot/Icm type IV secretion system by electron cryotomography. *EMBO Rep.* **18**, 726–732
35. Green, E. R., and Mecsas, J. (2016) Bacterial Secretion Systems: An Overview. *Microbiol. Spectr.* **4**, 1–19
36. Hospenthal, M. K., Costa, T. R. D., and Waksman, G. (2017) A comprehensive guide to pilus biogenesis in Gram-negative bacteria. *Nat. Rev. Microbiol.* **15**, 365–379
37. Kearns, D. B. (2010) A field guide to bacterial swarming motility. *Nat. Rev. Microbiol.* **8**, 634–644
38. Kim, J. H., Lee, J., Park, J., and Ghoo, Y. S. (2015) Gram-negative and Gram-positive bacterial extracellular vesicles. *Semin. Cell Dev. Biol.* **40**, 97–104
39. Press Release. (2017) The Nobel Prize in Chemistry 2017. NobelPrize.org. Nobel Media AB 2020. Available at: <https://www.nobelprize.org/prizes/chemistry/2017/press-release/> (26 Jan 2020)
40. Doerr, A. (2017) Cryo-electron tomography. *Nat. Methods.* **14**, 34
41. Stuart, D. I., Subramaniam, S., and Abrescia, N. G. A. (2016) The democratization of cryo-EM. *Nat. Methods.* **13**, 607–608
42. Alewijnse, B., Ashton, A. W., Chambers, M. G., Chen, S., Cheng, A., Ebrahim, M., Eng, E. T., Hagen, W. J. H., Koster, A. J., López, C. S., Lukyanova, N., Ortega, J., Renault, L., Reyntjens, S., Rice, W. J., Scapin, G., Schrijver, R., Siebert, A., Stagg, S. M., Grum-Tokars, V., Wright, E. R., Wu, S., Yu, Z., Zhou, Z. H., Carragher, B., and Potter, C. S. (2017) Best practices for managing large CryoEM facilities. *J. Struct. Biol.* **199**, 225–236
43. Dandey, V. P., Wei, H., Zhang, Z., Tan, Y. Z., Acharya, P., Eng, E. T., Rice, W. J., Kahn, P. A., Potter, C. S., and Carragher, B. (2018) Spotiton: New features and applications. *J. Struct. Biol.* **202**, 161–169
44. Rubinstein, J. L., Guo, H., Ripstein, Z. A., Haydaroglu, A., Au, A., Yip, C. M., Trani, J. M. Di, Benlekbi, S., and Kwok, T. (2019) Shake-it-off: A simple ultrasonic cryo-EM specimen preparation device. *bioRxiv.* 10.1101/632125
45. Comolli, L. R., Duarte, R., Baum, D., Luef, B., Downing, K. H., Larson, D. M., Csencsits, R., and Banfield, J. F. (2012) A portable cryo-plunger for on-site intact cryogenic microscopy sample preparation in natural environments. *Microsc. Res. Tech.* **75**, 829–836
46. Chen, S., Beeby, M., Murphy, G. E., Leadbetter, J. R., Hendrixson, D. R., Briegel, A., Li, Z., Shi, J., Tocheva, E. I., Müller, A., Dobro, M. J., and Jensen, G. J. (2011) Structural diversity of bacterial flagellar motors. *EMBO J.* **30**, 2972–2981
47. Briegel, A., Ladinsky, M. S., Oikonomou, C., Jones, C. W., Harris, M. J., Fowler, D. J., Chang, Y. W., Thompson, L. K., Armitage, J. P., and Jensen, G. J. (2014) Structure of bacterial cytoplasmic chemoreceptor arrays and implications for chemotactic signaling. *Elife.* **2014**, 1–16
48. Wang, J., Brackmann, M., Castaño-Díez, D., Kudryashev, M., Goldie, K. N., Maier, T., Stahlberg, H., and Basler, M. (2017) Cryo-EM structure of the extended type VI secretion system sheath-tube complex. *Nat. Microbiol.* 10.1038/s41564-017-

- 0020-7
49. Hand, E. (2020) 'We need a people's cryo-EM.' Scientists hope to bring revolutionary microscope to the masses. *Science* (80-.). 10.1126/science.aba9954
 50. Ali, M., Nelson, A. R., Lopez, A. L., and Sack, D. A. (2015) Updated global burden of cholera in endemic countries. *PLoS Negl. Trop. Dis.* 10.1371/journal.pntd.0003832
 51. Halpern, M., and Izhaki, I. (2017) Fish as hosts of *Vibrio cholerae*. *Front. Microbiol.* 10.3389/fmicb.2017.00282
 52. Laviad -Shitrit, S., Lev-Ari, T., Katzir, G., Sharaby, Y., Izhaki, I., and Halpern, M. (2017) Great cormorants (*Phalacrocorax carbo*) as potential vectors for the dispersal of *Vibrio cholerae*. *Sci. Rep.* 7, 7973
 53. Butler, S. M., and Camilli, A. (2005) Going against the grain: chemotaxis and infection in *Vibrio cholerae*. *Nat. Rev. Microbiol.* 3, 611–620
 54. Krebs, S. J., and Taylor, R. K. (2011) Protection and attachment of *Vibrio cholerae* mediated by the toxin-coregulated pilus in the infant mouse model. *J. Bacteriol.* 193, 5260–5270
 55. Utada, A. S., Bennett, R. R., Fong, J. C. N., Gibiansky, M. L., Yildiz, F. H., Golestanian, R., and Wong, G. C. L. (2014) *Vibrio cholerae* use pili and flagella synergistically to effect motility switching and conditional surface attachment. *Nat. Commun.* 5, 1–8
 56. Tacket, C. O., Taylor, R. K., Losonsky, G., Lim, Y. U., Nataro, J. P., Kaper, J. B., and Levine, M. M. (1998) Investigation of the roles of toxin-coregulated pili and mannose- sensitive hemagglutinin pili in the pathogenesis of *Vibrio cholerae* O139 infection. *Infect. Immun.* 66, 692–695
 57. Conner, J. G., Teschler, J. K., Jones, C. J., and Yildiz, F. H. (2016) Staying Alive: *Vibrio cholerae*'s Cycle of Environmental Survival, Transmission, and Dissemination. *Microbiol. Spectr.* 4, VMBF-0015-2015
 58. Peterson, K. M., and Gellings, P. S. (2018) Multiple intrainestinal signals coordinate the regulation of *Vibrio cholerae* virulence determinants. *Pathog. Dis.* 10.1093/femspd/ftx126
 59. Nelson, E. J., Chowdhury, A., Flynn, J., Schild, S., Bourassa, L., Shao, Y., Larocque, R. C., Calderwood, S. B., Qadri, F., and Camilli, A. (2008) Transmission of *Vibrio cholerae* is antagonized by lytic phage and entry into the aquatic environment. *PLoS Pathog.* 4, e1000187
 60. Almagro-Moreno, S., Pruss, K., and Taylor, R. K. (2015) Intestinal Colonization Dynamics of *Vibrio cholerae*. *PLoS Pathog.* 11, 1–11
 61. Merrell, D. S., Butler, S. M., Qadri, F., Dolganov, N. A., Alam, A., Cohen, M. B., Calderwood, S. B., Schoolnik, G. K., and Camilli, A. (2002) Host-induced epidemic spread of the cholera bacterium. *Nature.* 417, 642–645
 62. Bachmann, V., Kostiuik, B., Unterweger, D., Diaz-Satizabal, L., Ogg, S., and Pukatzki, S. (2015) Bile salts modulate the mucin-activated type vi secretion system of pandemic *vibrio cholerae*. *PLoS Negl. Trop. Dis.* 9, 1–22
 63. Bartlett, T. M., Bratton, B. P., Duvshani, A., Miguel, A., Sheng, Y., Martin, N. R., Nguyen, J. P., Persat, A., Desmarais, S. M., VanNieuwenhze, M. S., Huang, K. C., Zhu, J., Shaevitz, J. W., and Gitai, Z. (2017) A Periplasmic Polymer Curves *Vibrio cholerae* and Promotes Pathogenesis. *Cell.* 168, 172–185
 64. Brenzinger, S., Van Der Aart, L. T., Van Wezel, G. P., Lacroix, J. M., Glatter, T., and Briegel, A. (2019) Structural and proteomic changes in viable but non-culturable

REFERENCES

- vibrio cholerae. *Front. Microbiol.* **10**, 1–15
65. Shi, H., Westfall, C. S., Kao, J., Odermatt, P. D., Anderson, S. E., Cesar, S., Sievert, M., Moore, J., Gonzalez, C. G., Zhang, L., Elias, J. E., Chang, F., Huang, K. C., and Levin, P. A. (2021) Starvation induces shrinkage of the bacterial cytoplasm. *Proc. Natl. Acad. Sci. U. S. A.* 10.1073/pnas.2104686118
66. Runft, D. L., Mitchell, K. C., Abuaita, B. H., Allen, J. P., Bajer, S., Ginsburg, K., Neely, M. N., and Withey, J. H. (2014) Zebrafish as a natural host model for *Vibrio cholerae* colonization and transmission. *Appl. Environ. Microbiol.* **80**, 1710–1717
67. Murdoch, C. C., and Rawls, J. F. (2019) Commensal Microbiota Regulate Vertebrate Innate Immunity-Insights From the Zebrafish. *Front. Immunol.* **10**, 1–14
68. Millet, Y. A., Alvarez, D., Ringgaard, S., von Andrian, U. H., Davis, B. M., and Waldor, M. K. (2014) Insights into *Vibrio cholerae* Intestinal Colonization from Monitoring Fluorescently Labeled Bacteria. *PLoS Pathog.* 10.1371/journal.ppat.1004405
69. Pham, L. N., Kanther, M., Semova, I., and Rawls, J. F. (2008) Methods for generating and colonizing gnotobiotic zebrafish. *Nat. Protoc.* **3**, 1862–1875
70. Depelteau, J. S., Koning, G., Yang, W., and Briegel, A. (2020) An Economical, Portable Manual Cryogenic Plunge Freezer for the Preparation of Vitrified Biological Samples for Cryogenic Electron Microscopy. *Microsc. Microanal.* **26**, 413–418
71. Zheng, S. Q., Keszthelyi, B., Branlund, E., Lyle, J. M., Braunfeld, M. B., Sedat, J. W., and Agard, D. A. (2007) UCSF tomography: An integrated software suite for real-time electron microscopic tomographic data collection, alignment, and reconstruction. *J. Struct. Biol.* **157**, 138–147
72. Mastronarde, D. N. (2005) Automated electron microscope tomography using robust prediction of specimen movements. *J. Struct. Biol.* **152**, 36–51
73. Kremer, J. R., Mastronarde, D. N., and McIntosh, J. R. (1996) Computer visualization of three-dimensional image data using IMOD. *J. Struct. Biol.* **116**, 71–76
74. Mastronarde, D. N., and Held, S. R. (2017) Automated tilt series alignment and tomographic reconstruction in IMOD. *J. Struct. Biol.* **197**, 102–113
75. Oikonomou, C. M., and Jensen, G. J. (2016) A new view into prokaryotic cell biology from electron cryotomography. *Nat. Rev. Microbiol.* **14**, 205–220
76. Briegel, A., Ortega, D. R., Tocheva, E. I., Wuichet, K., Li, Z., Chen, S., Muller, A., Iancu, C. V., Murphy, G. E., Dobro, M. J., Zhulin, I. B., and Jensen, G. J. (2009) Universal architecture of bacterial chemoreceptor arrays. *Proc Natl Acad Sci U S A.* **106**, 17181–17186
77. Rapisarda, C., Cherrak, Y., Kooger, R., Schmidt, V., Pellarin, R., Logger, L., Cascales, E., Pilhofer, M., Durand, E., and Fronzes, R. (2019) *In situ* and high-resolution cryo-EM structure of a bacterial type VI secretion system membrane complex. *EMBO J.* 10.15252/embj.2018100886
78. Dobro, M. J., Oikonomou, C. M., Piper, A., Cohen, J., Guo, K., Jensen, T., Tadayon, J., Donermeyer, J., Park, Y., Solis, B. A., Kjær, A., Jewett, A. I., McDowall, A. W., Chen, S., Chang, Y. W., Shi, J., Subramanian, P., Iancu, C. V., Li, Z., Briegel, A., Tocheva, E. I., Pilhofer, M., and Jensen, G. J. (2017) Uncharacterized bacterial structures revealed by electron cryotomography. *J. Bacteriol.* **199**, 1–14
79. Ferreira, J. L., Gao, F. Z., Rossmann, F. M., Nans, A., Brenzinger, S., Hosseini, R.,

- Wilson, A., Briegel, A., Thormann, M., Rosenthal, P. B., and Beeby, M. (2019) γ - proteobacteria eject their polar flagella under nutrient depletion , retaining flagellar motor relic structures. *PLoS Biol.* **17**, e3000165
80. Alam, A., LaRocque, R. C., Harris, J. B., Vanderspurt, C., Ryan, E. T., Qadri, F., and Calderwood, S. B. (2005) Hyperinfectivity of human-passaged *Vibrio cholerae* can be modeled by growth in the infant mouse. *Infect. Immun.* **73**, 6674–6679
 81. Tamayo, R., Patimalla, B., and Camilli, A. (2010) Growth in a biofilm induces a hyperinfectious phenotype in *Vibrio cholerae*. *Infect. Immun.* **78**, 3560–3569
 82. Bourassa, L., and Camilli, A. (2009) Glycogen contributes to the environmental persistence and transmission of *Vibrio cholerae*. *Mol. Microbiol.* **72**, 124–138
 83. von Kruger, W. M. A., Lery, L. M. S., Soares, M. R., de Neves-Manta, F. S., Batista e Silva, C. M., Neves-Ferreira, A. G. da C., Perales, J., and Bisch, P. M. (2006) The phosphate-starvation response in *Vibrio cholerae* O1 and *phoB* mutant under proteomic analysis : Disclosing functions involved in adaptation , survival and virulence. *Protein Sci.* **6**, 1495–1511
 84. Harapin, J., Börmel, M., Sapra, K. T., Brunner, D., Kaeck, A., and Medalia, O. (2015) Structural analysis of multicellular organisms with cryo-electron tomography. *Nat. Methods.* **12**, 634–636
 85. Medeiros, J. M., Böck, D., and Pilhofer, M. (2018) Imaging bacteria inside their host by cryo-focused ion beam milling and electron cryotomography. *Curr. Opin. Microbiol.* **43**, 62–68
 86. Juraszek, J., Rutten, L., Blokland, S., Bouchier, P., Voorzaat, R., Ritschel, T., Bakkers, M. J. G., Renault, L. L. R., and Langedijk, J. P. M. (2021) Stabilizing the closed SARS-CoV-2 spike trimer. *Nat. Commun.* **12**, 1–8
 87. Ma, J., Su, D., Sun, Y., Huang, X., Liang, Y., Fang, L., Ma, Y., Li, W., Liang, P., and Zheng, S. (2021) Cryo-EM structure of S-Trimer, a subunit vaccine candidate for COVID-19. *J. Virol.* 10.1128/jvi.00194-21
 88. Wolff, G., Limpens, R. W. A. L., Zevenhoven-Dobbe, J. C., Laugks, U., Zheng, S., de Jong, A. W. M., Koning, R. I., Agard, D. A., Grünewald, K., Koster, A. J., Snijder, E. J., and Bárcena, M. (2020) A molecular pore spans the double membrane of the coronavirus replication organelle. *Science (80-.).* **369**, 1395–1398
 89. Yao, H., Song, Y., Chen, Y., Wu, N., Xu, J., Sun, C., Zhang, J., Weng, T., Zhang, Z., Wu, Z., Cheng, L., Shi, D., Lu, X., Lei, J., Crispin, M., Shi, Y., Li, L., and Li, S. (2020) Molecular Architecture of the SARS-CoV-2 Virus. *Cell.* **183**, 730-738.e13
 90. Subramaniam, S. (2020) COVID-19 and cryo-EM. *IUCrJ.* **7**, 575–576
 91. Jin, Q., Vogt, S., Lai, B., Chen, S., Finney, L., Gleber, S. C., Ward, J., Deng, J., Mak, R., Moonier, N., and Jacobsen, C. (2015) Ultraviolet germicidal irradiation and its effects on elemental distributions in mouse embryonic fibroblast cells in x-ray fluorescence microanalysis. *PLoS One.* **10**, 1–14
 92. Welch, D., Buonanno, M., Grilj, V., Shuryak, I., Crickmore, C., Bigelow, A. W., Randers-Pehrson, G., Johnson, G. W., and Brenner, D. J. (2018) Far-UVC light: A new tool to control the spread of airborne-mediated microbial diseases. *Sci. Rep.* **8**, 1–7
 93. Boyce, J. M., and Donskey, C. J. (2019) Understanding ultraviolet light surface decontamination in hospital rooms: A primer. *Infect. Control Hosp. Epidemiol.* **40**, 1030–1035
 94. Britt, A. B. (1996) DNA damage and repair in plants. *Annu. Rev. Plant Physiol. Plant Mol. Biol.* **47**, 75–100

REFERENCES

95. Durchschlag, H., Fochler, C., Feser, B., Hausmann, S., Seroneit, T., Swientek, M., Swoboda, E., Winklmaier, A., Wlček, C., and Zipper, P. (1996) Effects of X- and UV-irradiation on proteins. *Radiat. Phys. Chem.* **47**, 501–505
96. Krisko, A., and Radman, M. (2010) Protein damage and death by radiation in *Escherichia coli* and *Deinococcus radiodurans*. *Proc. Natl. Acad. Sci. U. S. A.* **107**, 14373–14377
97. Silva-Valenzuela, C. A., and Camilli, A. (2019) Niche adaptation limits bacteriophage predation of *Vibrio cholerae* in a nutrient-poor aquatic environment. *Proc. Natl. Acad. Sci.* **116**, 1627–1632
98. Hagen, W. J. H., Wan, W., and Briggs, J. A. G. (2017) Implementation of a cryo-electron tomography tilt-scheme optimized for high resolution subtomogram averaging. *J. Struct. Biol.* **197**, 191–198
99. Diebolder, C. A., Dillard, R. S., and Renault, L. L. R. (2021) From tube to structure: SPA cryo-EM workflow using apoferritin as an example. *Methods Mol. Biol.* **2305**, 229–256
100. Xiong, Q., Morpew, M. K., Schwartz, C. L., Hoenger, A. H., and Mastronarde, D. N. (2009) CTF determination and correction for low dose tomographic tilt series. *J. Struct. Biol.* **168**, 378–387
101. Castaño-Díez, D., Kudryashev, M., and Stahlberg, H. (2017) Dynamo Catalogue: Geometrical tools and data management for particle picking in subtomogram averaging of cryo-electron tomograms. *J. Struct. Biol.* **197**, 135–144
102. Castaño-Díez, D., Kudryashev, M., Arheit, M., and Stahlberg, H. (2012) Dynamo: A flexible, user-friendly development tool for subtomogram averaging of cryo-EM data in high-performance computing environments. *J. Struct. Biol.* **178**, 139–151
103. Kucukelbir, A., Sigworth, F. J., and Tagare, H. D. (2014) Quantifying the local resolution of cryo-EM density maps. *Nat. Methods.* **11**, 63–65
104. Scheres, S. H. W. (2012) A bayesian view on cryo-EM structure determination. *J. Mol. Biol.* **415**, 406–418
105. Zhang, K. (2016) Gctf: Real-time CTF determination and correction. *J. Struct. Biol.* **193**, 1–12
106. Zheng, S. Q., Palovcak, E., Armache, J. P., Verba, K. A., Cheng, Y., and Agard, D. A. (2017) MotionCor2: Anisotropic correction of beam-induced motion for improved cryo-electron microscopy. *Nat. Methods.* **14**, 331–332
107. Chen, Z., Sun, L., Zhang, Z., Fokine, A., Padilla-Sanchez, V., Hanein, D., Jiang, W., Rossmann, M. G., and Rao, V. B. (2017) Cryo-EM structure of the bacteriophage T4 isometric head at 3.3-Å resolution and its relevance to the assembly of icosahedral viruses. *Proc. Natl. Acad. Sci. U. S. A.* **114**, E8184–E8193
108. Zivanov, J., Nakane, T., Forsberg, B. O., Kimanius, D., Hagen, W. J. H., Lindahl, E., and Scheres, S. H. W. (2018) New tools for automated high-resolution cryo-EM structure determination in RELION-3. *Elife.* **7**, 1–22
109. Rohou, A., and Grigorieff, N. (2015) CTFFIND4: Fast and accurate defocus estimation from electron micrographs. *J. Struct. Biol.* **192**, 216–221
110. Zivanov, J., Nakane, T., and Scheres, S. H. W. (2019) A Bayesian approach to beam-induced motion correction in cryo-EM single-particle analysis. *IUCrJ.* **6**, 5–17
111. Zivanov, J., Nakane, T., and Scheres, S. H. W. (2020) Estimation of high-order aberrations and anisotropic magnification from cryo-EM data sets in RELION-3.1. *IUCrJ.* **7**, 253–267
112. Goddard, T. D., Huang, C. C., Meng, E. C., Pettersen, E. F., Couch, G. S., Morris, J.

- H., and Ferrin, T. E. (2018) UCSF ChimeraX: Meeting modern challenges in visualization and analysis. *Protein Sci.* **27**, 14–25
113. Barth, Z. K., Netter, Z., Angermeyer, A., Bhardwaj, P., and Seed, K. D. (2020) A Family of Viral Satellites Manipulates Invading Virus Gene Expression and Can Affect Cholera Toxin Mobilization. *mSystems*. **5**, 1–18
 114. Jumper, J., Evans, R., Pritzel, A., Green, T., Figurnov, M., Ronneberger, O., Tunyasuvunakool, K., Bates, R., Žídek, A., Potapenko, A., Bridgland, A., Meyer, C., Kohl, S. A. A., Ballard, A. J., Cowie, A., Romera-Paredes, B., Nikolov, S., Jain, R., Adler, J., Back, T., Petersen, S., Reiman, D., Clancy, E., Zielinski, M., Steinegger, M., Pacholska, M., Berghammer, T., Bodenstein, S., Silver, D., Vinyals, O., Senior, A. W., Kavukcuoglu, K., Kohli, P., and Hassabis, D. (2021) Highly accurate protein structure prediction with AlphaFold. *Nature*. 10.1038/s41586-021-03819-2
 115. Pettersen, E. F., Goddard, T. D., Huang, C. C., Couch, G. S., Greenblatt, D. M., Meng, E. C., and Ferrin, T. E. (2004) UCSF Chimera - A visualization system for exploratory research and analysis. *J. Comput. Chem.* **25**, 1605–1612
 116. Singharoy, A., Teo, I., McGreevy, R., Stone, J. E., Zhao, J., and Schulten, K. (2016) Molecular dynamics-based refinement and validation for sub-5 Å cryo-electron microscopy maps. *Elife*. **5**, 1–33
 117. Phillips, J. C., Braun, R., Wang, W., Gumbart, J., Tajkhorshid, E., Villa, E., Chipot, C., Skeel, R. D., Kalé, L., and Schulten, K. (2005) Scalable molecular dynamics with NAMD. *J. Comput. Chem.* **26**, 1781–1802
 118. Humphrey, W., Dalke, A., and Schulten, K. (1996) VMD: Visual Molecular Dynamics. *J. Mol. Graph.* **14**, 33–38
 119. Caspar, D. L., and Klug, A. (1962) Physical Principles in the Construction of Regular Viruses. *Cold Spring Harb Symp Quant Biol.* **27**, 1–24
 120. Ferraro, G., Ciambellotti, S., Messori, L., and Merlino, A. (2017) Cisplatin Binding Sites in Human H-Chain Ferritin. *Inorg. Chem.* **56**, 9064–9070
 121. Buonanno, M., Welch, D., Shuryak, I., and Brenner, D. J. (2020) Far-UVC light (222 nm) efficiently and safely inactivates airborne human coronaviruses. *Sci. Rep.* **10**, 1–8
 122. IES Photobiology Committee (2020) *IES Committee Report : Germicidal Ultraviolet (GUV) – Frequently Asked Questions*
 123. Berger, C., Ravelli, R. B. G., López-Iglesias, C., Kudryashev, M., Diepold, A., and Peters, P. J. (2021) Structure of the Yersinia injectisome in intracellular host cell phagosomes revealed by cryo FIB electron tomography. *J. Struct. Biol.* 10.1016/j.jsb.2021.107701
 124. Yang, W., Keith Cassidy, C., Ames, P., Diebolder, C. A., Schulten, K., Luthey-Schulten, Z., Parkinson, J. S., and Briegel, A. (2019) In situ conformational changes of the escherichia coli serine chemoreceptor in different signaling states. *MBio*. 10.1128/mBio.00973-19
 125. Muok, A. R., Ortega, D. R., Kurniyati, K., Yang, W., Maschmann, Z. A., Sidi Mabrouk, A., Li, C., Crane, B. R., and Briegel, A. (2020) Atypical chemoreceptor arrays accommodate high membrane curvature. *Nat. Commun.* **11**, 1–13
 126. Arnold, J., Mahamid, J., Lucic, V., De Marco, A., Fernandez, J. J., Laugks, T., Mayer, T., Hyman, A. A., Baumeister, W., and Plitzko, J. M. (2016) Site-Specific Cryo-focused Ion Beam Sample Preparation Guided by 3D Correlative Microscopy. *Biophys. J.* **110**, 860–869
 127. Bokhari, H., Ali, A., Noreen, Z., Thomson, N., and Wren, B. W. (2017) Galleria

REFERENCES

- mellonella is low cost and suitable surrogate host for studying virulence of human pathogenic *Vibrio cholerae*. *Gene*. **628**, 1–7
128. Schaffer, M., Mahamid, J., Engel, B. D., Laugks, T., Baumeister, W., and Plitzko, J. M. (2017) Optimized cryo-focused ion beam sample preparation aimed at in situ structural studies of membrane proteins. *J. Struct. Biol.* **197**, 73–82
129. Sartori, N., Richter, K., and Dubochet, J. (1993) Vitrification depth can be increased more than 10-fold by high-pressure freezing. *J. Microsc.* **172**, 55–61
130. Henderson, R. (1995) The Potential and Limitations of Neutrons, Electrons and X-Rays for Atomic Resolution Microscopy of Unstained Biological Molecules. *Q. Rev. Biophys.* **28**, 171–193
131. Eltsov, M., Grewe, D., Lemercier, N., Frangakis, A., Livolant, F., and Leforestier, A. (2018) Nucleosome conformational variability in solution and in interphase nuclei evidenced by cryo-electron microscopy of vitreous sections. *Nucleic Acids Res.* **46**, 9189–9200
132. Bharat, T. A. M., Hoffmann, P. C., and Kukulski, W. (2018) Correlative Microscopy of Vitreous Sections Provides Insights into BAR-Domain Organization In Situ. *Structure*. **26**, 879-886.e3
133. Couture-Tosi, E., Ranck, J.-L., Haustant, G., Pehau-Arnaudet, G., and Sachse, M. (2010) CEMOVIS on a pathogen: analysis of *Bacillus anthracis* spores. *Biol. Cell.* **102**, 609–619
134. Mielanczyk, L., Matysiak, N., Michalski, M., Buldak, R., and Wojnicz, R. (2014) Closer to the native state. Critical evaluation of cryo-techniques for Transmission Electron Microscopy: Preparation of biological samples. *Folia Histochem. Cytobiol.* **52**, 1–17
135. Melia, C. E., Bolla, J. R., Katharios-Lanwermyer, S., Mihaylov, D. B., Hoffmann, P. C., Huo, J., Wozny, M. R., Elfari, L. M., Böhning, J., Owens, R. J., Robinson, C. V., O'Toole, G. A., and Bharat, T. A. M. (2021) Architecture of cell-cell junctions in situ reveals a mechanism for bacterial biofilm inhibition. *Proc. Natl. Acad. Sci.* **118**, 2021.02.08.430230
136. Hohenberg, H., Tobler, M., and Müller, M. (1996) High-pressure freezing of tissue obtained by fine-needle biopsy. *J. Microsc.* **183**, 133–139
137. Hohenberg, H., Mannweiler, K., and Muller, M. (1994) High-pressure freezing of cell suspensions in cellulose capillary tubes. *J. Microsc.* **175**, 34–43
138. Nyholm, S. V., and McFall-Ngai, M. J. (2021) A lasting symbiosis: how the Hawaiian bobtail squid finds and keeps its bioluminescent bacterial partner. *Nat. Rev. Microbiol.* 10.1038/s41579-021-00567-y
139. Sarkar, P., Bosneaga, E., Yap, E. G., Das, J., Tsai, W. T., Cabal, A., Neuhaus, E., Maji, D., Kumar, S., Joo, M., Yakovlev, S., Csencsits, R., Yu, Z., Bajaj, C., Downing, K. H., and Auer, M. (2014) Electron tomography of cryo-immobilized plant tissue: A novel approach to studying 3d macromolecular architecture of mature plant cell walls in situ. *PLoS One*. **9**, e106928
140. Meijer, A. H., and Spaink, H. P. (2011) Host-pathogen interactions made transparent with the zebrafish model. *Curr. Drug Targets.* **12**, 1000–17
141. Gitai, Z. (2005) The new bacterial cell biology: Moving parts and subcellular architecture. *Cell*. **120**, 577–586
142. Klose, K. E. (2000) The suckling mouse model of cholera. *Trends Microbiol.* **8**, 189–191
143. Lutz, C., Erken, M., Noorian, P., Sun, S., and McDougald, D. (2013) Environmental

- reservoirs and mechanisms of persistence of *Vibrio cholerae*. *Front. Microbiol.* **4**, 1–15
144. Singh, A., and Barnard, T. G. (2016) Surviving the acid barrier: responses of pathogenic *Vibrio cholerae* to simulated gastric fluid. *Appl. Microbiol. Biotechnol.* **100**, 815–824
 145. Yang, J. H., Wu, U. I., Tai, H. M., and Sheng, W. H. (2019) Effectiveness of an ultraviolet-C disinfection system for reduction of healthcare-associated pathogens. *J. Microbiol. Immunol. Infect.* **52**, 487–493
 146. Weiss, G. L., Kieninger, A.-K., Maldener, I., Forchhammer, K., and Pilhofer, M. (2019) Structure and function of a bacterial gap junction analog. *Cell.* **178**, 374–384
 147. Rigort, A., and Plitzko, J. M. (2015) Cryo-focused-ion-beam applications in structural biology. *Arch. Biochem. Biophys.* **581**, 122–130
 148. Romero-Brey, I. (2018) 3D Electron Microscopy (EM) and Correlative Light Electron Microscopy (CLEM) Methods to Study Virus-Host Interactions. in *Influenza Virus: Methods and Protocols* (Yamauchi, Y. ed), pp. 213–236, Springer Nature, **1836**, 213–236
 149. Cyrklaff, M., Frischknecht, F., and Kudryashev, M. (2017) Functional insights into pathogen biology from 3D electron microscopy. *FEMS Microbiol. Rev.* **41**, 1–26
 150. Cho, I., and Blaser, M. J. (2012) The human microbiome: At the interface of health and disease. *Nat. Rev. Genet.* **13**, 260–270
 151. Cho, J. Y., Liu, R., Macbeth, J. C., and Hsiao, A. (2021) The Interface of *Vibrio cholerae* and the Gut Microbiome. *Gut Microbes.* 10.1080/19490976.2021.1937015
 152. Ligthart, K., Belzer, C., de Vos, W. M., Tytgat, H. L. P. P., Vos, W. M. De, and Tytgat, H. L. P. P. (2020) Bridging Bacteria and the Gut: Functional Aspects of Type IV Pili. *Trends Microbiol.* **28**, 340–348
 153. Sokol, N. S., and Newton, I. L. G. (2020) The Microbiome Sets the Stage for Cholera. *Trends Microbiol.* **28**, 430–432
 154. Rubinsky, B., Perez, P. A., and Carlson, M. E. (2005) The thermodynamic principles of isochoric cryopreservation. *Cryobiology.* **50**, 121–138
 155. Fuest, M., Schaffer, M., Nocera, G. M., Galilea-Kleinsteuber, R. I., Messling, J. E., Heymann, M., Plitzko, J. M., and Burg, T. P. (2019) In situ Microfluidic Cryofixation for Cryo Focused Ion Beam Milling and Cryo Electron Tomography. *Sci. Rep.* **9**, 1–10
 156. Sergey, G., Denis, K., Ava, H., Gediminas, G., Viola, O., Owen L., K., Ruby H.P., L., Moira O', B., Roger, P., James C., W., and Alex, de M. (2018) Oxygen plasma focused ion beam scanning electron microscopy for biological samples. *bioRxiv.* 10.1101/457820
 157. Gorelick, S., Buckley, G., Gervinskas, G., Johnson, T. K., Handley, A., Caggiano, M. P., Whisstock, J. C., Pocock, R., and de Marco, A. (2019) PIE-scope, integrated cryo-correlative light and FIB/SEM microscopy. *Elife.* **8**, 1–15
 158. Wilfling, F., Lee, C. W., Erdmann, P. S., Zheng, Y., Sherpa, D., Jentsch, S., Pfander, B., Schulman, B. A., and Baumeister, W. (2020) A Selective Autophagy Pathway for Phase-Separated Endocytic Protein Deposits. *Mol. Cell.* **80**, 764–778.e7

NEDERLANDSE SAMENVATTING

Bacteriën zijn onmisbaar in de natuur. Toch is er nog veel onbekend over hoe ze zich kunnen aanpassen aan veranderende omstandigheden en kunnen gedijen als individuele cellen, als onderdeel van microbiële gemeenschappen of in nauw contact met een gastheer. Dit geldt met name voor hoe de structurele samenstelling van bacteriële cellen bijdraagt aan hun vermogen om te navigeren en te overleven in verschillende niches. Het verkrijgen van inzicht in bacteriële ultrastructuur onder verschillende omstandigheden is essentieel om te begrijpen hoe bacteriën zich aanpassen en veranderen in complexe milieus. Gedetailleerd inzicht in hun specifieke morfologische en structurele kenmerken kan nieuwe inzichten geven in de behandelwijze van lastige infecties.

Om beter te begrijpen hoe cellen werken en hoe hun interactie met de omgeving is op micro- en nanoschaalniveau, moeten we inzoomen met krachtige microscopiemethoden zoals cryogene elektronenmicroscopie (cryo-EM). Voor vragen op cellulair niveau en waarbij monsters met een gemengde samenstelling onderzocht worden, is cryogene elektronentomografie (cryo-ET) het instrument bij uitstek, omdat het de visualisatie van monsters in bijna oorspronkelijke staat mogelijk maakt, in drie dimensies en met macromoleculaire resolutie. Voor structureel onderzoek naar geïsoleerde eiwitcomplexen in gefilterde homogene monsters, passen we een andere cryo-EM-methode toe, genaamd “enkeledeeltjes-analyse”, of “single particle analysis” (SPA). Met deze techniek kunnen we individuele eiwitten of eiwitstructuren visualiseren met een resolutie van nanometers. Om beter te begrijpen hoe microben worden beïnvloed door veranderingen in hun omgeving, heb ik hier cryo-EM toegepast, evenals lichtmicroscopie en microbiologische methoden.

In **hoofdstuk twee** begin ik met een overzicht van bacteriële en archaeale ultrastructuur, waarbij ik de nadruk leg op moleculaire machines die zijn onderzocht met verschillende methodes, waaronder cryo-EM. Eerst laat ik in grote lijnen zien hoe de verschillende structuren van de celenvelop fungeren als grenzen tussen de binnenste inhoud van de cel en de externe omgeving. Dit koppel ik vervolgens aan de celvorm en daarna behandel ik het proces van celdeling. Ten slotte bespreek ik structuren die een directe interactie hebben met de externe omgeving, zoals de verschillende aanhangsels van microben en hun secretiesystemen.

Daaropvolgend beschrijf ik de ontwikkeling van een handmatig draagbare invriesmachine, of “portable manual plunge freezing device” (PMPF, **hoofdstuk drie**). De hier ontwikkelde PMPF is een goedkoop alternatief voor in de handel verkrijgbare opties en zorgt ervoor dat het apparaat gemakkelijk van laboratorium

naar laboratorium kan worden verplaatst, lokaal, nationaal en internationaal. Met behulp van de PMPF, onderzoek ik de ziekteverwekker *Vibrio cholerae* op veranderingen in de morfologie en de bijbehorende moleculaire machines, terwijl deze bacterie overgaat van de omgeving naar een zebra-visgastheer en vervolgens weer terug naar de omgeving. Dit werk toont aan dat de reis door het spijsverteringskanaal van een natuurlijke gastheer leidt tot een bacterie die veerkrachtiger is en die zich beter kan aanpassen aan veranderingen in de omgeving. Deze veerkracht zorgt er waarschijnlijk ook voor dat de bacterie efficiënter van gastheer naar gastheer kan gaan. Analyse van de moleculaire machines toonde aan dat cellen die hun vibroïde of bijna-vibroïde vorm behielden, ook de moleculaire machines behielden die belangrijk zijn voor de hechting en het waarnemen van de omgeving.

Werken met een pathogene soort, zoals *V. cholerae*, vereist de naleving van strikte richtlijnen voor biologische veiligheid, zodat de veiligheid van personeel, onderzoekers en de omgeving kan worden gewaarborgd. In een poging toegang te verkrijgen tot cryo-EM-faciliteiten die niet gecertificeerd zijn om te werken met monsters met een hoger biologische veiligheidsniveau (ML II of hoger), heb ik me vervolgens gericht op het effect van ultraviolet C (UVC) bestraling op de integriteit van monsters en de mogelijkheid tot het verkrijgen van hoge resolutie en structurele informatie van deze bestraalde monsters (**hoofdstuk vijf**). In dit hoofdstuk heb ik me gericht op twee soorten monsters, namelijk de bacterie *V. cholerae* voor het middelen van subtomogram en de ICP1-bacteriofaag voor de analyse met SPA. Deze studie toonde aan dat UVC-blootstelling bij cryogene temperaturen een geschikte methode is om ziekteverwekkers te inactiveren. Bovendien is de structurele informatie die wordt verkregen uit geïnactiveerde pathogenen niet te onderscheiden van onbehandelde organismen. Naast het economische apparaat dat wordt gebruikt voor UVC-behandeling, demonstreert dit hoofdstuk ook de mogelijkheid om UVC-bestraling te gebruiken als een manier om het biologische veiligheidsniveau van pathogenen te verlagen, die vervolgens in de meeste cryo-EM-faciliteiten kunnen worden bekeken, zelfs zonder biologische veiligheidscertificaten.

Het onderzoeken van bacteriële cellen, virussen of eiwitcomplexen met cryo-EM vereist gespecialiseerde monstervoorbereidingstechnieken. Voor monsters met een dikte van minder dan 5-10 µm kunnen we “plunge freeze” gebruiken om het monster in te bedden in een glasachtige staat die de integriteit van het monster behoudt (**hoofdstukken drie, vier, vijf**). Monsters die dikker zijn, zoals grotere eukaryote cellen, weefsels of microbiële biofilms, vereisen bevriezing onder hoge druk om artefacten, veroorzaakt door ijskristalvorming, te voorkomen en de

daaropvolgende verdunning van het monster. In **hoofdstuk zes** beschrijf ik de huidige staat van monstervoorbereiding van grotere volumes voor cryo-EM en introduceer ik het gebruik van micro gefabriceerde biopsienaalden. Eerst heb ik glazen naalden getest voor de biopsie van verschillende weefseltypes. Vervolgens gebruik ik 3D-geprinte naalden om monsters te halen uit een bacteriekolonie van *Streptomyces coelicolor*, die daarna werden ingevroren onder hoge druk ter voorbereiding op de verdunning van het monster door cryo-ultramicrotomie en cryo-FIB SEM. Dit werk biedt de allereerste proof-of-concept-experimenten om door te gaan met de ontwikkeling van deze nieuwe biopsienaalden voor de cryo-EM-workflow.

Samenvattend draagt dit proefschrift bij aan belangrijke ontwikkelingen op het gebied van cryo-EM, door een bredere toegang te bieden tot technieken die traditioneel beperkt waren tot een paar goed uitgeruste laboratoria. Met de oprichting van regionale en nationale faciliteiten met microscopen die toegankelijk zijn voor de onderzoeksgemeenschap, worden nieuwe gebruikers uitgenodigd om lokaal monsters voor te bereiden voordat ze deze faciliteiten inschakelen. Daarnaast introduceer ik een nieuw hulpmiddel voor monstervoorbereiding voor gebruikers die werken met organismen die als BSL II of hoger worden beschouwd, waarmee deze organismen van een hoger veiligheidsniveau kunnen worden teruggebracht tot niveaus die acceptabel zijn voor dergelijke faciliteiten. Het combineren van de UVC-techniek met de PMPF vermindert de investering in het voorbereiden van deze monsters aanzienlijk, en zal een enorm inzicht geven in het *in vivo* organisme. Deze nieuwe hulpmiddelen, samen met andere opkomende technieken voor monstervoorbereiding van grote volumes en nieuwe modellen van interacties tussen de pathogeen en gastheer, bieden een geheel nieuwe set hulpmiddelen voor het verkennen van microben en hun interactie met de omgeving.

CURRICULUM VITAE

Jamie Scott Depelteau was born on 27 May 1979 in Concord, New Hampshire in the United States of America. In 2001, he obtained a Bachelor of Science degree in Microbiology and Cell Sciences at the University of Florida (USA). During this time, his undergraduate research focused on understanding the genetic and environmental influences on the development of infantile hydrocephalus in the HTx rat model. From 2001-2004, he pursued post-graduate studies and research in the biomedical sciences at The Ohio State University (OSU). Here, his research focused on the dendritically targeted mRNA, *Pcp-2/L7*, and its role in synaptic plasticity. Subsequently, he completed a Master of Arts degree in education at The OSU in 2006. From 2006 until 2016, he worked in education-related positions at various universities in the USA. His last position was the Manager of Undergraduate Affairs and Curriculum Planning at the University of California, Berkeley, where he oversaw the undergraduate advising and curriculum for the Departments of Molecular and Cell Biology, and Integrative Biology. Simultaneously, he performed research in the laboratory of prof. dr. Matthew Welch with the goal of employing the CRISPR/Cas9 system to study factors affecting the Arp2/3 actin nucleation in mammalian cell lines. After moving to the Netherlands, he began work as a PhD candidate under the supervision of prof. dr. Ariane Briegel and prof. dr. Annemarie Meijer. The results of this PhD research are presented in this dissertation.

PUBLICATIONS

Depelteau JS, Limpens R, Nag D, Koch BEV, Withey JH, Meijer AH, Briegel A. (2021) Transition of *Vibrio cholerae* through a natural host induces resistance to environmental changes. bioRxiv 2021.09.30.462513; doi: <https://doi.org/10.1101/2021.09.30.462513>

Depelteau JS, Renault L, Althof N, Cassidy CK, Mendonça LM, Jensen GJ, Resch GP, Briegel A. UVC inactivation of pathogenic samples suitable for cryo-EM analysis. (2021) bioRxiv 2021.07.06.451241; doi: <https://doi.org/10.1101/2021.07.06.451241>

Lemos Rocha LF.; Peters K; **Depelteau JS**; Briegel A; Vollmer W; Blokesch M. (2021) The VarA-CsrA regulatory pathway determines cell shape in *Vibrio cholerae*. bioRxiv 2021.09.09.459595; doi: <https://doi.org/10.1101/2021.09.09.459595>

Depelteau JS, Koning G, Yang W, Briegel A. (2020) An Economical, Portable Manual Cryogenic Plunge Freezer for the Preparation of Vitriified Biological Samples for Cryogenic Electron Microscopy. Microsc Microanal 26, 413–418. doi:10.1017/S1431927620001385

Depelteau JS, Brenzinger S, and Briegel A. (2019) Bacterial and Archaeal Cell Structure, Editor(s): Thomas M. Schmidt, Encyclopedia of Microbiology (Fourth Edition), Academic Press, Pages 348-360.

Ultee E, Schenkel F, Yang W, Brenzinger S, **Depelteau JS**, & Briegel A (2018). An Open-Source Storage Solution for Cryo-Electron Microscopy Samples. Microscopy and Microanalysis, 24(1), 60–63. <https://doi.org/10.1017/S143192761701279X>

Jones HC, **Depelteau JS**, Carter BJ, & Somera KC (2002). The frequency of inherited hydrocephalus is influenced by intrauterine factors in H-Tx rats. Exp Neurol, 176(1), 213–220. <https://doi.org/10.1006/exnr.2002.7921>

Depelteau JS, Jones HC. Lactation after gestation affects the expression of inherited hydrocephalus in H-Tx rats. Eur J Pediatr Surg. 2001 Dec;11 Suppl 1:S49-51. PMID: 11848053.

Jones HC, Carter BJ, **Depelteau JS**, Roman M, & Morel L. (2001). Chromosomal linkage associated with disease severity in the hydrocephalic H-Tx rat. Behavior Genetics, 31(1), 101–111. <https://doi.org/10.1023/A:1010266110762>

Jones HC, **Depelteau JS**, Carter BJ, Lopman BA, & Morel L. (2001). Genome-wide linkage analysis of inherited hydrocephalus in the H-Tx rat. Mammalian Genome, 12(1), 22–26. <https://doi.org/10.1007/s003350010226>

Jones HC, Lopman BA, Jones TW, Carter BJ, **Depelteau JS**, & Morel L. (2000). The expression of inherited hydrocephalus in H-Tx rats. Childs Nerv Syst, 16(9), 578–584. <https://doi.org/10.1007/s003810000330>